2015-07-01

The Synthesis and Characterization of Ferritin Bio Minerals for Photovoltaic, Nanobattery, and Bio-Nano Propellant Applications

Trevor Jamison Smith
Brigham Young University

BYU ScholarsArchive Citation

Smith, Trevor Jamison, "The Synthesis and Characterization of Ferritin Bio Minerals for Photovoltaic, Nanobattery, and Bio-Nano Propellant Applications" (2015). *All Theses and Dissertations*. 6045.
https://scholarsarchive.byu.edu/etd/6045

The Synthesis and Characterization of Ferritin Bio Minerals for Photovoltaic, Nanobattery, and Bio-Nano Propellant Applications

Trevor Jamison Smith

A dissertation submitted to the faculty of
Brigham Young University
in partial fulfillment of the requirements for the degree of

Doctor of Philosophy

Richard K. Watt, Chair
Matthew C. Asplund
John S. Colton
Roger G. Harrison
Brian F. Woodfield

Department of Chemistry and Biochemistry

Brigham Young University

July 2015

ABSTRACT

The Synthesis and Characterization of Ferritin Bio Minerals for Photovoltaic, Nanobattery, and Bio-Nano Propellant Applications

Trevor Jamison Smith
Department of Chemistry and Biochemistry, BYU
Doctor of Philosophy

Material science is an interdisciplinary area of research, which in part, designs and characterizes new materials. Research is concerned with synthesis, structure, properties, and performance of materials. Discoveries in materials science have significant impact on future technologies, especially in nano-scale applications where the physical properties of nanomaterials are significantly different than their bulk counterparts. The work presented here discusses the use of ferritin, a hollow sphere-like biomolecule, which forms metal oxo-hydride nanoparticles inside its protein shell for uses as a bio-inorganic material.

Ferritin is capable of forming and sequestering 8 nm metal-oxide nanoparticles within its 2 nm thick protein shell. A variety of metal-oxide nanoparticles have been synthesized inside ferritin. The work herein focuses on three distinct areas:

1) Ferritin's light harvesting properties: namely band gaps. Discrepancies in the band gap energies for ferritin's native ferrihydrite mineral and non-native minerals have been previously reported. Through the use of optical absorption spectroscopy, I resolved the types of band gaps as well as the energy of these band gaps. I show that metal oxides in ferritin are indirect band gap semiconductors which also contain a direct transition. Modifications to the ferrihydrite mineral's band gaps are measured as a result of co-depositing anions into ferritin during iron loading. I demonstrate that these band gaps can be used to photocatalytically reduce gold ions in solution with titanium oxide nanoparticles in ferritin.

2) A new method for manganese mineral synthesis inside ferritin: Comproportionation between permanganate and Mn(II) forms new manganese oxide minerals inside ferritin that are different than traditional manganese oxide mineral synthesis. This reaction creates a MnO_2, Mn_2O_3, or Mn_3O_4 mineral inside ferritin, depending on the synthesis conditions.

3) Ferritin as an energetic material: Ferritin is capable of sequestering various metals and anions into its interior. Perchlorate, an energetic anion, is sequestered through a co-deposition process during iron loading and is tested with energetic binding materials. Peroxide, which can be used as an oxidant, is also shown to be sequestered within apoferritin and combined with an aluminum based fuel for solid rocket propellants.

Keywords: ferritin, photovoltaic, photochemistry, photocatalyst, gold nanoparticles, ferrihydrite, band gap, optical absorption spectroscopy, metal-oxide, nanoparticle, bio-inorganic material, biomaterial

ACKNOWLEDGEMENTS

I would like to thank my advisor, Dr. Richard K. Watt, for his help and guidance in completing my degree. I would also like to thank Dr. John S. Colton for his help and collaboration in my research endeavors. Additionally, I would like to thank my committee members--Roger G. Harrison, Matthew C. Asplund, and Brian F. Woodfield--for their insight and expertise that helped to bring this work to fruition.

I also appreciate the support, love, and understanding that my wife, Jennifer Smith, has given me, and for my children, Ruby and Seth, for their love, support and patience.

I also want to thank the undergraduate students whom without, I would not have been able to produce the high quality publications in a short time frame which has allowed to me finishing my degree as quickly as I have. Namely: Stephen Erickson, Cameron Olsen, Jacob Embely, Jake Maxfield, and Kevin Zenner.

Table of Contents

Table of Tables

Table of Figures

Chapter 1

Chapter 2

Chapter 3

Chapter 4

Chapter 5

Chapter 6

Chapter 7

Chapter 8

Chapter 9

Chapter 1 – An Introduction to Ferritin and Its Role in Material Science

This chapter contains an introduction to and review of ferritin and its role in material science. In particular, the majority of my research has focused on synthesizing ferritin minerals as a charge separation photo catalyst; therefor this chapter focuses on that aspect of ferritin materials chemistry. I have also included a review of the field of photovoltaic systems to put my research on charge separation catalysts into perspective of how ferritin might become involved in artificial photosynthesis applications. I was a co-author of an in-depth review describing the use of ferritin as a charge separation photo catalyst. It is available at Catalysis Science & Technology, volume 3, issue 2, 2013, pp 3103-3110, and is titled "Ferritin as a model for developing 3rd generation nano architecture organic/inorganic hybrid photo catalysts for energy conversion".

Overview

The world consumes a significant amount of energy every year, which reached 132,000 Terawatt hours in 2008[1] and has increased by 2% every year[2] since then. The need for energy is further complicated by dwindling fossil fuel reserves, political unrest in countries that have large fossil fuel reserves, and increasing environmental pollution. Renewable energy sources offer a promising solution to meet the increasing global energy demand and be free of current issues with fossil fuels.

Solar energy is a promising solution to help meet global energy demand. Approximately 12.2 trillion watts of energy strikes the earth's crust per square mile per year.[3] Near perfect conversion of solar energy into electricity would require tens of thousands of square miles to meet global energy demand. However, the world's best solar panels are only 44% efficient[4], may contain toxic materials, have a low natural abundance of elements, and are difficult to mass produce. A cheaper, non-toxic and efficient solar panel or photovoltaic system is needed to address rising global energy consumption.

Research in photovoltaic systems (PVS) has mostly focused on obtaining higher photoelectric efficiencies and greater electric current output. However, these goals often overlook material expenses, chemical degradation, scarcity of materials, and other important factors. In a review article by R.K. Watt[5], the author addresses several of these issues in depth, and proposes four main problems with existing PVS: some PVS contain toxic materials, use expensive and rare metals, photo-corrode with use, and are limited by a theoretical limit known as the Shockley-Queisser limit[6].

The Shockley-Queisser limit describes a maximal 33.7% photon to electron conversion efficiency for a single material using the most abundant light energy of 1.34 eV or 925 nm from solar irradiance. Research conducted in an attempt to reach the maximal 33.7% efficiency has achieved 25% efficiency[7] using mono-crystalline silicon. Commercially available silicon solar panels are currently reaching 21.5% efficiency.[8] The 33.7% limit can be exceeded with a multi-layer PVS using concentrated sunlight and absorbing multiple wavelengths; with recent investigations achieving 44% efficiency[9] with a theoretical limit of 86% efficiency[10]. However, multilayer devices have proven difficult to manufacture, requiring mono-crystalline structure throughout all of the material layers used in the device.[11] Inefficiencies arise, either when photon energy exceeds the band gap in which excess energy will be lost as heat, or if the photon is of insufficient energy, in which case the photon is not absorbed. Attempts to overcome these inefficiencies, as well as the other issues concerning solar energy technology are being addressed over three generations of solar technology.

Generations of Solar Technology

Among the many different types of PVS available, three main classes or generations of PVS exist. First generation solar panels are made of various crystal types of silicon. Second generation PVS use thin film charge separation catalysts, such as amorphous silicon solar cells, dye sensitized solar cells (DSSC), perovskite solar cells, multi-junction solar cells, and CdTe solar cells. Future or third generation PVS use nanoparticles for their charge separation catalyst and include colloidal quantum dots, hybrid organic-inorganic systems, and may contain earth abundant materials which are benign and environmentally friendly.

First Generation Photovoltaic Systems

First generation PV systems are widely used to power both homes and businesses. These systems use earth abundant silicon, and are currently in large scale manufacturing. There are two types of first generation silicon PV systems: polycrystalline, and monocrystalline silicon solar cells. In both cases the initial installation costs are very high, and require almost twenty years of power generation to recoup the cost of investment.[12,13] The majority of the cost is from the silicon used in the solar cell.[14] Silicon is an indirect band gap semi-conductor that requires hundreds of micrometer thick layers of material to achieve sufficient light harvesting[15].

Polycrystalline silicon solar panels range between 17% and 21.5% efficiency with efficiency loss attributed to the polycrystalline character of the silicon material, where defects within the crystal lattice creates traps that allow for electron-hole pairs to recombine[16]. These solar cells are cheaper that monocrystalline solar cells because less waste is produced in the manufacturing process. However, they are more sensitive to photo corrosion have a lower surface area to efficiency ratio.[17]

Monocrystalline silicon solar cells have recently reached 25% efficiency in the lab[18] and have a commercial efficiency up to 21.5%.[19] Monocrystalline silicon has a uniform crystal lattice, without defects or grain boundaries. This results in higher efficiencies from the fewer electron-hole pair recombination events that would otherwise occur from defects in the crystal lattice. Monocrystalline silicon is also the leading material in PV systems, accounting for 36% of the total market in 2013.[20] These systems are more expensive than polycrystalline solar panels, and are more sensitive to partial shading conditions which would damage the solar cell.

Second Generation Photovoltaic Systems

Second generation PV systems are more diversified, including amorphous silicon solar cells, DSSC, perovskite solar cells, multi-junction solar cells, and CdTe solar cells. These systems use thin film technology which use less material that results in cost savings. Second generation solar cells systems have recently reached 20% efficiency[21] for single junction solar cells and 40% efficiency[22] for multi-junction solar cells. Second generation photovoltaic systems are generally synthesized using chemical vapor deposition, which is time consuming and costly.[23]

Amorphous silicon solar cells are considered second generation because they utilize thin film technology. Amorphous silicon has the benefit of containing vacancies within the silicon crystal lattice, which allows for various elements to be added or doped into the material.[24] Elemental doping of the silicon allows for better tuning of the silicon band gap, and has reached 15% efficiency. While the overall efficiency has decreased, the amount of material used in these systems is significantly less than first generation silicon solar cells.[25]

DSSC use hybrid organic-inorganic molecules that typically consist of an inorganic metal ion with aromatic organic ligands that form 'dyes.' These dyes include naturally occurring anthocyanin[26,27,28] and synthetic dyes[29,30,31,32]. Anthocyanin dyes are found in plants as the color component of most leaves and flowers that are cheap and simple to extract, but produce low photon-electron conversion efficiencies that are below 3%.[26,27,28] Synthetic dyes use a variety of aromatic, sulfur, and carboxylic groups to achieve higher efficiencies up to 15%[33], but are more costly than naturally occurring anthocyanin. Both systems use nano-thin layers of materials,[34,35] but often use rare metals including ruthenium[36,37,38], iridium[39], and sometimes toxic metals such as lead[33].

Perovskite solar cells use perovskite crystal structures that contain hybrid organic-inorganic materials. The inorganic materials include either environmentally toxic lead[40,41,42] or health hazardous tin[43,44] metals. The organic component consists of an organic methylammonium ion[45] and halide counter anions[46] that can be replaced with other organic molecules and halide ions to further alter the band gap of a given cell. Since the discovery of perovskites for PV use in 2009, photon to electron conversion efficiencies have risen from 3.8%[46] to 20.1% efficient in 2014,[47] with the most efficient systems using lead as the photocatalyst.[48] These PV systems are not yet commercially available.

Multi-junction solar cells use multiple layers of various materials of different band gaps to maximize light harvesting. These materials have reached 40% light harvesting efficiency using a GaInP/GaInAs/Ge design, with band gaps of 1.86 eV, 1.4 eV, and 0.65 eV, respectively.[22] The high efficiencies are a result of dividing the solar spectrum into three segments, which reduces energy lost as heat when a photon exceeds the band gap. This is achieved from the photons that are of insufficient energy to be absorbed by the GaInP layer that may be absorbed by the GaInAs, and those photons that do not have sufficient energy to be absorbed by the GaInAs layer may be absorbed by the Ge base layer. However, these cells are difficult to manufacture as each layer of material must have the same crystal lattice structure, produce the same operating voltage and current, and be relatively free of defects and impurities. These cells are not yet commercially available.

CdTe solar cells have reached 19.6% efficiency.[49] This PV system is available commercially, and accounts for over half of all thin film solar cells.[50] Cadmium is a byproduct of zinc refining, and the use of cadmium in solar cells offers a beneficial use for the Cd by-product material is energy productive,[51] but the PV cells must be disposed of or recycled properly. The major limiting factor of CdTe solar cells is the use of Tellurium, which has the same natural abundance of platinum and contributes significantly to the both cost and manufacturing limitation of CdTe solar cells.[52] Some of the tellurium may be replaced with sulfur and selenium anions in a CdTe/CdS or CdTe/CdSe design, but at the cost of reduced efficiency to 14.0%.[53] Significant reduction in efficiency to 4.22% is observed when tellurium is omitted in a third generation CdS/CdSe solar cell design.[54]

Third Generation Photovoltaic Systems

Third generation PV systems use nanoparticles to increase the photon to electron conversion efficiency of solar cells.[18] The increased efficiency is based on the quantum confinement effects, where band gaps depend on particle size and allows for fine tuning of the band gap energy. As particle size decreases the band gap energy increases because the energies within the band structure that applies to a bulk material becomes discreet as the nanoparticle becomes smaller and there are fewer atomic orbitals available to form the overlapping molecular orbital energies.

Some examples of third generation solar cells are nanoparticle doped thin films, nano-wires, colloidal quantum dots (CQD), organic-inorganic hybrid CQD, and the bio-inorganic molecule ferritin.[5,55,56] The nanoparticle nature of these materials have enhanced photon to electron conversion as a result of changing particle size and may use benign earth abundant metals. Additionally, these systems are often synthesized using wet chemistry techniques, whereas second generation solar cells requires costly and time inefficient vapor deposition for manufacturing.

Copper, silver, and gold nanoparticles have a unique surface plasmon resonance (SPR). The SPR is a result of the atomic orbitals of the elements interacting and perturbing the incident wavelengths of light, and produces a change in the wavelength or color of light that is emitted. The addition of silver nanoparticles to a GaAs solar cell increases the efficiency by 8%.[57] The addition of gold nanoparticles to a DSSC solar cell significantly increased the efficiency, but failed to report the efficiency increase.[58] The DSSC AuNP paper did note that the increase in efficiency was directly correlated to the SPR signal of the AuNP, which may have also had a synergistic effect with the titanium oxide substrate.

Nano-wire solar cells use non-spherical or rod-like nanomaterials to increase efficiency. The nano-rod shape give the advantages of decreased reflection, increased light trapping, band gap tuning, and a greater tolerance for defects in the mineral structure.[59] These systems have been demonstrated in DSSC systems and have reached 1.5% efficiency.[60] The limiting factor in DSSC and organic-inorganic systems is the ability to diffuse or separate the electron-hole pairs from one another. The efficiency of these systems was increased as the length to width ratio reached a 5:1 ratio. Further increases in efficiency are predicted if the synthesis could yield longer nano-rods.[60]

Colloidal quantum dot (CQD) solar cells use a wide range of materials to replace silicon and CdTe solar cells. Within the same material, size and shape dictate the range of available band gap energies that can be used for photocatalytic charge separation.[61] These cells have been theorized to reach up to 66% efficiency[62], but have only been demonstrated to have up to 8.7% efficiency[63]. Materials common in CQDs include indium phosphide (InP), TiO_2, CdSe, and PbS. While these systems offer promise in terms of ease of synthesis and natural abundance of elements, they have yet to achieve any appreciable photon-to-electron conversion efficiency.

Hybrid systems combine the previously mentioned inorganic CQDs with organic ligands to improve separation between electron-hole pairs. In select cases, these systems have theoretic efficiencies of 45%, but have only demonstrated 0.49% efficiency.[64] These systems are primarily limited by the ability of the ligand to effectively move the holes left behind from the electron-hole pair[65], while maintaining the integrity of the CQD.[66] QD-Protein complexes have provided a method for solubilizing QDs for a significant period of time, while maintaining the absorption and fluorescent properties of the original QDs.[66,67] These systems have been used in conjunction with imaging, labeling, and sensor applications in medical techniques, but the theories and ideas also apply to QD solar cells and are namely solubility of the QDs while maintaining photon absorption properties of the QDs.

Ferritin is a third generation PVS that is an organic-inorganic hybrid which contains benign and earth abundant iron oxide nanoparticle that measure 8 nm in diameter. The organic protein component maintains the solubility of otherwise insoluble metal oxide nanoparticles, while maintaining and repairing the integrity of the nanoparticle that would normally degrade from photo-corrosion. The overall ferritin system can be organized into three-dimensional architectures for enhanced efficiency.[68] The iron oxide core can also be replaced with other metals that would allow for a greater diversity of band gaps that could create a multi-junction solar cell.[5]

Ferritin Background

Ferritin is a sphere-like biomolecule (Figure 1-1) which is found in virtually all organisms and was first discovered by Vilem Laufberger.[69] Ferritins primary role is to store iron as a ferrihydrite mineral, $(Fe^{III})_2O_3 \cdot 0.5H_2O$ (referred to as Fe(O)OH for convenience).

The protein is composed of 24 subunits when assembled weighing 450 kDa. Each subunit is either a heavy (21 kDa) or light (19 kDa) chain commonly referred to as H- and L-ferritin. Each chain has a specific role for the ferritin macromolecule; H-ferritins contain a ferroxidase center, where metal ions are oxidized from their 2^+ to 3^+ state,[70] L-ferritin's primary role is the nucleation site for mineralization[71,72] and has recently been shown to contain an important electron transport chain, which facilitates electron import and export for iron loading and demineralization, respectively.[73] Variations in the H:L ferritin ratios are observed in different tissues which affects the macromolecules ability to bind and store iron.[74,75]

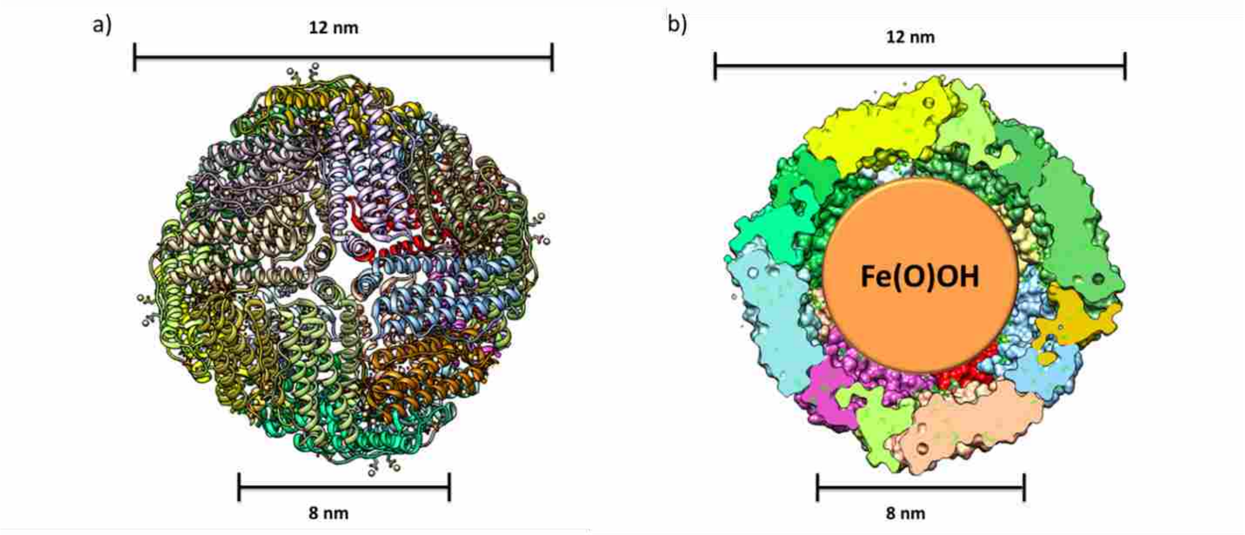

Figure 1 - 1. A computer generated model of human H-ferritin homopolymer. a) shows a ribbon diagram of the protein, and b) shows a cross section with a ferrihydrite mineral on the interior of the protein. The protein

measures 12 nm in diameter with an 8 nm interior that is either hollow (apoferritin) or with a mineral core (holo-ferritin). Model generated using UCSF Chimera software package PDB code 1FHA.

Ferritin subunits maintain the same basic structure across various organisms.[76,77] These subunits are comprised of four main ɑ-helices with a fifth smaller helix, see Figure 1-2.

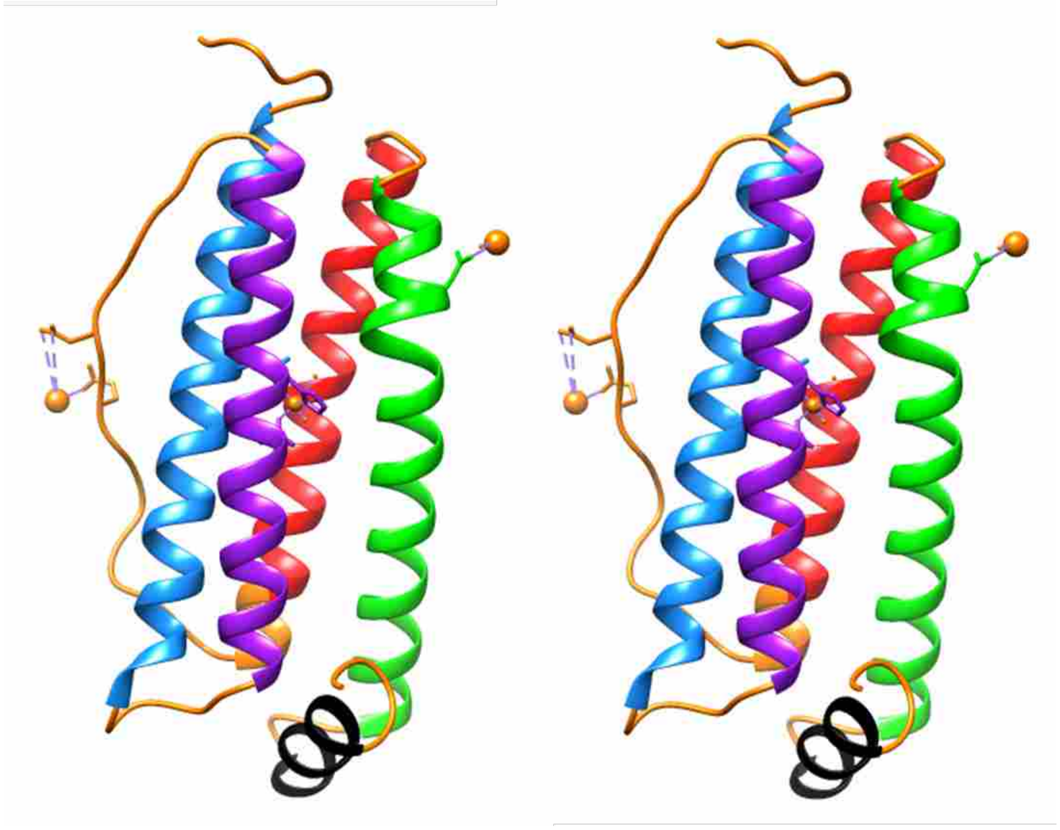

Figure 1 - 2. Stereogram of a ferritin H-chain subunit with colored alpha helices. The single subunit is of human H-chain ferritin showing the 4 main helix structures with a smaller 5th helix. Helix 1 is shown in **Blue**, Helix 2 is **Purple**, Helix 3 is **Red**, Helix 4 is **Green**, and Helix 5 is **Black**. Loops that connect the helices are shown in brown. Graphic was produced using UCSF Chimera package PDB code 1FHA.

When ferritin is assembled it contains channels along the 3-fold and 4-fold axis that allows ions to traverse the 2 nm thick protein shell. The 3-fold channel is hydrophilic[78] consisting of three aspartates and three glutamates. The 3-fold channel is a know metal binding site for divalent and trivalent metals (Cd^{2+}, Zn^{2+}, Tb^{3+}, Ca^{2+})[79,80,81,82]. This 3-fold channel has also been suggested as the site of iron entry[83], and contain three cysteine residues at the channel entrance. Substitution to the carboxylate residues inhibits iron loading into ferritin.[84,85] Additionally, cations are attracted to the exterior portion of the 3-fold channel which contains negative residues in and near the channel surrounded by portions of positive potential.[83] The 4-fold channel is hydrophobic and is suggested to be the location where anions are able to enter and leave the protein.[5,79]

After ferrous iron enters the protein interior, it is oxidized at the ferroxidase center's active site that is located at the center of the H-chain's 4 ɑ-helix bundle (See Figure 1-3).[86] The active site coordinates the iron using several amino acid residues contributed from each ɑ-helix. The pathway from the ferroxidase center on H-chain ferritin, to the nucleation sight on L-chain ferritin has been an area of recent investigation.[86] Theil et al.[87] later found that ferric iron travels parallel to an ɑ-helix until it reaches the short 5th ɑ-helix, which has a 60° angle, that may guide the ferric iron to the mineralization cavity in L-chain ferritin.

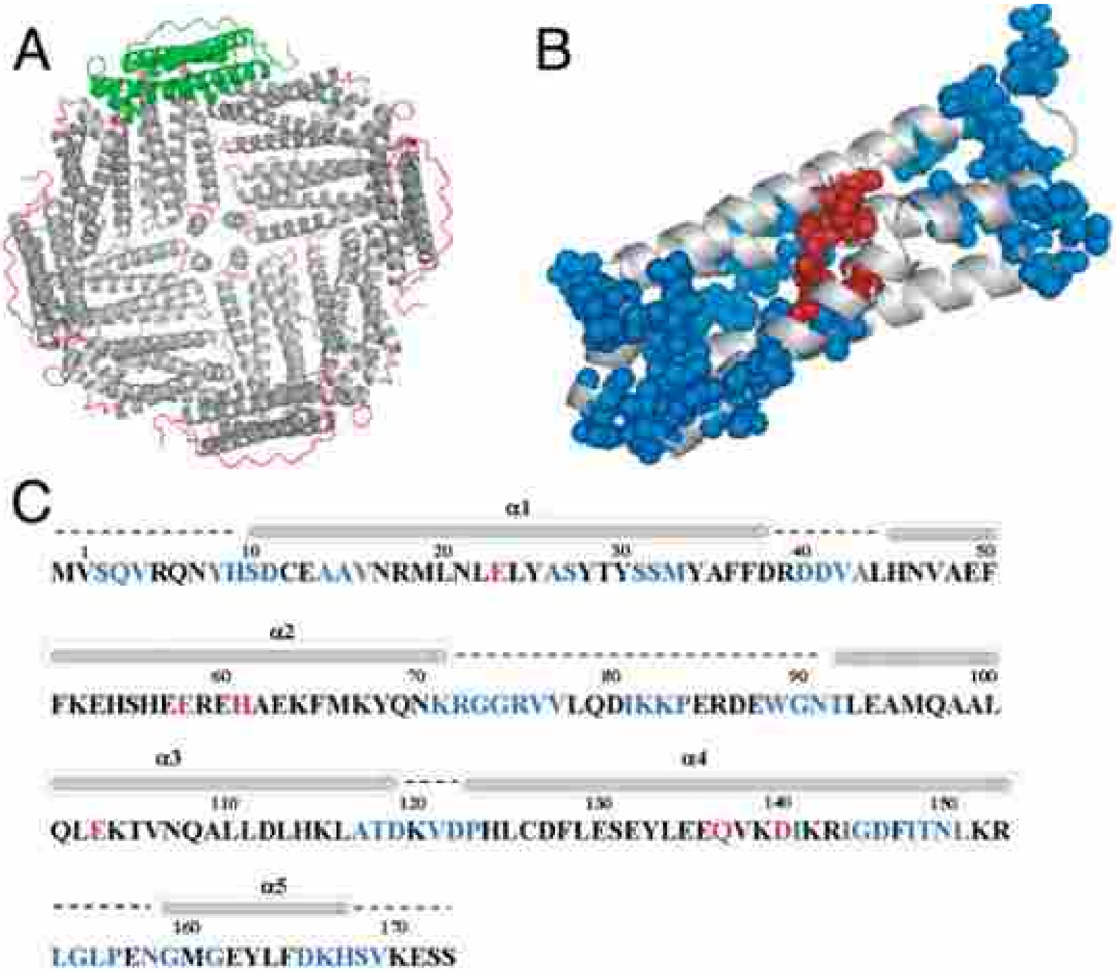

Figure 1 - 3. Sequential assignment of ferritin by solid-state NMR. (A) 3D structure of recombinant frog (*R. caesbeiana*) M ferritin (24 subunit, PDB 1MFR; PyMOL 0.99rc5). The four-helix-bundle subunits are displayed as gray helices and red loops. The green subunit illustrates the orientation of one monomeric ferritin subunit along the surface of the hollow sphere. (B) representation of the four-helix-bundle subunit NMR-assigned residues (blue spheres) and ferroxidase residues (red spheres). (C) Primary and secondary structure from M ferritin-ferroxidase site residues (red front), NMR sequence specific assigned residues (blue font), α-helices (bars), and loops (broken lines). From reference 86.

Ferritin BioMaterial Synthesis and Characterization.

While the majority of ferritin research has been to understand the mechanism by which ferritin stores and releases iron in biological applications,[88,89,90,91,92] research has also been conducted using ferritin's ability to function as a nanocage for storing and mineralizing metal nanoparticles inside an organic framework. A variety of metal nanoparticles have been synthesized inside ferritin and include: various metals[93], metal oxides[94,95,96,97,98], metal sulfides[99], and II-VI[100] semiconductor materials. The ability to form these materials as uniform 8 nm spheres provides special physical and chemical properties. My research concerns the synthesis and characterization of various metal oxides with additions of various anions and investigates their respective properties for applications in electrochemical, photochemical and bio-nano-propellant applications.

Metal Oxide Synthesis in Ferritin

There are three main reactions schemes to load metal oxides into ferritin, 1) metal loading using ferritin's ferroxidase center, 2) metal loading using UV light to assist in metal loading, 3) a metal is diffused into ferritin interior followed by addition of sulfide or other chalcogen under anaerobic conditions.

Ferroxidase Center Loading

Ferroxidase center loading begins by adding a 2^+ oxidation state transition metal that is further oxidized by the protein's ferroxidase center, creating a 3^+ metal on the interior of the protein. The metal is sequestered as a metal oxy-hydroxide, or M(O)OH. This process works for those metals that have similar redox properties as iron, such as cobalt and manganese.

UV Light Assisted Metal Loading

A second class of ferritin synthesis reactions is accomplished by using UV light to photocatalyze the metal loading process. [97] In a paper by Klem et al.[97], titanium (IV), europium (IV), and iron (III) citrates were loaded into ferritin. The metal-citrate salts were placed into a solution containing apoferritin followed by addition of UV light, this photoreduced the metal by citrate oxidation which assisted in the metal loading process. Oxygen was required to load the metal-citrate complexes when exposed to UV light, which suggests that the ferroxidase center may be required for loading these metals into ferritin.

Metal Diffusion into the Ferritin Interior

A third class of ferritin loading reactions is when a metal or metal salt (transition or otherwise) is reacted with sulfide (or other chalcogen) under anaerobic conditions in the presence of apoferritin.[99,101] A non-ferrous metal is first given several minutes to enter the interior of apoferritin by diffusion followed by a stoichiometric addition of sulfide, which forms a metal sulfide on the interior. This process is repeated several times until the desired core size is reached.

Sulfur and Anion Deposition Into Ferritin

The iron-oxide mineral in ferritin has also been used as a scaffold to alter the anion content within ferritin. The counter ion to the iron metal can be modified using two known processes, and include sulfide reduction[99] and anion deposition [102, 135].

Iron Sulfide Reduction

The iron oxide in ferritin can be chemically reduced with sulfide to produce an iron sulfide mineral.[99] Sodium sulfide under anaerobic conditions is added to the ferrihydrite mineral in ferritin, forming a new iron-sulfide mineral. If oxygen is present, the iron-sulfide core will re-oxidize and reform the ferrihydrite mineral and release the sulfide from the mineral. The resulting iron-sulfide mineral has an oxidation state of 2.5^+,[99] and the band gap for this material is thought to be 0.95 eV.[94]

Surface Deposition and Mineral Deposition of Anions

The ferrihydrite mineral can be altered by depositing anions onto the mineral's surface or throughout the mineral. Native ferritin contains a phosphate layer that constitutes about 10% or 1 phosphate for every 10 irons in the native ferrihydrite mineral.[103,104,105] It has been speculated that the purpose of the phosphate is to increase the solubility of the ferrihydrite mineral from a K_{sp} of 10^{-36} to approximately 10^{-22}.[106] The phosphate is thought to enter ferritin through either a co-deposition process during iron loading or that the anions are able to transverse through gated pores in the protein.[107]

It was shown by Polanams et al.[108] that oxo-anions can be co-deposited into the ferrihydrite mineral during iron loading. Therein, apoferritin was placed into solutions containing 1 mM sodium oxo-anion and apoferritin. Ferrous iron was then added in stoichiometric amounts for target cores of 2000 Fe/ferritin. These anions were found to load anywhere between a 1:1 and 5:1 iron to anion ratio.

The co-deposition of various anions was also measured by Colton et al.[134] who observed a red shift in the band gap of the ferrihydrite mineral, and is attributed to a combination of the electronegativity of the anions and ability of the anions to associate with the ferrihydrite mineral.

Ferritin Photochemistry

Ferritin's photochemical applications have been an area of recent investigation.[94,109,110,111] The ferrihydrite mineral in ferritin has been shown to photoreduce

Au(III) to Au(0)[110], Cr(VII) to Cr(III)[109], Cu(II) to Cu(0)[112], Ag^+ to Ag(0)[113] and Hg_2(II) to Hg(0)[113]. In the paper by Keyes et al.[110] they describe a model for ferritin's photo-catalytic reduction of Au(III) ions to gold nanoparticles. They explain that the Au(III) ions are attracted to sulfur containing groups on the exterior of the protein which acts as nucleation sites, and is different from the nucleation sites located on the interior of L-chain ferritin for metal oxide mineralization.

Mechanism of Gold(III) Reduction

The photochemical excitation from the UV light source creates an electron-hole pair in the ferrihydrite mineral. The excited electron then traverses the ferritin protein shell to reduce the Au(III) ions. The electron transfer process from the interior to the exterior of the protein can proceed through one of three processes: the electron can tunnel through the 2 nm shell, it can travel along two metals that are in the 3-fold channel, or the electrons can travel through an electron transport chain located in the L-ferritin.

The holes left behind by the reaction are filled by citrate oxidation. The initial gold nanoparticle acts as a nucleation site that attracts more Au(III) ions, which in turn are reduced and deposited onto the growing gold particle. In some cases, the reaction yielded gold nanoparticle formation on the interior of ferritin; however the majority of gold nanoparticles were formed on the exterior of ferritin.

The ferrihydrite mineral in ferritin remains stable or intact during this photocatalytic reaction.[114] This is due to ferritins ability to re-oxidize the photo-corroded iron back to a stable ferrihydrite mineral. This aspect was demonstrated by Kim et al.,[114] where the ferrihydrite mineral in ferritin was able to be regenerated many times over without losing catalytic efficiency. When using bare ferrihydrite or other iron-oxide nanoparticles, the iron was able to photocatalytically reduce Cr(IV) to Cr(III) until an insoluble and inactive iron oxide was formed.[114] The iron-oxide ‘rust’ formed an insoluble complex with hydroxide which can no longer participate in further photochemical reactions.

Ferritin is able to maintain the integrity of the photocatalytic nanoparticle, and as long as a chelator is not present the iron will remain inside the protein. The ability of the ferritin protein to re-mineralize and maintain the integrity of the ferrihydrite mineral during photocatalytic processes overcomes the photocorrosion problems facing PV systems.

Excitation Lifetimes

The band gaps within the ferritin’s metal oxide mineral reacts with UV light to create an excited electron (exciton) which is sufficiently long-lived to react with electron donors/acceptors in solution[115]. Nikandrov et al[115] reported that band gap excitation of ferrihydrite in ferritin leads to generation of electron-hole pairs that are sufficiently long lived to allow the excitons to react with other molecules in solution. Ferritin photoreduction of propylviologen occurred 4 μs after laser excitation of the ferrihydrite core. In comparison, charge recombination in bare hematite nanoparticles (closely related to ferrihydrite) occurs in 2 ps.[116] This is a 2000-fold increase in lifetime of the excitons when the particles are encapsulated in ferritin. The ability of ferritin to stabilize the excitons against charge recombination may occur either because the oxidation of electron donors in the surrounding medium is so rapid that the holes in the nanoparticle are filled, thus preventing the exciton from leaving the conduction band, or because the protein shell is redox active and can accept electrons, thus transferring them to a different physical location. A similar process is observed in dye-sensitized solar cells, where the exciton is moved from the metal cluster to the ligand through a metal-to-ligand electron transfer process.[117]

Band gaps – Origin and Explanation

A band gap is defined as the energy spacing between a material's valence band and conduction band.[118] These bands are formed from the overlap of many molecular orbitals of the solid material. As the number of atoms increases in the solid a large number of molecular orbitals become closely spaced until bands are formed (Figure 1-4). Multiple bands are formed from the interacting atomic and molecular orbitals. These bands govern a metal's thermal, electrical, and optical properties of a material originate from the conduction and valence band. The relative spacing between the two bands has a large impact in whether a material is an electrical and thermal insulator (large spacing), semi-conductor (small spacing), or conductor (little to no spacing). Electrons are able to jump from lower to higher bands as long as sufficient energy is applied, and a vacancy exists in the upper band. In the case of a PVS or a photocatalyst a photon is used to induce an electronic transition between bands. Within semiconductor physics, the band gap is always one of two types, either a direct band gap or an indirect band gap.

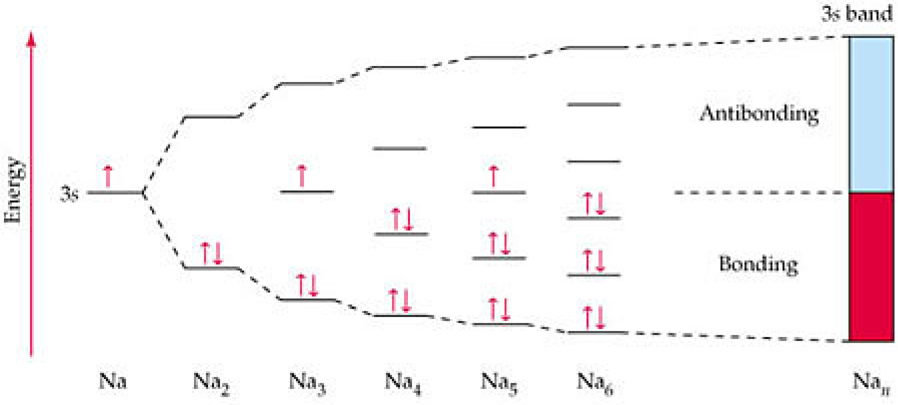

Figure 1 - 4. Molecular orbital energy-level diagram sodium metal with increasing number of atoms. As the number of orbitals increasing in the molecular solid, the spacing between energy levels decrease until bonding and antibonding bands are formed. In this example, sodium is a good conductor. Figure provided by Reference 119.

A direct band gap is when an electronic transition occurs directly, without the need for a k-vector, or vibrational energy. DSSCs are an example of a direct band gap material. The excitation between bands occurs rapidly as the energy from a photon is easily absorbed. The high efficiency of direct transitions allows for very thin layers of high performance materials. However, most DSSCs and thin film materials use rare or toxic materials, making their use environmentally and economically prohibitive.[120,121,122,123]

An indirect band gap is when an electronic transition requires both a photon of sufficient energy and a phonon or vibrational energy to cause the excitation. A transition in an indirect band gap material tends to be less probable, as it requires two different energy inputs to allow for the transition to occur. Silicon based solar panels are an example of an indirect band gap material. These indirect band gap solar panels require significantly more material than their direct band gap counterparts, often requiring several millimeters of materials to achieve efficient photon absorption. Older solar panels contained more earth abundant elements such as Cd, Te, and Se to improve efficiencies, which are environmentally hazardous materials[124,125], however, the use of these metals has been replaced by other materials.

Ferritin Band Gap Measurements

The band gap values for the metal oxide minerals in ferritin that have been previously reported very greatly. These band gaps were measured using a variety of techniques, including a photochemical assay using optical filters to find the optimum color of light that allows for the photochemical process to occur, and a scanning tunneling microscopy technique to probe surface states of the ferrihydrite mineral.

Optical Filter Chemical Assay Band gap Determination

Two photochemical assay papers find the photochemically active band gap of the ferrihydrite mineral to be between 2.5-3.5 eV[126] and 3.0-3.5 eV[110]. In these papers a photochemical reduction assay was performed to measure at which wavelengths a photochemical reduction occurred. The assay used native ferritin in the presence of a citrate solution (electron donor) and an electron acceptor which is used as the colorimetric assay (Cr(VI) to Cr(III)[114] or Au(III) to Au(0)[110]). Under UV light (3.1-10 eV) an electron-hole pair is formed inside of the ferrihydrite mineral in ferritin. The excited electron then reduces the electron acceptor in solution, and the hole is filled by citrate oxidation. This process only worked in the near-UV to UV region of the illumination spectrum. Of the two techniques discussed herein, I consider this technique to be a more correct method for measuring band gaps of materials as a chemical assay was used to determine the approximate band gap of the ferrihydrite mineral.

Scanning Tunneling Spectroscopy

A paper by Rakshit et al.[127] used scanning tunneling spectroscopy (STS) to measure the band gaps in ferritin, reporting “band gap energy” of 1.00 eV, without distinction between direct or indirect band gaps, and without showing errors in their measurements. It should be noted that this technique is improper for measuring the properties of a bulk material.

STS experiments, also known as scanning tunneling microscopy (STM) are used to measure the topography of a surface much like scanning electron microscopy (SEM), only at much higher resolution (0.01 nm with STM[128] compared to 5 nm with SEM[129]).[130] The technique works by scanning a surface with a piezoelectric tip in a raster pattern which measures a current at constant voltage. The concept is based off of ‘quantum tunneling,[131,132] where a conductive tip is brought very close to the surface of a material (less than 2 nm), and the applied voltage creates a tunneling current from the atom’s atomic orbitals interacting with the piezoelectric tip. The electrical current recorded from the tip is in direct relation to the height of the sample, which can then be used to reconstruct the location of the atoms or molecules on a material's surface.[133]

STM experiments probe the surface state of atoms, finding their relative position in space. Measuring a bulk property, such as a band gap, would be impractical with this technique, as the electrons would always take the path of least resistance. The electron measured would need to travel through the protein's tunneling barrier (2 nm), through the mineral (8 nm), through the protein a second time (2 nm), and into the gold conducting layer. A more likely explanation for the reported values by Rakshit et al.[127] is that the electric current traveled over surface of the protein or across the metal's exterior surface, and the measured current was based off of the surface states that the electrons passed over.

Optical Absorption Spectroscopy

Optical absorption spectroscopy (OAS) is a common method used to determine band gaps in semi-conductors. Band gap energy of ferritin, finding that ferritin is an indirect semiconductor with an indirect band gap of 2.140 eV and a direct transition at 3.053 eV. [134] This technique has also been used to find variations in the band gap as a result of core size and anion co-deposition[135], as well as resolving the band gaps of non-native metal oxides inside ferritin[10] (which also corrected previously reported results by Rackshit et al.[127]) The details of these experiments and results are given in Chapters 3, 4, and 5 herein.

Conclusion

Ferritin provides a model for creating and investigating the properties of metal oxide nanoparticles for use in PVS, nanobatteries, and energetic materials. By maintaining solubility as well as fine tune control of the anion content of metal oxide nanoparticles, new and previously difficult to measure properties can be investigated.

References

---

[1] World energy outlook, available via http://www.iea.org/media/weowebsite/2008-1994/WEO2008.pdf

[2] Available at http://www.eia.gov/todayinenergy/detail.cfm?id=12251

[3] Available at http://www.ecoworld.com/energy-fuels/how-much-solar-energy-hits-earth.html

[4] Available at http://www.nrel.gov/ncpv/images/efficiency_chart.jpg.

[5] Watt, R. K., Petrucci, O. D. & Smith, T. Ferritin as a model for developing 3rd generation nano architecture organic/inorganic hybrid photo catalysts for energy conversion. *Catal. Sci. Technol.* **2013**. *3,* 3103–3110.

[6] W. Shockley, H. Queisser, Detailed Balance Limit of Efficiency of p-n Junction Solar Cells. *J App. Phys.* **1960.** *32,* 510-519

[7] C Clarke. San Jose Solar Company Breaks Efficiency Record for PV. KCET. http://www.kcet.org/news/rewire/solar/photovoltaic-pv/san-jose-solar-company-breaks-efficiency-record-for-pv.html (March 2013)

[8] Available at http://cleantechnica.com/2014/02/02/which-solar-panels-most-efficient/

[9] Richard D. Schaller, Milan Sykora, Jeffrey M. Pietryga, and Victor I. Klimov. Seven Excitons at a Cost of One: Redefining the Limits for Conversion Efficiency of Photons into ChargeCarriers. *Nano Lett.,* **2006**, *6,* 424-429

[10] Erickson, S. D., Smith, T. J., Moses, L. M., Watt, R. K. & Colton, J. S. Non-native Co-, Mn-, and Ti-oxyhydroxide nanocrystals in ferritin for high efficiency solar energy conversion. *Nanotechnology* **26,** 015703 (2015).

[11] King, R. R. *et al.* 40% efficient metamorphic GaInP⁄GaInAs⁄Ge multijunction solar cells. *Applied Physics Letters* **90,** 183516 (2007).

[12] Available at http://instituteforenergyresearch.org/analysis/tough-times-may-be-ahead-for-residential-solar-panels/ Accessed June 12, 2015

[13] Available at https://www.nerdwallet.com/blog/finance/money-nerd/green-living/save-money-putting-solar-panels-roof/ Accessed June 12, 2015

---

[14] Available at http://www.solar-states.com/breaking-down-the-cost-of-solar/. Accessed June 29, 2015.

[15] Rath, J. . Low temperature polycrystalline silicon: a review on deposition, physical properties and solar cell applications. *Solar Energy Materials and Solar Cells* **76,** 431–487 (2003).

[16] Seager, C. H. Grain boundary recombination: Theory and experiment in silicon. *Journal of Applied Physics* **52,** 3960–3968 (1981).

[17] Available at http://energyinformative.org/best-solar-panel-monocrystalline-polycrystalline-thin-film/. Accessed June 24, 2015.

[18] Tyagi, V. V., Rahim, N. A., Rahim, N. A., Jeyraj, A. & Selvaraj, L. Progress in solar PV technology: Research and achievement. *Renewable and Sustainable Energy Reviews* **20,** 443–461 (2013).

[19] Photovoltaics Report, Fraunhofer ISE, July 28, 2014, pages 24, 25

[20] Photovoltaics Report, Fraunhofer ISE, July 28, 2014, pages 18,19

[21] Schmidtke, J. Commercial status of thin-film photovoltaic devices and materials. *Optics express* **18,** A477–A486 (2010).

[22] King, R. R., D. C. Law, K. M. Edmondson, C. M. Fetzer, G. S. Kinsey, H. Yoon, R. A. Sherif, and N. H. Karam. 40% efficient metamorphic GaInP⁄GaInAs⁄Ge multijunction solar cells. *Applied Physics Letters* **90,** 183516 (2007).

[23] Guo, L., Kondo, M., Fukawa, M., Saitoh, K. & Matsuda, A. High rate deposition of microcrystalline silicon using conventional plasma-enhanced chemical vapor deposition. *Japanese journal of applied physics* **37,** L1116 (1998).

[24] Carlson, D. E. & Wronski, C. R. Amorphous silicon solar cell. *Applied Physics Letters* **28,** 671–673 (1976).

[25] Kabir, M. I. *et al.* Amorphous Silicon Single-Junction Thin-Film Solar Cell Exceeding 10% Efficiency by Design Optimization. *International Journal of Photoenergy* **2012,** 7 (2012).

[26] Wongcharee, K., Meeyoo, V. & Chavadej, S. Dye-sensitized solar cell using natural dyes extracted from rosella and blue pea flowers. *Solar Energy Materials and Solar Cells* **91,** 566–571 (2007).

[27] Calogero, G. *et al.* Anthocyanins and betalains as light-harvesting pigments for dye-sensitized solar cells. *Solar Energy* **86,** 1563–1575 (2012).

[28] Calogero, G. *et al.* Synthetic analogues of anthocyanins as sensitizers for dye-sensitized solar cells. *Photochemical & Photobiological Sciences* **12,** 883–894 (2013).

---

[29] Joly, D. *et al.* A robust organic dye for dye sensitized solar cells based on iodine/iodide electrolytes combining high efficiency and outstanding stability. *Scientific reports* **4,** (2014).

[30] Qin, P. *et al.* Design of an Organic Chromophore for P-Type Dye-Sensitized Solar Cells. *J. Am. Chem. Soc.* **130,** 8570–8571 (2008).

[31] Hagberg, D. P. *et al.* A novel organic chromophore for dye-sensitized nanostructured solar cells. *Chem. Commun.* 2245–2247 (2006). doi:10.1039/B603002E

[32] Hara, K. *et al.* Design of new coumarin dyes having thiophene moieties for highly efficient organic-dye-sensitized solar cells. *New J. Chem.* **27,** 783–785 (2003).

[33] Burschka, J. *et al.* Sequential deposition as a route to high-performance perovskite-sensitized solar cells. *Nature* **499,** 316–319 (2013).

[34] Wang, Q. *et al.* Efficient Light Harvesting by Using Green Zn-Porphyrin-Sensitized Nanocrystalline TiO2 Films. *J. Phys. Chem. B* **109,** 15397–15409 (2005).

[35] Baranoff, E. *et al.* Cyclometallated Iridium Complexes as Sensitizers for Dye-Sensitized Solar Cells. *Chemistry – An Asian Journal* **5,** 496–499 (2010).

[36] Chou, C.-C. *et al.* Ruthenium(II) Sensitizers with Heteroleptic Tridentate Chelates for Dye-Sensitized Solar Cells. *Angewandte Chemie International Edition* **50,** 2054–2058 (2011).

[37] Chen, C.-Y., Wu, S.-J., Wu, C.-G., Chen, J.-G. & Ho, K.-C. A Ruthenium Complex with Superhigh Light-Harvesting Capacity for Dye-Sensitized Solar Cells. *Angewandte Chemie* **118,** 5954–5957 (2006).

[38] Mayo, E. I. *et al.* Cyclometalated iridium(iii)-sensitized titanium dioxide solar cells. *Photochem. Photobiol. Sci.* **5,** 871–873 (2006).

[39] Baranoff, E. *et al.* Cyclometallated Iridium Complexes as Sensitizers for Dye-Sensitized Solar Cells. *Chemistry – An Asian Journal* **5,** 496–499 (2010).

[40] Christians, J. A., Fung, R. C. M. & Kamat, P. V. An Inorganic Hole Conductor for Organo-Lead Halide Perovskite Solar Cells. Improved Hole Conductivity with Copper Iodide. *J. Am. Chem. Soc.* **136,** 758–764 (2014).

[41] Zhou, H. *et al.* Interface engineering of highly efficient perovskite solar cells. *Science* **345,** 542–546 (2014).

[42] Kim, H.-S. *et al.* Lead Iodide Perovskite Sensitized All-Solid-State Submicron Thin Film Mesoscopic Solar Cell with Efficiency Exceeding 9%. *Sci. Rep.* **2,** (2012).

[43] Hao, F., Stoumpos, C. C., Cao, D. H., Chang, R. P. H. & Kanatzidis, M. G. Lead-free solid-state organic-inorganic halide perovskite solar cells. *Nat Photon* **8,** 489–494 (2014).

---

[44] Liu, M., Johnston, M. B. & Snaith, H. J. Efficient planar heterojunction perovskite solar cells by vapour deposition. *Nature* **501,** 395–398 (2013).

[45] Koh, T. M. *et al.* Formamidinium-Containing Metal-Halide: An Alternative Material for Near-IR Absorption Perovskite Solar Cells. *J. Phys. Chem. C* **118,** 16458–16462 (2014).

[46] Kojima, A., Teshima, K., Shirai, Y. & Miyasaka, T. Organometal halide perovskites as visible-light sensitizers for photovoltaic cells. *Journal of the American Chemical Society* **131,** 6050–6051 (2009).

[47] Available at http://www.rsc.org/chemistryworld/2015/01/new-ion-continues-perovskite-solar-cell-record-flat-out-progress Accessed June 12, 2015

[48] Available at http://www.solarreviews.com/news/lead-out-perovskite-solar-040514/ accessed June 12, 2015

[49] Green, M. A., Emery, K., Hishikawa, Y., Warta, W. & Dunlop, E. D. Solar cell efficiency tables (version 42). *Progress in Photovoltaics: Research and Applications* **21,** 827–837 (2013).

[50] Fraunhofer ISE Photovoltaics Report, July 28, 2014, pages 18,19

[51] Raugei, M. & Fthenakis, V. Cadmium flows and emissions from CdTe PV: future expectations. *Energy Policy* **38,** 5223–5228 (2010).

[52] Available at http://www.nrel.gov/analysis/key_activities_jobs_sup_cstr.html Accessed June 12, 2015

[53] Britt, J. & Ferekides, C. Thin-film CdS/CdTe solar cell with 15.8% efficiency. *Applied Physics Letters* **62,** 2851–2852 (1993).

[54] Lee, Y.-L. & Lo, Y.-S. Highly Efficient Quantum-Dot-Sensitized Solar Cell Based on Co-Sensitization of CdS/CdSe. *Advanced Functional Materials* **19,** 604–609 (2009).

[55] Ip, A. H. *et al.* Hybrid passivated colloidal quantum dot solids. *Nat Nano* **7,** 577–582 (2012).

[56] Andrey L. Rogach. Fluorescence energy transfer in hybrid structures of semiconductor nanocrystals. *Nanotoday* **6,** 355–365 (2011).

[57] Nakayama, K., Tanabe, K. & Atwater, H. A. Plasmonic nanoparticle enhanced light absorption in GaAs solar cells. *Applied Physics Letters* **93,** 121904 (2008).

[58] Tian, Y. & Tatsuma, T. Mechanisms and Applications of Plasmon-Induced Charge Separation at TiO2 Films Loaded with Gold Nanoparticles. *J. Am. Chem. Soc.* **127,** 7632–7637 (2005).

[59] Garnett, E. C., Brongersma, M. L., Cui, Y. & McGehee, M. D. Nanowire solar cells. *Annual Review of Materials Research* **41,** 269–295 (2011).

---

[60] Law, M., Greene, L. E., Johnson, J. C., Saykally, R. & Yang, P. Nanowire dye-sensitized solar cells. *Nat Mater* **4,** 455–459 (2005).

[61] Buhro, W. E. & Colvin, V. L. Semiconductor nanocrystals: Shape matters. *Nat Mater* **2,** 138–139 (2003).

[62] Nozik, A. . Quantum dot solar cells. *Physica E: Low-dimensional Systems and Nanostructures* **14,** 115–120 (2002).

[63] Chuang, C.-H. M., Brown, P. R., Bulović, V. & Bawendi, M. G. Improved performance and stability in quantum dot solar cells through band alignment engineering. *Nat Mater* **13,** 796–801 (2014).

[64] Plass, R., Pelet, S., Krueger, J., Grätzel, M. & Bach, U. Quantum Dot Sensitization of Organic−Inorganic Hybrid Solar Cells. *J. Phys. Chem. B* **106,** 7578–7580 (2002).

[65] Kwak, J. *et al.* Bright and Efficient Full-Color Colloidal Quantum Dot Light-Emitting Diodes Using an Inverted Device Structure. *Nano Lett.* **12,** 2362–2366 (2012).

[66] Chan, W. C. Luminescent quantum dots for multiplexed biological detection and imaging. *Current Opinion in Biotechnology* **13,** 40–46 (2002).

[67] Medintz, I. L., Uyeda, H. T., Goldman, E. R. & Mattoussi, H. Quantum dot bioconjugates for imaging, labelling and sensing. *Nature materials* **4,** 435–446 (2005).

[68] Chu, Sang-Hyon, Sang H. Choi, Gerald D. Watt, Jae-Woo Kim, Yeonjoon Park, Robert C. Davis, John N. Harb, Glen C. King, and Peter T. Lillehei. Fabrication of cell structures for bionanobattery. *Smart Struct. Mat.* **5389**, 443–451 (2004).

[69] Laufberger, V. Sur la cristallisation de la ferritine. *Bull. Soc. chim. biol* **19,** 1575–1582 (1937).

[70] Hentze, M. W. *et al.* Cloning, characterization, expression, and chromosomal localization of a human ferritin heavy-chain gene. *Proceedings of the National Academy of Sciences* **83,** 7226–7230 (1986).

[71] Vidal, R. *et al.* Expression of a Mutant Form of the Ferritin Light Chain Gene Induces Neurodegeneration and Iron Overload in Transgenic Mice. *The Journal of Neuroscience* **28,** 60–67 (2008).

[72] Wade, V. J. *et al.* Influence of site-directed modifications on the formation of iron cores in ferritin. *Journal of Molecular Biology* **221,** 1443–1452 (1991).

[73] Carmona, U., Li, L., Zhang, L. & Knez, M. Ferritin light-chain subunits: key elements for the electron transfer across the protein cage. *Chem. Commun.* **50,** 15358–15361 (2014).

[74] Dickey, L. F. *et al.* Differences in the regulation of messenger RNA for housekeeping and specialized-cell ferritin. A comparison of three distinct ferritin complementary DNAs, the

corresponding subunits, and identification of the first processed in amphibia. *Journal of Biological Chemistry* **262,** 7901–7907 (1987).

75 Zecca, L. et al. Iron, neuromelanin and ferritin content in the substantia nigra of normal subjects at different ages: consequences for iron storage and neurodegenerative processes. Journal of Neurochemistry **76,** 1766–1773 (2001).

76 Theil, E. C. Ferritin: structure, gene regulation, and cellular function in animals, plants, and microorganisms. *Annual review of biochemistry* **56,** 289–315 (1987).

77 Andrews, S. C. *et al.* Structure, function, and evolution of ferritins. *Journal of Inorganic Biochemistry* **47,** 161–174

78 S Levi, P Santambrogio, B Corsi, A Cozzi & P Arosio. Evidence that residues exposed on the three-fold channels have active roles in the mechanism of ferritin iron incorporation. *Biochem. J.* 467–473 (1996).

79 Ford, G. C. *et al.* Ferritin: Design and Formation of an Iron-Storage Molecule. *Philosophical Transactions of the Royal Society of London. B, Biological Sciences* **304,** 551–565 (1984).

80 Rice, D.W., Ford, G.C., White, J.L., Smith, J.M.A. and Harrison, P.M. (1983) Advanc. Inorg. Biochem. 5, 39-50

81 Lawson, D. M. *et al.* Solving the structure of human H ferritin by genetically engineering intermolecular crystal contacts. *Nature* **349,** 541–544 (1991).

82 Wardeska, J. G., Viglione, B. & Chasteen, N. D. Metal ion complexes of apoferritin. Evidence for initial binding in the hydrophilic channels. *Journal of Biological Chemistry* **261,** 6677–6683 (1986).

83 Chasteen, N. D. & Harrison, P. M. Mineralization in Ferritin: An Efficient Means of Iron Storage. *Journal of Structural Biology* **126,** 182–194 (1999).

84 A Treffry *et al.* Defining the roles of the threefold channels in iron uptake, iron oxidation and iron-core formation in ferritin: a study aided by site-directed mutagenesis. *Biochem. J.* 721–728 (1993).

85 Sonia Levi, Paolo Santambrogio, Barbara Corsi, Anna Cozzi & Paolo Arosio. Evidence that residues exposed on the three-fold channels have active roles in the mechanism of ferritin iron incorporation. *Biochem. J.* **317,** 467–473 (1996).

86 Turano, P., Lalli, D., Felli, I. C., Theil, E. C. & Bertini, I. NMR reveals pathway for ferric mineral precursors to the central cavity of ferritin. *Proceedings of the National Academy of Sciences* **107,** 545–550 (2010).

87 Theil, E. C., Liu, X. S. & Tosha, T. Gated pores in the ferritin protein nanocage. *Inorganica Chimica Acta* **361,** 868–874 (2008).

---

[88] Bartzokis, G. & Tishler, T. MRI evaluation of basal ganglia ferritin iron and neurotoxicity in Alzheimer's and Huntingon's disease. *Cellular and molecular biology (Noisy-le-Grand, France)* **46,** 821–833 (2000).

[89] Dexter, D. T. *et al.* Decreased Ferritin Levels in Brain in Parkinson's Disease. *Journal of Neurochemistry* **55,** 16–20 (1990).

[90] Van Reeth, C. *et al.* Serum ferritin and isoferritins are tools for diagnosis of active adult Still's disease. *The Journal of rheumatology* **21,** 890–895 (1994).

[91] Curtis, A. R. J. *et al.* Mutation in the gene encoding ferritin light polypeptide causes dominant adult-onset basal ganglia disease. *Nat Genet* **28,** 350–354 (2001).

[92] Dexter, D. T. *et al.* Alterations in the levels of iron, ferritin and other trace metals in parkinson's disease and other neurodegenerative diseases affecting the basal ganglia. *Brain* **114**, 1953–1975 (1991).

[93] Ensign, D., Young, M. & Douglas, T. Photocatalytic Synthesis of Copper Colloids from Cu(II) by the Ferrihydrite Core of Ferritin. *Inorg. Chem.* **43,** 3441–3446 (2004).

[94] Watt, R. K., Petrucci, O. D. & Smith, T. Ferritin as a model for developing 3rd generation nano architecture organic/inorganic hybrid photo catalysts for energy conversion. *Catal. Sci. Technol.* **3,** 3103–3110 (2013).

[95] Meldrum, F. C., Wade, V. J., Nimmo, D. L., Heywood, B. R. & Mann, S. Synthesis of inorganic nanophase materials in supramolecular protein cages. *Nature* **349,** 684–687 (1991).

[96] Douglas, T. & Stark, V. T. Nanophase Cobalt Oxyhydroxide Mineral Synthesized within the Protein Cage of Ferritin. *Inorg. Chem.* **39,** 1828–1830 (2000).

[97] Klem, M. T., Mosolf, J., Young, M. & Douglas, T. Photochemical Mineralization of Europium, Titanium, and Iron Oxyhydroxide Nanoparticles in the Ferritin Protein Cage. *Inorg. Chem.* **47,** 2237–2239 (2008).

[98] Okuda, M., Iwahori, K., Yamashita, I. & Yoshimura, H. Fabrication of nickel and chromium nanoparticles using the protein cage of apoferritin. *Biotechnology and Bioengineering* **84,** 187–194 (2003).

[99] Douglas, T. *et al.* Synthesis and Structure of an Iron (III) Sulfide-Ferritin Bioinorganic Nanocomposite. *Science* **269,** 54–57 (1995).

[100] Yamashita, I., Hayashi, J. & Hara, M. Bio-template Synthesis of Uniform CdSe Nanoparticles Using Cage-shaped Protein, Apoferritin. *Chemistry Letters* **33,** 1158–1159 (2004).

---

[101] Iwahori, K., Yoshizawa, K., Muraoka, M. & Yamashita, I. Fabrication of ZnSe Nanoparticles in the Apoferritin Cavity by Designing a Slow Chemical Reaction System. *Inorg. Chem.* **44,** 6393–6400 (2005).

[102] Hilton, R. J., Zhang, B., Martineau, L. N., Watt, G. D. & Watt, R. K. Anion deposition into ferritin. *Journal of Inorganic Biochemistry* **108,** 8–14 (2012).

[103] Johnson, J. L., Cannon, M., Watt, R. K., Frankel, R. B. & Watt, G. D. Forming the Phosphate Layer in Reconstituted Horse Spleen Ferritin and the Role of Phosphate in Promoting Core Surface Redox Reactions†. *Biochemistry* **38,** 6706–6713 (1999).

[104] Cheng, Y. G. & Chasteen, N. D. Role of phosphate in initial iron deposition in apoferritin. *Biochemistry* **30,** 2947–2953 (1991).

[105] Hilton, R., David Andros, N. & Watt, R. The ferroxidase center is essential for ferritin iron loading in the presence of phosphate and minimizes side reactions that form Fe(III)-phosphate colloids. *Biometals* **25,** 259–273 (2012).

[106] Hilton, Robert J. Ferritin Diversity: Mechanistic Studies, Disease Implications, and Materials Chemistry. (Brigham Young University, 2011).

[107] Watt, R. K., Hilton, R. J. & Graff, D. M. Oxido-reduction is not the only mechanism allowing ions to traverse the ferritin protein shell. *Biochimica et Biophysica Acta (BBA) - General Subjects* **1800,** 745–759 (2010).

[108] Polanams, J., Ray, A. D. & Watt, R. K. Nanophase Iron Phosphate, Iron Arsenate, Iron Vanadate, and Iron Molybdate Minerals Synthesized within the Protein Cage of Ferritin. *Inorg. Chem.* **44,** 3203–3209 (2005).

[109] Nikandrov, V. V., Grätzel, C. K., Moser, J.-E. & Grätzel, M. Light induced redox reactions involving mammalian ferritin as photocatalyst. *Journal of Photochemistry and Photobiology B: Biology* **41,** 83–89 (1997).

[110] Keyes, J., Hilton, R., Farrer, J. & Watt, R. Ferritin as a photocatalyst and scaffold for gold nanoparticle synthesis. *J Nanopart Res* **13,** 2563–2575 (2011).

[111] Petrucci, O. D., Buck, D. C., Farrer, J. K. & Watt, R. K. A ferritin mediated photochemical method to synthesize biocompatible catalytically active gold nanoparticles: size control synthesis for small ([similar]2 nm), medium ([similar]7 nm) or large ([similar]17 nm) nanoparticles. *RSC Adv.* **4,** 3472–3481 (2014).

[112] Ensign, D., Young, M. & Douglas, T. Photocatalytic Synthesis of Copper Colloids from Cu(II) by the Ferrihydrite Core of Ferritin. *Inorg. Chem.* **43,** 3441–3446 (2004).

[113] Oscar D. Petrucci. Ferritin-Based Photo-Oxidation of Biomass for Nanoparticle Synthesis, Bioremediation, and Hydrogen Evolution. (Brigham Young University, 2013).

---

[114] Kim, I., Hosein, H.-A., Strongin, D. R. & Douglas, T. Photochemical Reactivity of Ferritin for Cr(VI) Reduction. *Chem. Mater.* **14,** 4874–4879 (2002).

[115] V. V. Nikandrov, C. K. Gratzel, J. E. Moser and M. Gratzel, Light induced redox reactions involving mammalian ferfitin as photocatalyst*. J. Photochem. Photobiol.,* B, 1997. **41**, 83–89.

[116] Cherepy, N. J., Liston, D. B., Lovejoy, J. A., Deng, H. & Zhang, J. Z. Ultrafast Studies of Photoexcited Electron Dynamics in γ- and α-Fe2O3 Semiconductor Nanoparticles. *J. Phys. Chem. B* 1998. **102**, 770–776.

[117] Available at http://en.wikipedia.org/wiki/Dye-sensitized_solar_cell

[118] Zumdahl, Steven S. *Chemistry*. (Houghton Mifflin Company, 2007).

[119] Sodium Metal - Molecular Orbital Theory. at <http://wps.prenhall.com/wps/media/objects/4680/4793217/ch21_04.htm>

[120] Chou, C.-C. *et al.* Ruthenium(II) Sensitizers with Heteroleptic Tridentate Chelates for Dye-Sensitized Solar Cells. *Angewandte Chemie International Edition* **50,** 2054–2058 (2011).

[121] Chen, C.-Y., Wu, S.-J., Wu, C.-G., Chen, J.-G. & Ho, K.-C. A Ruthenium Complex with Superhigh Light-Harvesting Capacity for Dye-Sensitized Solar Cells. *Angewandte Chemie* **118,** 5954–5957 (2006).

[122] Mayo, E. I. *et al.* Cyclometalated iridium(iii)-sensitized titanium dioxide solar cells. *Photochem. Photobiol. Sci.* **5,** 871–873 (2006).

[123] Baranoff, E. *et al.* Cyclometallated Iridium Complexes as Sensitizers for Dye-Sensitized Solar Cells. *Chemistry – An Asian Journal* **5,** 496–499 (2010).

[124] Fthenakis, V. M. End-of-life management and recycling of PV modules. *Energy Policy* **28,** 1051–1058 (2000).

[125] Karl W. Böer. Cadmium sulfide enhances solar cell efficiency. *Energy Conversion and Management* **52,** 426–430 (2011).

[126] Kim, I., Hosein, H.-A., Strongin, D. R. & Douglas, T. Photochemical Reactivity of Ferritin for Cr(VI) Reduction. *Chem. Mater.* **14,** 4874–4879 (2002).

[127] Rakshit, T. & Mukhopadhyay, R. Tuning Band gap of Holoferritin by Metal Core Reconstitution with Cu, Co, and Mn. *Langmuir* **27,** 9681–9686 (2011).

[128] Binnig, G., Rohrer, H., Gerber, C. & Weibel, E. Surface Studies by Scanning Tunneling Microscopy. *Phys. Rev. Lett.* **49,** 57–61 (1982).

[129] McMullan, D. Scanning electron microscopy 1928–1965. *Scanning* **17,** 175–185 (1995).

[130] Feenstra, R. M. Scanning tunneling spectroscopy. *Surface Science* **299–300,** 965–979 (1994).

---

[131] Caldeira, A. O. & Leggett, A. J. Influence of Dissipation on Quantum Tunneling in Macroscopic Systems. *Phys. Rev. Lett.* **46,** 211–214 (1981).

[132] Gatteschi, D. & Sessoli, R. Quantum Tunneling of Magnetization and Related Phenomena in Molecular Materials. *Angewandte Chemie International Edition* **42,** 268–297 (2003).

[133] Zumdahl, Steven S. *Chemistry*. pp. 483 (Houghton Mifflin Company, 2007).

[134] Colton, J., Erickson, S., Smith, T. & Watt, R. Sensitive detection of surface- and size-dependent direct and indirect band gap transitions in ferritin. *Nanotechnology* **25,** 135703 (2014).

[135] Smith, T. J. *et al.* Tuning the band gap of ferritin nanoparticles by co-depositing iron with halides or oxo-anions. *J. Mater. Chem. A* (2014). doi:10.1039/C4TA04588B

Chapter 2 – Methods

This chapter contains all of the major synthesis schemes, reactions, and explanations to how and why my experiments were performed. Please note that portions of this chapter will be in "italics," which contain suggestions and notes to the various methods and procedures, including pitfalls to avoid and techniques to obtain better and more consistent results.

Instrumentation

Ferritin materials are characterized through five main techniques which include: column chromatography, UV-Vis spectrophotometry, inductively coupled plasma – mass spectrometry, tunneling electron microscopy, and electrochemical techniques, which include coulometry and cyclic voltammetry.

Column Chromatography

Column chromatography is an important technique for separating different compounds and chemicals from one another. The sample is dissolved into a mobile liquid or gas phase and passed over an immobile stationary phase. The two phases are chosen such that the sample distributes itself between the mobile and stationary phase to a varying degree. In the case of ferritin, a size exclusion column is the preferred method for separating the protein with its sequestered mineral from the unbound ions in solution.

Size exclusion columns separate molecules based on their size or molecular weight. This technique works well for ferritin sample (450 kDa), especially when trying to separate small molecules from ferritin, such as buffers, salts, and unreacted metal ions. Size exclusion chromatography uses porous beads to separate large molecules from smaller ones. Large molecules are unable to enter into the interior of the porous beads and simply pass across the surface of the packing material. Smaller molecules, such as salts or metal ions, enter into the porous bead’s interior, and have a longer path length to pass through the packing material compared to the large molecules. This difference in path length allows the large molecules (ferritin) to pass through the column relatively quickly, whereas the smaller molecules (salts and metal ions) must take a longer path through the column and elute later in the separation process.

UV-Vis Spectrophotometry

The absorption of light can be considered a two-step process. The first step involves the absorption of UV or visible light which causes an excitation of an electron, followed by a relaxation step where the excitons loses adsorbed energy, generally in the form of heat. The specific energies or wavelengths at which the absorption occurs are specific to the types of bonds in the molecule being studied.

Tyrosine and tryptophan residues common in biological compounds will show an intense absorption peak at 280 nm. This absorption originates from the cyclic pi system in the organic molecule, where transitions from $\pi \rightarrow \pi^*$ occur. Apoferritin is easily measured at 280 nm, with an absorption coefficient of 471,000 cm^{-1} M^{-1} (i.e. 0.98 g/L/cm).[1] However, ferritins that contain metal oxide cores cannot be quantified using the 280 nm absorption peak.

Inorganic compounds more commonly have broad absorption bands in the visible region, especially in the first two transition series. Absorption involves electronic transitions between the occupied t_{2g} and unoccupied e_g orbitals originating from the d-atomic orbitals. The energy between the d-orbitals is dependent on the Z-effective of the atom, the oxidation state, and the ligand bound to the metal. Commonly for ferritin, a broad shoulder is observed between 280 nm and 450 nm for the various metal oxide nanoparticles, however distinct colors are observed between each metal. Iron oxides tend to be a brown-orange color, manganese oxides are generally brown-green, and cobalt oxides have a green hue. Titanium oxide cores in ferritin do not produce colors as they are fully oxidized and therefore have no electrons in which to cause a visible excitation between the t_{2g} and e_g orbitals.

UV-Vis spectrophotometry is also used to measure surface plasmon resonance signals, including those from gold nanoparticles. Gold nanoparticles, which can be grown by using metal oxides in ferritin as a photocatalyst, have direct application to immunoassays[2,3], biosensors[4,5], medical treatment[6,7], lab-on-a-chip sensors[8,9], and as scaffolds for other materials[10,11]. When gold nanoparticles grow larger than 2 nm, a surface plasmon resonance (SPR) is observed.[12] The SPR signal originates from the interaction between the electrons of the atom and light. The resonance between the incident light and the natural frequency of the electrons in the atoms causes the reflected light to be of a different color than the incident light. In the case of gold, the SPR signal is 530 nm (green) which gives a deep red to purple color for 10 nm particles in water. As the nanoparticles become larger, a red shift is observed in the SPR signal. Additional changes in the SPR signal can be caused by ligands or other materials binding or interacting to the gold surface, which distort the resonance frequency of the gold's electron surface. The ability for ligands or other materials to alter an SPR signal of gold is a key principle for biosensors and lab-on-a-chip sensors, and ferritin provides a unique scaffold for creating uniform and size controlled gold nanoparticles. The gold nanoparticles are grown on the exterior of ferritin as a result of the ferrihydrite mineral's photo-catalytic activity.

Inductively Coupled Plasma Mass Spectrometry

Plasmas are an electrically conducting gaseous mixture containing a significant concentration of cations and electrons. In the case of inductively coupled plasma (ICP), argon is used as the conducting gas which is brought to an ignition temperature through ohmic heating by a radio-frequency induction coil, and the argon plasma becomes self-sustaining at 10,000 K. This high heat and electron rich environment atomizes the molecules in the sample.

The ionized sample can then be detected in one of two techniques. The first technique is through Optical Emission Spectroscopy (OES). Similarly to how a UV-Vis spectrophotometer operates, the ICP-OES detects the quantity of specific wavelengths of light that is emitted from the elements. The second technique uses Mass Spectrometry (MS), where ions of the elements are passed through a series of quadrupole mass filters and into a detector. ICP-MS can detect far lower concentrations of materials than ICP-OES (1 ppb vs 1 ppm, respectively), but ICP-MS is also more sensitive to matrix effects such as reactions with argon and oxygen (ArO$^+$, FW 55.947) which gives false iron signals (Fe$^+$, MW 55.845). *This particular reaction between argon and oxygen prevents accurate measurements of iron, and therefore the bipyridal assay is the preferred method for iron analysis.*

Tunneling Electron Microscopy

The TEM works by passing a beam of high energy electrons through an extremely thin sample. As the electrons travel and interact with the sample, diffraction, tunneling, and other interactions occur, which generates an image or reciprocal lattice onto a CCD detector. TEMs are able to generate images with significantly higher resolution then light microscopes; this is from the de Broglie wavelength of electrons *(which for the Tecnai TF-20 is about 2.51 pm when accounting for the velocity of the electron)*.

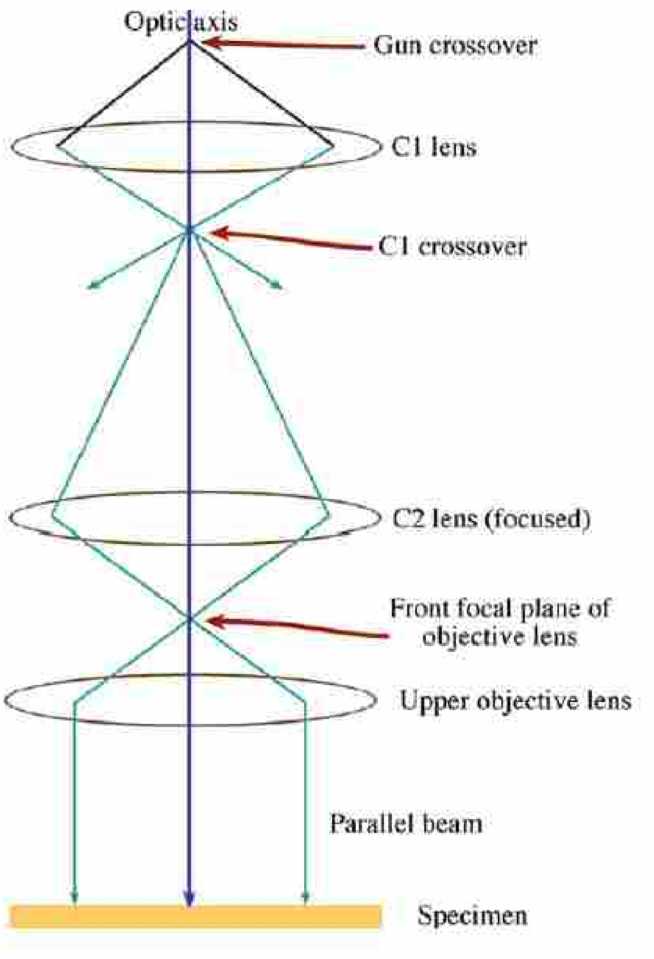

Figure 2 - 1. Upper section of TEM Microscope with exaggerated beam path angles

Using electrons as a 'light source' from TEM imaging leads to unique focusing and imaging properties. As the electron beam moves down the column, electrons are focused and collimated using several magnetic lenses (See Figure 2-1[13]). These lenses are notorious for their hysteresis effects in imaging, which causes the image to move during the image capturing process. The electrons then pass through the ultra-thin sample and interact with both the positively charged nucleus and negatively charged electron cloud. These interactions are used to produce an image or reciprocal lattice. After the electron beam passes through the sample, the beam is the reshaped *(collimated)* and magnified several times until the appropriate magnification has been reached.

The electron-sample interaction gives the TEM a diverse range of sample characterization capabilities. Forward scattered electrons can generate images, provide crystal data, as well as elemental information. Back scattering electrons can generate visible light, secondary electrons, and characteristic X-rays unique to each sample, which can be used for elemental analysis. Elemental information is obtained through collecting back scattered secondary electrons whose energy is specific to the elements in the sample and detected through the X-ray Energy-Dispersive Spectrometry.

In the case of ferritin as well as other nano-crystals, the nano-particles are easily imaged, but are too small to obtain clear structural data from electron diffraction. Diffuse diffraction rings are visible in some cases when the density of ferritin is fairly high across the TEM grid.

Electrochemistry Techniques

Electroanalytical methods have certain advantages over other characterization techniques. Electrochemically measurements are often selective for a particular oxidation state, whereas other methods are not. These techniques also provide information about activities, rather than concentrations.[14]

A DC electrochemical cell consists of two electrical conductors (*electrodes*), a conductive salt solution, and a reference electrode. The working electrode is an electroactive material that is electrochemically inert (does not reduce of oxidize) under the given range of potentials used for a particular experiment. These materials include gold, platinum, and glassy carbon. The counter electrode is simply a conductive wire that is also electrochemically inert under the given conditions. The reference electrode that I use in my research is a $Ag^+/AgCl$ wire in saturated potassium chloride. This electrode has an offset potential of 0.199 V vs. the natural hydrogen electrode, a standard reference in electrochemistry. *It should be noted that the reference electrode is not necessary in all electrochemical techniques, but is required for the techniques that are used herein.*

Cyclic Voltammetry

CV is used to measure the reduction and oxidation (redox) potentials as well as diffusion coefficients for a given chemical. By scanning a voltage range in a forward and reverse direction, the oxidation and reduction potential are observed as a change in current. The peak height is a function of the concentration of the analyte at the working electrode surface. Over multiple scans, the height of the redox peaks decrease due to a depletion of analyte at the electrode surface. This change in peak height as a function of scan rate will give the diffusion coefficient of the analyte in solution.

Coulometry

There are three electroanalytical methods that are based on the oxidation and reduction of an analyte, and are constant-potential coulometry, constant-current coulometry, and electrogravimetry. In my research I use constant-potential coulometry, where a fixed potential is used to measure the total number of electrons passed between the working and counter electrode.

Apoferritin Preparation and Quantification

Apoferritin preparation

A dialysis procedure is used to remove the iron mineral from ferritin, creating apoferritin. Dialysis originates from the Greek word, *dialusis,* meaning dissolution. It is a diffusion process where solutes pass through a semipermeable membrane, flowing from high concentration to low concentration.

Apoferritin was prepared using established methods from M. Joo et al[15] and J. Polanams et al.[16] native horse spleen ferritin (HoSF) was purchased from Sigma Aldrich and stored at 4 °C. A Millipore Dialysis Cassette (MW cut off <100 kDa) is then placed into the dialysis solution of 0.25 M sodium acetate trihydrate (34.02 g/L) with 1% thioglycolic acid (7.54 mL of 70% thioglycolic acid/L) for 15 minutes to hydrate. The resulting pH should be between 4.8 and 5.0, adjustments may be necessary. The HoSF is then added directly to dialysis cassette using an injection syringe, being careful to not pierce the dialysis membrane, and placed into the refrigerated dialysis solution with gentle stirring for the remainder of the dialysis. *(Please note that dialysis tubing may also be used, however dialysis tubing will lose approximately 30% to 60% of your total initial protein through defects the membrane, whereas the dialysis cassettes only loose about 10% to 20% of the total initial protein added. Additionally, the dialysis cassette dilutes the protein far less than dialysis tubing.)* If done properly, the dialysis solution should turn purple at first from the Fe^{3+}-thiolate, and may go clear after a few hours. The solution needs to be exchanged every 8 hours for 24 hours.

After the thioglycolic acid exchanges, the dialysis cassette with the now apoferritin inside is dialyzed against a 0.5% sodium bicarbonate solution, with an exchange every 8 hours for 24 hours. Bipyridine may be added in the first exchange with some sodium hydrosulfide to chelate any remaining iron, including the iron that is bound to the ferroxidase center. *If the protein precipitates during the thioglycolic acid step, immediately exchange the ferritin containing cassette into the bicarbonate buffer solution to re-nature the protein. This may result in additional protein loss. After the protein is re-natured, it may be placed into the thioglycolic acid to continue the iron chelation.*

The apoferritin cassette is then placed into Mili-Q (15 M Ω) water for 8 hours, and then placed into a solution of desired buffer. In most cases for my experiments, I used a salt free 0.01% bicarbonate buffer to maintain a neutral pH, while allowing freedom in placing apoferritin into various salts for experimentation.

Protein Analysis - Lowry Method

A Lowry Assay[17] is the preferred method for measuring ferritin protein concentration. The Lowry Assay will have fewer matrix effects which would otherwise give inaccurate protein concentrations. Other methods may be used, including the Bradford method, which is discussed later. The Lowry method that is used in my research can be found in the reference by Peterson et al.[18]

The Lowry Assay combines the reduction of copper (II) with the oxidation of tryptophan and tyrosine residues in basic conditions. Copper (I) is produced upon oxidation of tryptophan and tyrosine residues, and the reducing electron is transferred to the Folin-Ciocalteu reagent (or Folin reagent for convenience). While the exact mechanism of how the copper and Folin reagent react with one another, the Folin reagent does change from a pale yellow to an intense blue when reduced, depending on the protein concentration. This blue color is measured at 750 nm. This assay works best using between 2 and 20 µg of protein.

There are two reagents used in this process, Reagents A and B.

Reagent A: Reagent A is made by mixing 1 part CTC, with 1 part NaOH (0.8 N), 1 part 10% wt/wt sodium dodecyl sulfate, and 5 parts Mili-Q water. 0.8 mL per sample and standard is required. This is made fresh for each day a Lowry analysis is performed.

A CTC solution (stable for 2 months) is made by adding 50g of Na_2CO_3 into about 200 mL of Mili-Q water. In a separate 200 mL, 0.5g of $CuSO_4$ is dissolved followed by 1.0g of sodium tartrate. The Na_2CO_3 solution is then slowly added into the $CuSO_4$ solution over the course of about 5 minutes. Fill to 0.5L with Mili-Q water. (*If this is not done properly, the solution will precipitate. Please check the solution carefully before use, while it is generally stable for 2 months, it may precipitate in less than a week if not stored in a cabinet. Check for small crystals or precipitates by shaking vigorously. If present, a new solution must be made.)*

Reagent B: This solution is stable in a dark amber bottle for 12 months. Mix 1 part Folin Reagent with 5 parts Mili-Q water to make Reagent B. 0.2 mL per tube is required.

For preforming the protein analysis, add 1.00 mg/mL Bovine Serum Albumin (BSA) standard in the amounts of 0, 10, 20, 30, 40, and 50 µL into test tubes. Fill to 100 µL with Mili-Q water. Samples are made by adding 2-20 µg of total protein to each tube. (*Generally, HoSF purchased from Sigma Aldrich will have a protein concentration of about 50 mg/mL. The protein* *analysis will use between 0.5 and 3 µL of the native ferritin solution. Apoferritin, after it is made, will need between 2 and 10 µL of solution for protein analysis. Also, be sure to "rinse" the pipette by drawing and releasing the solution several times into the cuvette as this will equalize the solution's protein concentration with the pipette tip's protein concentration.)* Run each sample in sextuplet, or 2 sets of 3 different protein concentrations. (*For example, when measuring the concentrations of HoSF, I use two sets of 0.5 µL, two sets of 1 µL, and two sets of 3 µL HoSF solutions).* Every sample is now treated identically. Add 800 µL Reagent A to each tube, shake by hand within 3 seconds of addition, and wait 10 minutes. Then add 200 µL of Reagent B, vortex quickly (within 3 seconds), and then wait for 30 minutes. Read absorbance at 750 nm. The color is stable for two hours. Then use Excel or the software package included in the instrument to determine protein concentration.

If using a 96 flat bottom well plate, add 200 µL of the finished assay to each well, taking special care to not lose the sample position and removing any bubbles that may form. Analyze at 750 nm on a well plate reader. Protein concentration may be determined by using Excel or by using the software package included with the well plate reading instrument.

(HoSF concentrations from Sigma-Aldrich are generally between 30 and 55 mg/mL with iron counts around 1500 ± 300 Fe/HoSF (discussed later). Using the dialysis cassettes should yield a protein concentration between 10 and 25 mg/mL Apoferritin if done properly. In creating metal oxide cores, I try to target 2-5 mg/mL protein concentration for metal loading, which generally gives about 1-2 mg/mL protein concentration after samples have passed through a size-exclusion (Sephadex G-25 or G-75) column (discussed later).)

Protein Analysis- Bradford Method

The Bradford Protein Analysis is a much faster method to measure protein concentration than the Lowry Method, taking only a few minutes for the reaction to complete. However, the Bradford protein analysis will underestimate the protein concentration of ferritin, which will cause an overestimation of the metal content inside ferritin. It is also more susceptible to matrix affects caused by detergents and buffer, and this assay has a smaller linear range than the Lowry Method.

The technique works in a two-step process. The Coomassie reagent (initially red or brown) donates a free electron to the ionizable amino acids of the protein (arginine, lysine, and histidine) which denatures the tertiary structure. The oxidized Coomassie reagent then binds to the non-polar regions of the exposed amino acids, and is further strengthened by the ionic interaction between the Coomassie reagent and the exposed amino acid. The stabilized Coomassie reagent forms the blue Coomassie dye.

Sample preparation is the same as the lowery method, with a standard curve between 0 and 50 μg/mL BSA. Then, all standard and samples are diluted up to 100 μL. Then 1.5 mL of Coomassie Brilliant Blue (G-250) is added to each sample. The blue color is measured at 595 nm.

Synthesis of Metal Oxides in Ferritin

Reconstituted Iron Synthesis

Iron loading into ferritin is accomplished by reacting apoferritin with ferrous ammonium sulfate. The reaction proceeds as follows:

$$(1)\ 2\mathrm{Fe}^{\mathrm{II}} + 2\mathrm{H_2O} + \mathrm{O_2} + \mathrm{FTN} \rightarrow 2\mathrm{Fe}^{\mathrm{III}}\mathrm{(O)OH\text{-}FTN} + 2\mathrm{H}^{+}$$

5 mg of apoferritin is added to a buffer solution between pH 5.4 and pH 9.4 and is gently stirred. 100 mM ferrous ammonium sulfate in 10 mM nitric acid is then added over the course of 3 hours, with 10 μL additions every 10 minutes. A solution of 330 mM NaOH is added between each iron addition to neutralize the acid produced during the iron loading. The pH should be monitored throughout the reaction with a calibrated pH electrode.

This procedure allows for 100 irons per ferritin to be added every 10 minutes. The slower the loading rate per minute, the less protein precipitation is observed, leading to even larger targeted cores. Recently, our lab has demonstrated complete loading of 4500 Fe/FTN by using a syringe pump set to load less than 1 Fe/FTN per minute over the course of many hours while maintaining pH 7.4.

Manganese – Trevor Douglas Method

Mn(O)OH cores were also synthesized by following established methods.[19,20] A solution of $MnCl_2$ was added to a 50 mM AMPSO buffered solution at pH 8.9 with 5 mg of apoferritin to form the manganese cores. A color change was observed from clear-colorless to brown as the manganese oxidized and the core formed. The amount of $MnCl_2$ added was varied between samples to target a range of core sizes at a rate of 100 metal atoms per ferritin per addition every 10 minutes. The pH of the solution was also maintained by addition of 10 mM NaOH.

Manganese – Trevor Smith Method[21], Chapter 6

5 mg of apoferritin was added to one of three buffered solutions containing either: 1 M pH 5.4 MES buffer, 1 M pH 7.4 Imidazole buffer, or 1 M pH 9.4 AMPSO buffer. Each buffered apoferritin solution was then used in one of the following loading reactions.

Comproportionation loading was achieved by co-additions of first 100 permanganate/FTN (10 uL of 88 mM $KMnO_4$) followed quickly (*within 3 seconds, or before the* *permanganate changed colors*) by an addition of 100 Mn(II)/FTN (10 uL of 143 mM $MnCl_2$) to 5 mg of apoferritin. These additions were repeated 8 times, with at least 10 minutes between each addition to target a core size of 1600 Mn/FTN. Various ratios of Mn(II):MnO_4^- were also tested to see if Mn(IV) cores could be created.

Control reactions were performed by adding 200 μL of 88 mM potassium permanganate to 5 mg of aforementioned apoferritin solution using a syringe pump. The solution was added at a rate of 10 μL per hour, or 80 Mn/FTN per hour, targeting 1600 Mn/FTN. Samples were then centrifuged and decanted into a Sephadex G-75 size exclusion column, which was buffered with 25 mM pH 7.4 imidazole, no salt.

Cobalt Synthesis

Co(O)OH cores were synthesized by following established methods[22] where $Co(NO_3)_2$ and H_2O_2 were periodically added to 5 mg of apoferritin solution. The amount added was adjusted to target a range of core sizes at a rate of 100 metal atoms per ferritin per addition every 10 minutes. The pH of the solution was maintained by addition of 10 mM NaOH.

Titanium Synthesis

Titanium^{III}-citrate was made using stoichiometric ratios of Titanium^{III} chloride and citrate (1:3 ratio, respectively). When mixed into solution, a purple color is observed. Oxygen (or atmosphere) is bubbled through solution until the solution turns clear-colorless. *Please note that Ti(III) is a highly active reducing agent, and can/will combust when oxygen is present. As such, it is stored in the glove box, and must remain in said glove box. Handle this material with extreme caution and only open in the glove box. Once the Ti(III) is in solution, it can be safely handled in air.*

Ti(O)OH cores were made using the method from Klem et al.[23] Ti^{III}-citrate, ferritin, and buffer solutions were made to contain three times the concentration as found in the established method to give better amounts of absorption for the band gap measurements *(I used 5 mg/mL apoferritin, and targeted 2000 Ti/FTN)*. A 150 W Xe arc lamp was used to illuminate the samples for titanium deposition, with a 1 cm water path to absorb IR light. Sample temperature was maintained at 20 °C using a circulating temperature bath. Illumination lasted for roughly 20 minutes.

Sample Characterization

Ferritin samples are characterized using the five previously mentioned techniques, which were: column chromatography, UV-Vis spectrophotometry, inductively coupled plasma – mass spectrometry, tunneling electron microscopy, and electrochemical techniques, which include coulometry and cyclic voltammetry.

Column Chromatography

Before analyzing the metal content of each ferritin sample, all samples were passed over a Sephadex G-75 column with a salt free pH 7.4 imidazole buffer and collected into 1 mL fractions. This process separates the ferritin bound metals from the extraneous ions left over in solution, which were not incorporated into ferritin.

Iron Analysis

Iron content is measured using UV-Vis spectrophotometry by reducing all irons to Fe(II) which then forms a complex with bipyridine. The intense red color from the iron-bipyridine complex originates from the metal to ligand charge transfer (MLCT). *Additionally, this complex can serve as a protecting group for the iron, preventing Fenton Chemistry (peroxide-iron reactions) from occurring.*

Using a 1 mL semi-micro visible cuvette: add 750 µL Mili-Q water, 250 µL saturated bipyridine, and at least 10 mg sodium hydrosulfide. Then blank the solution in the UV-VIS Spectrophotometer. Then add between 1 and 100 µL of the iron containing sample until an absorbance greater than 0.1 abs units is measured. three to five more additions of the same volume were added and the absorbance record. The concentration of iron were calculated using $A=bc\epsilon$, where A is absorbance, b is the path length, c is the molar concentration, and ϵ is the molar absorptivity. The molar absorptivity for the bipyridin iron complex at 522 nm is ϵ_{522} = 8650 M^{-1} cm^{-1}.[24] The irons per ferritin are calculated based on the ratio between the protein concentration and the iron concentration.

Inductively Coupled Plasma – Mass Spectrometry Metal Analysis

A standard curve is created using metal standards purchased from Sigma-Aldrich and trace metal grade 2.5% nitric acid. Standards are generally prepared at 0, 10, 50, 100, and 200 ppb, though this technique can measure up to 1000 ppb.

Samples are prepared using aliquots between 10 and 50 µL of metal containing ferritins, which are added to trace metal grade 2.5% nitric acid, for a final volume of 5 mL and allowed to sit overnight. Heating up to 100 °C may also be done to better denature the protein and solubilize the metal. The solutions are then passed through a 0.2 µM filter which removes any precipitates, including ferritin. The clean samples are then ready for ICP-MS analysis.

Tunneling Electron Microscope Sample Preparation

TEM samples are prepared using 100 mesh amorphous carbon TEM grids. The amorphous carbon is charged using a static electricity generator and a vacuum tube. Grids are placed on a glass slide and placed inside a vacuum tube. The vacuum tube is pumped down with a vacuum pump for 30 seconds, and then the static electricity generator is turned on for 30-60 seconds. The TEM grid is then removed from the apparatus, add 3 μL of Ferritin *(between 0.1 mg/mL and 10 mg/mL)* onto the charged TEM grid for 60 seconds. Wick away the solution with a Kimwipe. Rinse the grid by dipping the ferritin into a drop of MiliQ water for a few seconds and then wick away the moisture using a clean portion of the Kimwipe. Varying the time the ferritin solution has on the grid will change the amount of ferritin deposition onto the amorphous carbon grid. *This is good for imaging the cores and finding good diffraction patterns, the protein shell will not be visible. If an image of the protein shell with the core (or lack thereof) is wanted do the following.* For a negatively stained image add 3 μL of 0.5 to 3.0% uranyl acetate to the grid for 60 seconds. Decreasing the length that uranyl acetate has on the grid will also decrease the amount of negative staining on the grid, increasing the time will increasing the negative stain. Rinse the grid by dipping the ferritin into a drop of MiliQ water for a few seconds and then wick away the moisture using a clean portion of the Kimwipe. *Other acceptable negative stains include ammonium molybdate, uranyl acetate, uranyl formate, phosphotungstic acid, and osmium tetroxide. Also, please note that this process creates a concentration gradient of both protein and negative staining on the grid. If you find that the area that you are imaging is not suitable, move the sample to an extreme portion of the grid to find more appropriate concentrations of protein and negative stain.*

Cyclic Voltammetery

CV was used to measure the redox potentials of the metal oxide mineral inside ferritin. The 1.55 mm^2 gold surface of the working electrode is cleaned using three to five rinses of a piranha solution made fresh for each cleaning. Rinse the electrode in the piranha solution for 1 minute, followed by thorough rinsing with Milli-Q water, and repeat three to five times. Place the cleaned working electrode into a salt solution containing the reference and counter electrode, followed by addition of ferritin. Set the potentiostat to a -800 mV Vs. Ag^+/AgCl for two minutes. This

Piranha solution is very dangerous. It is made by mixing 3 parts concentrated sulfuric acid with 1 part 30% peroxide, which makes a strong oxy-acid. This strong oxidizing acid will turn most carbon containing molecules into carbon dioxide, and hydroxylate most other elements. Never make more than 5 mL at a time. And, only make this in the vent hood, wearing gloves, lab coat, goggles, face shield, and with the vent hood's guard in place.

Coulometry

The method from Watt et al.[25] is used to measure the oxidation state of the manganese mineral inside of ferritin as a function of reduction at a set potential of -800 mV vs sat'd Ag^+/AgCl. An electron mediating solution (methyl viologen, benzoyl viologen, or flavor mono-nucleotide) is reduced prior to ferritin addition. Once a stable baseline current has been reached, a degassed ferritin solution of known protein and metal concentration is added, which raises the current or electron flow into the cell. The electrons from the electron mediating solution are transferred to the mineral core in ferritin and the electron mediating solution is re-reduced. After ten minutes the current should return to baseline. The area under the curve is directly proportional to the number of electrons that were used to reduce the ferritin mineral. The calculated area under the curve from each experiment is then plotted as a sigmoidal plot with percent reduced in the y-axis and potential on the x-axis. The inflection point of the sigmoidal curve is taken to be the redox potential of the ferritin mineral.

Band gap Measurements

Optical measurements were performed using a home built ultraviolet-visible spectrophotometer. A Digikrom 250 spectrometer was used to obtain monochromatic light from an Oriel 66011 xenon arc lamp with a typical bandwidth of 1.6 nm. The monochromatic light was then collimated and passed through a cuvette containing the ferritin sample to a photodiode detector. The light from the arc lamp was modulated with a mechanical chopper at approximately 1.1 kHz; the photodiode signal was then sent to a lock-in amplifier referenced to the chopper and read out by the computer. This standard lock-in technique provides a high-signal to low-noise ratio.

The data was obtained in two steps. First a control sample was placed in the cuvette (solution with no ferritin), and absorption is measured over a range of wavelengths. Then, the same scan was performed with the ferritin sample in solution. The control and the ferritin-based scans were performed in two wavelength ranges, typically 300 nm to 450 nm, and 350 nm to 750 nm. The short wavelength scans were done with a 1200 lines/mm grating blazed at 250 nm; the long wavelength scans with a 1200 lines/mm grating blazed at 500 nm.

For a more detailed explanation of this technique, please see Chapter 3.

References

---

[1] Han, Bong-Gyoon, Ross W. Walton, Amos Song, Peter Hwu, Milton T. Stubbs, Steven M. Yannone, Pablo Arbeláez, Ming Dong, and Robert M. Glaeser. Electron microscopy of biotinylated protein complexes bound to streptavidin monolayer crystals. *Journal of Structural Biology* **180,** 249–253 (2012).

[2] Gupta, S., Huda, S., Kilpatrick, P. K. & Velev, O. D. Characterization and Optimization of Gold Nanoparticle-Based Silver-Enhanced Immunoassays. *Anal. Chem.* **79,** 3810–3820 (2007).

[3] Hirsch, L. R., Jackson, J. B., Lee, A., Halas, N. J. & West, J. L. A Whole Blood Immunoassay Using Gold Nanoshells. *Anal. Chem.* **75,** 2377–2381 (2003).

---

[4] Pingarrón, J. M., Yáñez-Sedeño, P. & González-Cortés, A. Gold nanoparticle-based electrochemical biosensors. *Electrochimica Acta* **53,** 5848–5866 (2008).

[5] Medley, Colin D., Joshua E. Smith, Zhiwen Tang, Yanrong Wu, Suwussa Bamrungsap, and Weihong Tan. Gold Nanoparticle-Based Colorimetric Assay for the Direct Detection of Cancerous Cells. *Anal. Chem.* **80,** 1067–1072 (2008).

[6] Kennedy, Laura C., Lissett R. Bickford, Nastassja A. Lewinski, Andrew J. Coughlin, Ying Hu, Emily S. Day, Jennifer L. West, and Rebekah A. Drezek. A New Era for Cancer Treatment: Gold-Nanoparticle-Mediated Thermal Therapies. *Small* **7,** 169–183 (2011).

[7] Cheng, Yu, Anna C. Samia, Joseph D. Meyers, Irene Panagopoulos, Baowei Fei, and Clemens Burda. Highly Efficient Drug Delivery with Gold Nanoparticle Vectors for in Vivo Photodynamic Therapy of Cancer. *J. Am. Chem. Soc.* **130,** 10643–10647 (2008).

[8] Hosokawa, K., Sato, K., Ichikawa, N. & Maeda, M. Power-free poly(dimethylsiloxane) microfluidic devices for gold nanoparticle-based DNA analysis. *Lab Chip* **4,** 181–185 (2004).

[9] Figeys, D. & Pinto, D. Lab-on-a-Chip: A Revolution in Biological and Medical Sciences. *Anal. Chem.* **72,** 330 A–335 A (2000).

[10] Fullam, S., Cottell, D., Rensmo, H. & Fitzmaurice, D. Carbon Nanotube Templated Self-Assembly and Thermal Processing of Gold Nanowires. *Advanced Materials* **12,** 1430–1432 (2000).

[11] Cui, Rongjing, Chang Liu, Jianming Shen, Di Gao, Jun-Jie Zhu, and Hong-Yuan Chen. Gold Nanoparticle–Colloidal Carbon Nanosphere Hybrid Material: Preparation, Characterization, and Application for an Amplified Electrochemical Immunoassay. *Advanced Functional Materials* **18,** 2197–2204 (2008).

[12] Eustis, S. & El-Sayed, M. A. Why gold nanoparticles are more precious than pretty gold: Noble metal surface plasmon resonance and its enhancement of the radiative and nonradiative properties of nanocrystals of different shapes. *Chem. Soc. Rev.* **35,** 209–217 (2006).

[13] David B. Williams & C. Barry Carter. *Transmission Electron Micropscopy - A Textbook of Materials Science*. **1,** *pp 142,* (Springer).

[14] B. Floyd Brown *et al. Corrosion and Metal Artifacts - A Dualogue Between Conservators and Achaeologists and Corrosion Scientists*. (1977).

[15] Joo, M.-S., Tourillon, G., Sayers, D. E. & Theil, E. C. Rapid reduction of iron in horse spleen ferritin by thioglycolic acid measured by dispersive X-ray absorption spectroscopy. *Biology of metals* **3,** 171–175 (1990).

[16] Polanams, J., Ray, A. D. & Watt, R. K. Nanophase Iron Phosphate, Iron Arsenate, Iron Vanadate, and Iron Molybdate Minerals Synthesized within the Protein Cage of Ferritin. *Inorg. Chem.* **44,** 3203–3209 (2005).

---

[17] Lowry, O. H., Rosebrough, N. J., Farr, A. L. & Randall, R. J. Protein measurement with the Folin phenol reagent. *J biol Chem* **193,** 265–275 (1951).

[18] Peterson, G. L. A simplification of the protein assay method of Lowry et al. which is more generally applicable. *Analytical Biochemistry* **83,** 346–356 (1977).

[19] Meldrum, F. C., Wade, V. J., Nimmo, D. L., Heywood, B. R. & Mann, S. Synthesis of inorganic nanophase materials in supramolecular protein cages. *Nature* **349,** 684–687 (1991).

[20] Mackle, P., Charnock, J. M., Garner, C. D., Meldrum, F. C. & Mann, S. Characterization of the manganese core of reconstituted ferritin by x-ray absorption spectroscopy. *J. Am. Chem. Soc.* **115,** 8471–8472 (1993).

[21] Smith, Trevor J., Stephen D. Erickson, Catalina Matias Orozco, Andrew Fluckiger, Lance M. Moses, John S. Colton, and Richard K. Watt. Tuning the band gap of ferritin nanoparticles by co-depositing iron with halides or oxo-anions. *J. Mater. Chem. A* **2,** 20782–20788 (2014).

[22] Douglas, T. & Stark, V. T. Nanophase Cobalt Oxyhydroxide Mineral Synthesized within the Protein Cage of Ferritin. *Inorg. Chem.* **39,** 1828–1830 (2000).

[23] Klem, M. T., Mosolf, J., Young, M. & Douglas, T. Photochemical Mineralization of Europium, Titanium, and Iron Oxyhydroxide Nanoparticles in the Ferritin Protein Cage. *Inorg. Chem.* **47,** 2237–2239 (2008).

[24] Moss, M. L. & Mellon, M. G. Colorimetric Determination of Iron with 2,2'-Bipyridyl and with 2,2',2'-Terpyridyl. *Ind. Eng. Chem. Anal. Ed.* **14,** 862–865 (1942).

[25] Watt, G. D., Frankel, R. B. & Papaefthymiou, G. C. Reduction of mammalian ferritin. *Proceedings of the National Academy of Sciences* **82,** 3640–3643 (1985).

Chapter 3 – Sensitive Detection of Surface- and Size-Dependent Direct and Indirect Band gap Transitions in Ferritin

I am including this chapter as a summary of a published paper that I co-authored, as it sets the foundation for the rest of the dissertation. The full paper is available at Nanotechnology, volume 25, pp. 135703 (2014), and is titled "Sensitive Detection of Surface- and Size-Dependent Direct and Indirect Band Gap Transitions in Ferritin."

In this paper, I conducted the majority of the sample preparation and characterization. Stephen Erickson preformed the band gap measurements in collaboration with Dr. John Colton who wrote the majority of the paper, including the explanation of the physics. I also assisted and took part in the writing process.

Overview

The interplay between minimizing energy loss from photons of excess energy, while maximizing the number of photons that can be absorbed led Shockley and Queisser to calculate the most efficient single band gap of our solar irradiance.[1] They found that single material with a band gap of 1.34 eV would reach a maximal 33.7% photon to electron conversion efficiency. Silicon, which has a band gap of 1.1 eV would reach a maximal 29% efficiency. The 1.1 eV band gap allows for light above 1.1 eV (1127 nm) to be harvested for photon to electron conversion. However, excess light energy above the band gap is rapidly lost as heat or phonon energy, and light with energy less than that of the band gap goes unabsorbed. The loss of excess photon energy is what lowers the maximum photon to electron conversion efficiency

In order to design a solar cell, the knowledge and understanding of both the type of band gap or semiconductor material as well as the energy of the band gap are required. There are two types of band gaps, namely direct and indirect band gaps. A direct band gap requires only a photon of sufficient energy to allow for an electron in the valence band to be excited into the conduction band. An indirect band gap requires both a photon of sufficient energy as well as a phonon of sufficient momentum to allow for an electron to move between the valence band and the conduction band minimum.

Silicon solar cells are also considered to be first generation photovoltaic devices. These first generation photovoltaics are cost prohibitive due to the amount of material required to allow for sufficient absorption. Second generation photovoltaics use thin film technology to lower the cost of materials and can be purely inorganic materials, or use both organic/inorganic hybrids. Third generation photovoltaics use nanoparticle technology to both lower the cost of materials while increasing the range of band gaps available for a single material by exploiting quantum confinement effects, where a nanoparticle's band gap depends on the size of the nanoparticle. These third generation photovoltaics often use inorganic light harvesting centers with organic ligands to promote electron harvesting. It has been suggested that proteins may also act as organic ligands, which could both stabilize the inorganic material as well as assist in electron harvesting.[2] Ferritin is a good example of an organic/inorganic hybrid material for studying third generation solar cells.

Ferritin is a sphere-like bio-inorganic molecule that measures 12 nm in diameter with an 8 nm hollow interior. This interior is generally filled with a ferrihydrite (Fe(O)OH) mineral. The protein component solubilizes the ferrihydrite mineral in solution and maintains its stability over pH 4-10 and up to 85 °C. Additionally, the protein maintains the oxidation state of the iron in the ferrihydrite mineral.

The ferrihydrite mineral has been previously demonstrated to have photocatalytic properties, where upon illumination the protein is able to reduce Au(III) to Au(0)[3], Cr(VI) to Cr(III)[4], Cu(II) to Cu(0)[5], Ag^+ to Ag(0)[6] and Hg_2(II) to Hg(0)[7]. The band gap energy of the ferrihydrite mineral was estimated using a photochemical colorimetric assay with selective light filters. In those papers[3,4], the photochemical process occurred using light between 2.5-3.5 eV and 3.0-3.5 eV, respectively. These energies correspond to the UV region of the light spectrum between 495 nm to 354 nm and 413 nm to 354 nm, respectively. Whether or not the ferrihydrite mineral in ferritin was a direct or indirect band gap semiconductor was not determined.

Another technique performed by Rakshit et al.[8] used scanning tunneling spectroscopy (STS) to measure the band gaps of both the native ferrihydrite mineral in ferritin as well as the band gaps of other non-native metals in ferritin. These values ranged between 0.00 eV and 1.47

eV for the non-native metals in ferritin, with unreported errors. The ferrihydrite mineral in ferritin was measured to have a band gap of 1.00 eV. It should be noted that the reported experimental results show large deviations in their measurements and that STS experiments in general measure surface states of a material. Measuring a bulk property, such as a band gap, would be difficult to say the least. It is more likely that the STS technique measured the surface states of the ferrihydrite mineral, and not the bulk band gap. Additionally, whether or not the ferrihydrite mineral is a direct or indirect band gap semiconductor was not determined.

In order to design a ferritin based solar cell or photovoltaic system, both the type of band gap as well as the energy of the band gap transition needs to be understood. Optical absorption spectroscopy (OAS) allows for both the determination of the band gap energy as well as investigating whether a given material is a direct or indirect band gap semiconductor. In short, the absorption coefficient "α" is used to calculate both the direct and indirect band gaps of the ferrihydrite mineral in ferritin. In the work done in our group by Colton et al.[9] we detail and explain the physics and calculations used to find the direct and indirect band gaps of the ferrihydrite mineral in ferritin.

Experimental

Three sets of samples were prepared for band gap measurements that include: native ferritin, surface modifications to the native ferrihydrite mineral, and selected core sizes of reconstituted ferrihydrite minerals in ferritin.

Native horse spleen ferritin was purchased from Sigma-Aldrich and the iron content of each ferritin was measured by comparing the iron concentration to the protein concentrations. Iron concentrations were determined using reducing agents with bipyridine.[10] Protein concentrations found by using a modified Lowry method.[11,12] The ratio between the iron and protein concentrations gives the irons per ferritin which was determined to be 1100 Fe/ferritin.

Surface modifications to the native ferrihydrite mineral in ferritin were also performed using native ferritin. Native ferritin was desalted using a Millipore 100 kDa MW cutoff centrifuge filter with a salt free 0.10% bicarbonate buffer solution at pH 7.4. The desalted ferritins were then placed into 200 mM sodium salt solutions that consisted of F^-, I^-, Br^-, Cl^-, and PO_4^{3-}. Additionally, common organic molecules were also tested for their ability to alter the ferrihydrite mineral, and included citrate and cysteine.

Reconstituted ferrihydrite minerals were made in order to test for quantum confinement effects of the ferrihydrite mineral. Apoferritin was created using established dialysis methods.[13] Native ferritin was dialyzed against mercaptoacetic acid using a Millipore 10 kDa dialysis cassette to remove iron from ferritin. The resulting apoferritin was then dialyzed against a 0.10% salt free bicarbonate buffer. The resulting protein concentration was measured using the modified Lowry assay.[12] Once the protein concentration was known, ferrous ammonium sulfate was added to a 50 mM pH 7.4 imidazole and apoferritin solution at a rate no greater than 100 irons per ferritin per 10 minutes, targeting core sizes of 500, 1000, and 1500 irons per ferritin.

After synthesis, the reconstituted ferrihydrite minerals in ferritin were passed over a Sephedex G-25 size exclusion column with a 50 mM pH 7.4 imidazole running buffer to separate ferritin bound iron from the unbound iron atoms in solution. The resulting ferrihydrite ferritin minerals where then analyzed using the previously mention irons per ferritin quantification methods. The resulting cores from the targeted 500, 1000, and 1500 irons per ferritin were 640, 980, and 1200 irons per ferritin.

The band gaps of the ferrihydrite ferritin samples mentioned previously were all measured using optical absorption spectroscopy performed by Stephen Erickson. All samples were diluted to 0.4 mg/mL and 0.1 mg/mL for the indirect and direct band gap measurements.

Results and Discussion

The ferrihydrite mineral in ferritin was determined to be an indirect band gap semiconductor with an indirect band gap of 2.140 ± 0.015 eV which also contains a direct transition at 3.053 ± 0.008 eV and is shown in Figure 3-1. In this figure the absorption coefficient "α" is plotted as a function of energy (eV). The linear extrapolation of the plot gives the band gap energy the material. The band gap energy can be calculated for a direct band gap if using α^2, or the indirect band gap if using $\alpha^{1/2}$. A defect binding energy of 0.220 ± 0.010 eV was also observed and is shown in Figure 1(a) in the left linear portion of the curve which does not

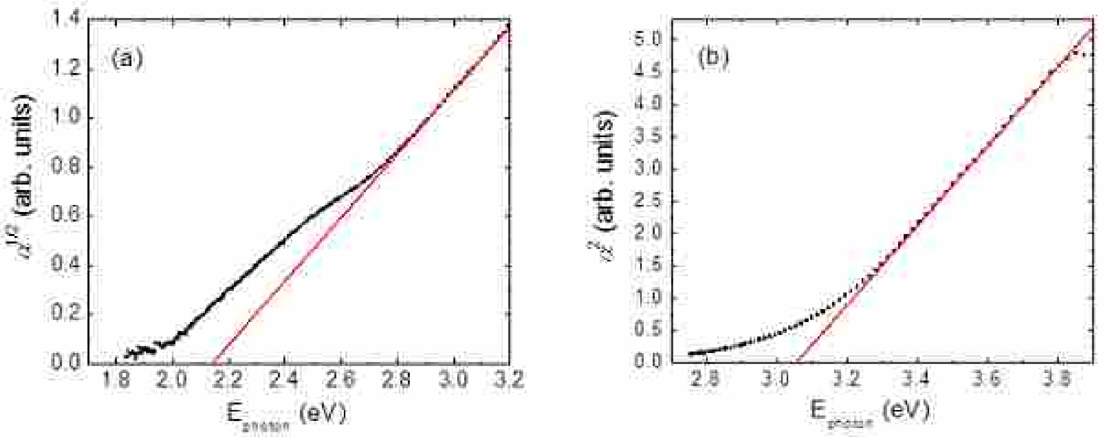

Figure 3 - 1. Representative plots of the absorption of ferrihydrite, measured at 300K. Linear fits are used to obtain band gap energies. (a) Plot of the square root of the absorption coefficient vs. photon energy, displaying two indirect absorption edges related to the indirect transition. (b) Plot of the square of the absorption coefficient vs. photon energy, displaying a third absorption edge, related to the direct transition.

have a linear fit shown. The phonon energy of the indirect band gap could not be determined either due to the phonon energy being too small, or that the thermal occupancy of the phonon component is too large, and is described in detail by our groups' paper by Colton et al.[9]

The resulting band gap measurements lead to the proposed band structure of the ferrihydrite mineral in ferritin as is shown in Figure 3-2.

Figure 3 - 2. Band structure schematic of ferrihydrite in native holoferritin based on the band gaps and defect energy level obtained from the optical absorption measurements.

The agreement between the measured direct transition at 3.05 eV and the optical filter chemical assay experiments by Kim et al.[4] and later Keyes et al.[3]of respectively 2.5-3.5 eV and

3.0-3.5 eV is evident. This is not surprising considering both techniques use optical absorption of the ferrihydrite mineral for band gap determination. Additionally the stark difference between the STS and the OAS techniques is also evident, having measured an undetermined band gap of 1.00 eV[8] and the closest measured indirect band gap of 2.14 eV respectively. As we are measuring the band gaps of the ferrihydrite mineral for the purposes of designing a photovoltaic system, we consider the optical absorption spectroscopy technique to be the most correct measurement of the band gaps in ferrihydrite ferritin, as they also agree closely with the optical filter colorimetric assays which were between 2.5-3.5 eV[3] and 3.0-3.5 eV[4.]

Surface modifications to the ferrihydrite mineral in ferritin resulted in variations to the measured band gap energy. As is shown in Figure 3-3, the sodium halide salts were able to raise the band gap energy of unmodified ferrihydrite minerals following trends in electronegativity. Iodide gave the least significant change and is thought that the large anion size prevents significant deposition into the ferrihydrite mineral's surface. Phosphate, which is found on native ferritin's mineral surface, gave the largest increase in band gap energy. The significant concentration of oxygen content in the phosphate anion may be the cause of the increased band gap energy which follows the electronegativity trend. The organic molecules citrate and cysteine may have been too large to enter into the protein's interior and gave mixed results for band gap modification. The magnitude of the change in band gap resulting from the surface modifications may be increased by depositing the anions throughout the mineral which is accomplished by co-depositing anions and iron during iron loading and was investigated by our group in a later study.[14]

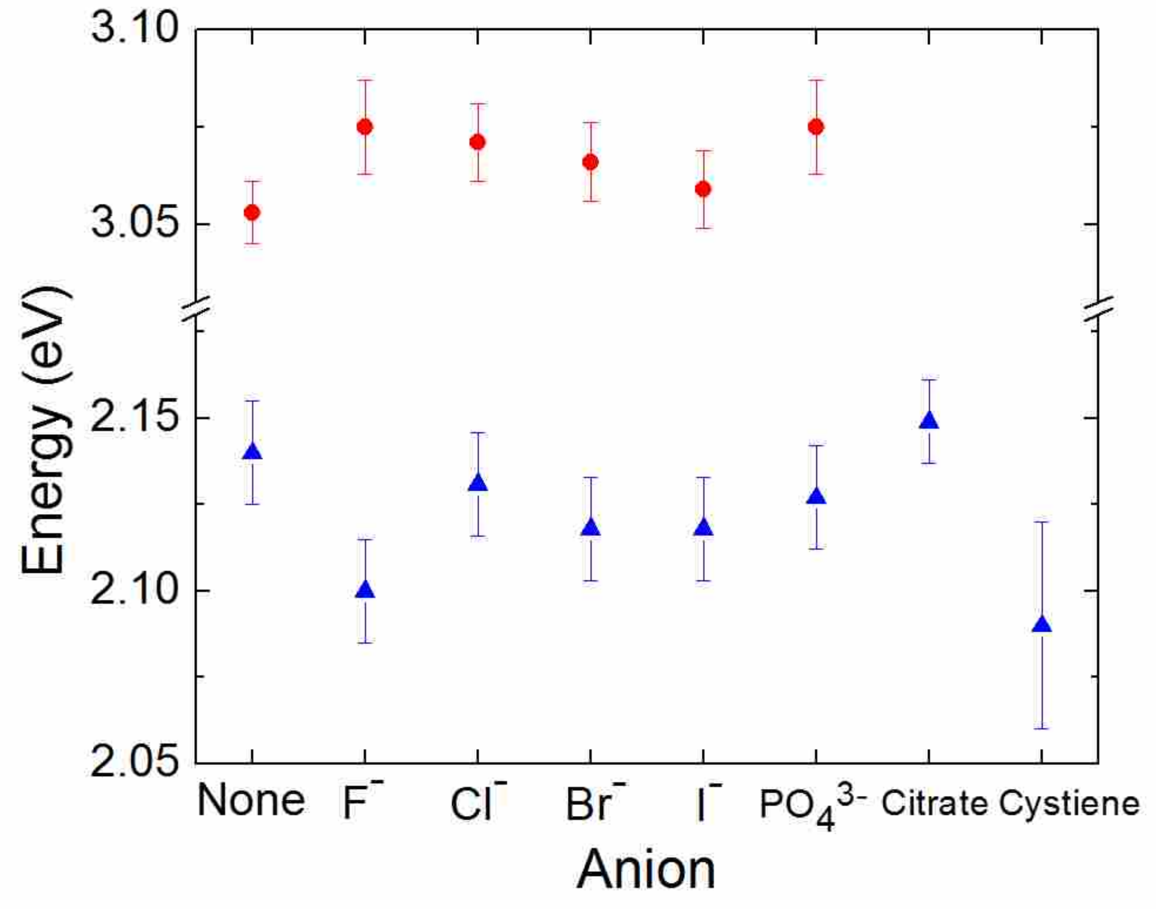

Figure 3 - 3. Direct and indirect band gaps of ferritin's ferrihydrite mineral in the presence of various salts. Direct (red circles) and indirect (blue triangles) band gaps of native ferritin incubated with the sodium salts of halides (F^-, Cl^-, Br^-, and I^-), oxoanions (PO_4^{3-}), and the electron donors citrate (Cit) and cysteine (Cys) (all at 0.2 M). The ions in solution interact with the surface of the ferrihydrite mineral core, altering the band gaps by up to 0.035 eV.

Quantum confinement effects were also measured as a function of core size with reconstituted ferrihydrite ferritin. As is shown in Figure 3-4, the smallest core of 640 Fe/ferritin gave the highest direct and indirect band gap energies of 3.119 ± 0.020 eV and 2.237 ± 0.012 eV, respectively. The larger core size of 1200 Fe/ferritin gave lower direct and indirect band gap energies of 2.896 ± 0.030 eV and 1.916 ± 0.015 eV, respectively. Detailed results of the band gap measurements are shown in Table 3-1.

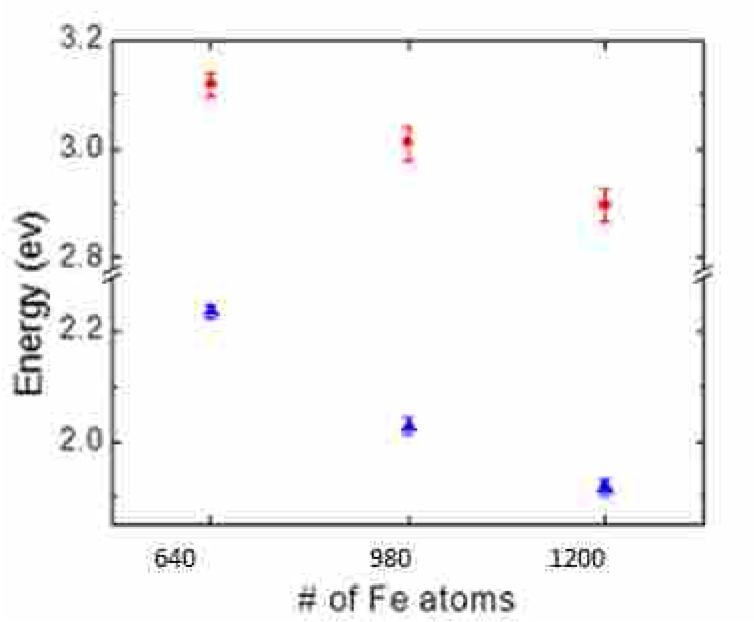

Figure 3 - 4. Direct (red circles) and indirect (blue triangles) band gaps for ferritin loaded with ferrihydrite containing various amounts of iron atoms. Quantum confinement effects are apparent, in that smaller cores yield higher energy band gaps.

Table 3 - 1. Summary of energies plotted in Figures 3-3 and 3-4, with the defect binding energy included. Native ferritin contained 1100 irons per ferritin. Prominent size effects exist, consistent with the presence of quantum confinement. Anions (F-, Cl-, etc.) and electron donors' citrate and cysteine were at 0.2 M in solution in the presence of desalted ferritin, resulting in surface modifications to the ferrihydrite mineral and hence, a small change in band gap.

	$E_{indirect}$ (eV)	$E_{defect\ binding}$ (eV)	E_{direct} (eV)
Native	2.140 ± 0.015	0.220 ± 0.010	3.053 ± 0.080
640 Fe core	2.237 ± 0.012	0.315 ± 0.008	3.119 ± 0.020
980 Fe core	2.027 ± 0.015	0.266 ± 0.010	3.012 ± 0.030
1200 Fe core	1.916 ± 0.015	0.252 ± 0.010	2.896 ± 0.030
F^-	2.119 ± 0.012	0.200 ± 0.010	3.075 ± 0.012
Cl^-	2.131 ± 0.015	0.235 ± 0.010	3.071 ± 0.010
Br^-	2.118 ± 0.015	0.229 ± 0.010	3.066 ± 0.010
I^-	2.118 ± 0.015	0.249 ± 0.010	3.059 ± 0.010
$(PO_4)^{3-}$	2.127 ± 0.015	0.237 ± 0.010	3.075 ± 0.012
Citrate	2.149 ± 0.012	0.232 ± 0.010	3.047 ± 0.010
Cysteine	2.105 ± 0.015	0.188 ± 0.010	3.065 ± 0.008

Conclusion

Optical absorption spectroscopy provided a reliable and consistent method for determining the type of band gap as well as the energy of the band gap transition. The ferrihydrite mineral in ferritin is an indirect band gap semiconductor with an indirect band gap of 2.140 ± 0.015 eV which also contains a direct transition at 3.053 ± 0.008 eV. The OAS technique gave similar direct transition energy as the optical filter colorimetric assay of 2.5-3.5 eV[4] and 3.0-3.5 eV[3].

The band gap energies of the ferrihydrite mineral can be altered through surface modifications of the ferrihydrite mineral and through changing the core size as a result of quantum confinement effects. Co-depositing anions into the ferrihydrite mineral during iron loading may increase the change in band gap energies and will be investigated later.

The original document was published in Nanotechnology February 28th, 2014.[15]

This work was also presented at: Nano and Giga Challenges in Electronics, Photonics, and Renewable Energy 2014; BYU Student Research Conference 2014; The American Physical Society March 2014 meeting; and COMS and Nano-Utah Joint Conference 2014.

References

---

[1] Shockley, W. & Queisser, H. J. Detailed Balance Limit of Efficiency of p-n Junction Solar Cells. *Journal of Applied Physics* **32,** 510–519 (1961).

[2] Medintz, I. L., Uyeda, H. T., Goldman, E. R. & Mattoussi, H. Quantum dot bioconjugates for imaging, labelling and sensing. *Nature materials* **4,** 435–446 (2005).

[3] Keyes, J., Hilton, R., Farrer, J. & Watt, R. Ferritin as a photocatalyst and scaffold for gold nanoparticle synthesis. *J Nanopart Res* **13,** 2563–2575 (2011).

[4] Kim, I., Hosein, H.A., Strongin, D. R. & Douglas, T. Photochemical Reactivity of Ferritin for Cr(VI) Reduction. *Chem. Mater.* **14,** 4874–4879 (2002).

[5] Ensign, D., Young, M. & Douglas, T. Photocatalytic Synthesis of Copper Colloids from Cu(II) by the Ferrihydrite Core of Ferritin. *Inorg. Chem.* **43,** 3441–3446 (2004).

[6] Oscar D. Petrucci. Ferritin-Based Photo-Oxidation of Biomass for Nanoparticle Synthesis, Bioremediation, and Hydrogen Evolution. (Brigham Young University, 2013).

[7] Oscar D. Petrucci. Ferritin-Based Photo-Oxidation of Biomass for Nanoparticle Synthesis, Bioremediation, and Hydrogen Evolution. (Brigham Young University, 2013).

[8] Rakshit, T. & Mukhopadhyay, R. Tuning Band Gap of Holoferritin by Metal Core Reconstitution with Cu, Co, and Mn. *Langmuir* **27,** 9681–9686 (2011).

[9] Colton, J., Erickson, S., Smith, T. & Watt, R. Sensitive detection of surface- and size-dependent direct and indirect band gap transitions in ferritin. *Nanotechnology* **25,** 135703 (2014).

---

[10] Cagle, F. W. & Smith, G. F. 2,2-Bipyridine Ferrous Complex Ion as Indicator in Determination of Iron. *Anal. Chem.* **19,** 384–385 (1947).

[11] Lowry, O. H., Rosebrough, N. J., Farr, A. L. & Randall, R. J. Protein measurement with the Folin phenol reagent. *J biol Chem* **193,** 265–275 (1951).

[12] Peterson, G. L. A simplification of the protein assay method of Lowry et al. which is more generally applicable. *Analytical Biochemistry* **83,** 346–356 (1977).

[13] Joo, M.-S., Tourillon, G., Sayers, D. E. & Theil, E. C. Rapid reduction of iron in horse spleen ferritin by thioglycolic acid measured by dispersive X-ray absorption spectroscopy. *Biology of metals* **3,** 171–175 (1990).

[14] Smith, Trevor J., Stephen D. Erickson, Catalina Matias Orozco, Andrew Fluckiger, Lance M. Moses, John S. Colton, and Richard K. Watt. Tuning the band gap of ferritin nanoparticles by co-depositing iron with halides or oxo-anions. *J. Mater. Chem. A* **2,** 20782–20788 (2014).

[15] Colton, J., Erickson, S., Smith, T. & Watt, R. Sensitive detection of surface- and size-dependent direct and indirect band gap transitions in ferritin. *Nanotechnology* **25,** 135703 (2014).

Chapter 4 – Tuning the Band gap of Ferritin Nanoparticles by Co-Depositing Iron with Halides or Oxo-anions

This chapter was published in Materials Chemistry A, issue 2, pp. 20782-20788, 2014, and is titled "Tuning the Band Gap of Ferritin Nanoparticles by Co-Depositing Iron with Halides or Oxo-Anions."

The work presented here was conducted by me, with assistance from Stephen Erickson, Catalina Orozco, Andrew Fluckiger, and Lance Moses in conducting the experiments. Writing was primarily performed by me, with editing assistance from Dr. John Colton, Dr. Richard Watt, as well as the above mentioned graduate and undergraduate students.

Abstract

Iron-containing ferritin has been used for light harvesting and as a photocatalyst. In this study, we test the hypothesis that changing the iron mineral core composition can alter the light harvesting and photocatalytic properties of ferritin, by co-depositing iron in the presence of halides or oxo-anions. This caused the anions to be incorporated into the iron mineral. We report that some of these new iron minerals possess different band gaps than the original ferrihydrite within ferritin. We found an increase in band gap of up to 0.288 eV or a decrease by as much as 0.104 eV, depending on the type of anion and amount of anions incorporated into the ferrihydrite mineral

Introduction

Nanoparticles (<100 nm) have high photon-exciton conversion efficiencies, which are especially desirable in photovoltaic (PV) devices.[1,2,3] Scientists developing multi-junction PV cells seek to surpass the theoretical efficiency limit of single junction cells[4] by utilizing multiple layers of materials with different band gaps.[5,6,7] The band gap dictates the minimum energy needed to excite an electron into the conduction band, and the amount of useful energy that can be extracted from each excitation. For increased efficiency, each layer must have a greater band gap than the layer below it, reducing the energy lost to heat. However, current methods have only produced a handful of compatible materials,[5] thus severely limiting the ability to develop multi-junction solar cells because of the limited range of materials with the desired band gaps.

The development of multi-junction PV cells with nanoparticles will require: 1) methods to synthesize a library of nanoparticles with the appropriately tuned band gaps; and 2) methods to deposit the nanoparticles in ordered arrays in layers. Ferritin was recently identified as model molecule for PV systems because of its unique properties as a hybrid organic/inorganic photocatalyst.[8] In this study we describe our efforts to design a library of ferritin iron-containing nanoparticles with altered band gaps that can be used in multi-junction PV cells.

Ferritin is the iron storage protein found in virtually every organism. It is a spherical biomolecule measuring 12 nm in diameter with an 8 nm hollow interior and is composed of 24 polypeptide subunits.[9] These subunits form an extremely stable protein complex that is capable of withstanding a pH range of 4-12 and maintain conformation up to 85 °C.[10]

Ferritin binds and mineralizes iron and sequesters it inside the 8 nm diameter protein cage as an iron oxide nanoparticle. The protein is capable of holding up to 4500 iron atoms as an $Fe_2O_3 \bullet 0.5H_2O$ or ferrihydrite mineral (often written as Fe(O)OH for convenience).[11]

The iron mineral can be removed from ferritin by chemical reduction and chelation, producing an empty protein nanocage.[26] The iron core can be reconstituted by adding iron to the empty protein shell (Fig. 3 – 1A).[26] Additionally, non-naturally occurring minerals can be synthesized inside ferritin by a variety of synthetic methods using different metals (Ti, Cr, Mn, Fe, Co, Ni, Cu, Eu and U) and anions (S, Se, PO_4^{3-}, AsO_4^{3-}, VO_3^{-}, MoO_4^{2-}, WO_4^{2-}).[8,12,13,14,15,] Therefore, a library of ferritin nanoparticle materials is available to be studied.

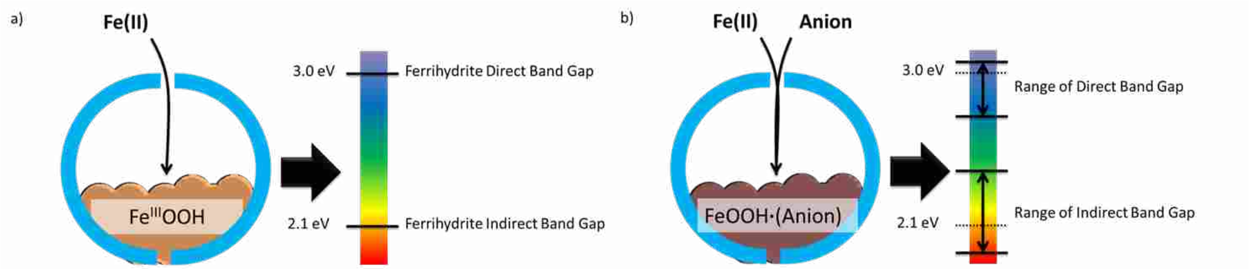

Figure 4 - 1. Scheme of band gap alterations using anion deposition in ferritin. a) The natural ferrihydrite mineral band gap is shown on a color scale, with the direct and indirect band gap energies. b) An anion co-deposited iron core, showing the extent of band gap variation possible by co-depositing various anions. The direct and indirect band gaps from figure 4-1(a) are shown as a dotted line in figure 4-1(b).

The protein shell of ferritin also provides unique handles for materials science applications. For instance, the protein shells of ferritin will self-assemble on surfaces such as silica or gold in hexagonally close packed arrays.[16] Additionally, the organic shell can be functionalized and organized in architectures of 2- and 3-dimensional structures.[17,18] The ability to assemble ferritin and its encapsulated mineral in ordered arrays and layers, particularly on transparent electrode surfaces such as indium tin oxide electrodes[19], makes ferritin an appealing substrate for multi-junction PV cells.

Upon illumination, ferritin absorbs light, creating excitons where the excited electrons have been used to reduce a variety of species (Au,[20] Cr,[21] Cu,[22] Cytochrome c and Viologens[23]). Nikandrov demonstrated that the light absorption takes place in the ferrihydrite core, a semiconducting material whose band gap has been reported by several groups.[20,21,24,25]

Recently, Colton et al.[25] used Optical Absorption Spectroscopy (OAS) to establish the native ferrihydrite mineral in ferritin as an indirect band gap semiconductor, and accurately measured an indirect band gap at 2.140 ± 0.010 eV (579.7 nm), a direct transitions (sometimes called a direct band gap) at 3.053 ± 0.005 eV (406.1 nm), and a defect-related state having a binding energy of 0.220 ± 0.010 eV.

The ability to synthesize artificial minerals inside ferritin expands the potential light harvesting materials that can be prepared. In this paper, we study altered iron-containing ferritin minerals. Polanams et al.[14] were able to co-deposit oxo-anions into the ferrihydrite mineral during iron loading, and reported that co-deposition changed the iron loading kinetics. The UV/Vis absorption spectrum of each of these ferritin iron/oxo-anions complexes was different, indicating changes to the mineral and the band gap of each mineral. Hilton et al.[26] were able to reduce the ferrihydrite mineral in the presence of different anions to create an Fe(X)OH core, where the symbol X in the chemical formula represents halides or oxo-anions. The ferritin solution went from a red-orange color to a pale yellow as the iron was reduced from FeIII to FeII. This significant color change is indicative of a change in band gap. Based on these observations, Colton et al.[25] tested the effect of halides that associated with the surface of the iron mineral in ferritin and observed that halides slightly altered the band gaps of the ferrihydrite mineral.

In this study, we test the hypothesis that the co-deposition of iron and anions into ferritin alters the band gap of the new iron mineral in ferritin. We synthesized and characterized these new anion-containing iron minerals formed in ferritin and employed OAS to measure the band gaps of these ferritins. We report new band gap energies for these new ferritin minerals and compare them to the natural iron core (ferrihydrite) of ferritin. Figure 4-1 schematically represents how the minerals were synthesized and represents that an altered band gaps were observed.

Recently, Colton et al.[25] used Optical Absorption Spectroscopy (OAS) to establish the native ferrihydrite mineral in ferritin as an indirect band gap semiconductor, and accurately measured an indirect band gap at 2.140 ± 0.010 eV (579.7 nm), a direct transitions (sometimes called a direct band gap) at 3.053 ± 0.005 eV (406.1 nm), and a defect-related state having a binding energy of 0.220 ± 0.010 eV.

The ability to synthesize artificial minerals inside ferritin expands the potential light harvesting materials that can be prepared. In this paper, we study altered iron-containing ferritin minerals. Polanams et al.[14] were able to co-deposit oxo-anions into the ferrihydrite mineral during iron loading, and reported that co-deposition changed the iron loading kinetics. The UV/Vis absorption spectrum of each of these ferritin iron/oxo-anions complexes was different, indicating changes to the mineral and the band gap of each mineral. Hilton et al.[26] were able to reduce the ferrihydrite mineral in the presence of different anions to create an Fe(X)OH core, where the symbol X in the chemical formula represents halides or oxo-anions. The ferritin solution went from a red-orange color to a pale yellow as the iron was reduced from FeIII to FeII. This significant color change is indicative of a change in band gap. Based on these observations, Colton et al.[25] tested the effect of halides that associated with the surface of the iron mineral in ferritin and observed that halides slightly altered the band gaps of the ferrihydrite mineral.

In this study, we test the hypothesis that the co-deposition of iron and anions into ferritin alters the band gap of the new iron mineral in ferritin. We synthesized and characterized these new anion-containing iron minerals formed in ferritin and employed OAS to measure the band gaps of these ferritins. We report new band gap energies for these new ferritin minerals and compare them to the natural iron core (ferrihydrite) of ferritin. Figure 4-1 schematically represents how the minerals were synthesized and represents that an altered band gaps were observed.

Experimental

Apoferritin was prepared by removing the iron from horse spleen ferritin (Sigma-Aldrich CAS# F4503) using established methods.[14,27] Native ferritin was dialyzed against thioglycolic acid and 0.050 M tris(hydroxymethyl)aminomethane (TRIS) to remove all iron from ferritin. The resulting iron free ferritin was then dialyzed against Milli-Q water in 0.10% bicarbonate buffer at pH 7.4. Further dialysis was used to exchange ferritin into imidazole buffer

Reconstituted ferrihydrite cores with no anions present were made by adding iron to an iron free ferritin solution (5 mg/mL, 1.11 x 10^{-5} M) in an imidazole buffer (prepared at 1M pH 7.4) with a final volume of 1.5 mL. The pH of the solution was kept at pH 7.4 by careful titration with NaOH. We have observed an aging effect where the measured band gap slowly changes with time (several hours to 1 day) immediately after the synthesis of a new core. This aging effect is presumably due to the reorganization of the mineral to its most stable state. For this study, all cores were aged for 5 days, far longer than was necessary to be certain that the mineralization process was complete. The mineral core synthesis was performed by adding 10 mM ferrous ammonium sulfate prepared in 10 mM nitric acid at a rate no greater than 100 irons per ferritin per 10 minutes. The pH was maintained at 7.4 by adding NaOH to neutralize acid produced from iron mineralization. Core sizes were selected between 500-2000 Fe/ ferritin.

Co-deposition of halides was achieved by loading iron into ferritin using the same method as above, but preparing the buffer solution with 200 mM concentrations of the desired sodium halide salt (except for fluoride, which was kept at 1 mM due to significant inhibition of iron loading with the higher fluoride concentrations).

Co-deposition of oxo-anions was performed by adding iron into a ferritin solution containing 1 mM sodium oxo-anion. Additional samples with higher oxo-anion concentrations of 5 mM oxo-anion were prepared by simultaneous additions in separate injections of 100 mM oxo-anion and 100 mM ferrous ammonium sulfate prepared in 10 mM nitric acid, at a rate no greater than 50 irons per 10 minutes up to a targeted bulk state (>900 Fe/ferritin). The pH was maintained at 7.4 by titration with 300 mM sodium hydroxide. All samples were mixed with a BioRad P-10 slurry in a 1:1 volume ratio to remove any iron-oxo-anion polymers.[28] A BioRad P-10 slurry solution was mixed on a rocking platform for at least 30 min and then centrifuged and the ferritin supernatant was decanted. The decanted iron-polymer free solutions were then passed over a Sephadex G-75 desalting column with 50 mM pH 7.4 imidazole buffer.

The iron content of each sample was determined by treating the ferritin samples with bypyridine and dithionite and measuring the iron-bipyridine absorbance at 522 nm (ϵ522=8650 M-1 cm-1).[29] The protein content was measured by the Lowry method,[30] and a ratio between the iron and protein concentration gave the relative Fe/ferritin ratio.

The halides and phosphate which were co-deposited into the ferrihydrite mineral cores were measured using Orion Ion Selective Electrodes (ISE), and additional elemental analysis was performed using inductively coupled plasma-mass spectrometry (ICP-MS) for all oxo-anion samples.

Band gaps were measured by optical absorption spectroscopy using a setup as described by Colton et al.[25] All samples were prepared and allowed to stabilize for 5 days after core re-mineralization to insure a stable mineral for band gap measurements.

Transmission Electron Microscopy (TEM) images were taken of all samples using a Tecnai F30 in parallel imaging mode. Energy Dispersive X-ray (EDX) spectrometry was conducted with an EDAX attached to a Tecnai F20 TEM. ImageJ was used to measure core size using an average of over 80 cores per sample. A representative figure of the TEM analysis is shown in Figure 4-2 with the data for all other samples available in the supplemental data at the end of the chapter.

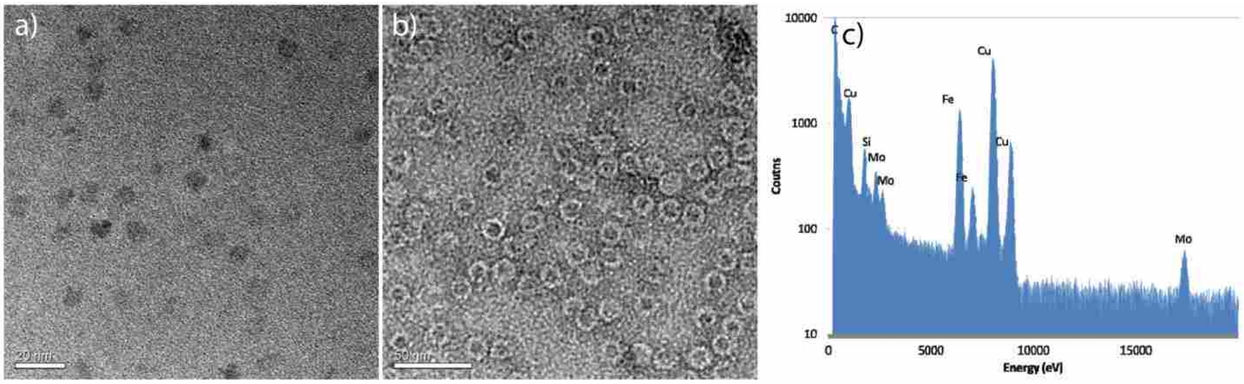

Figure 4 - 2. TEM images and EDX analysis of ferritin containing co-deposited iron and MoO_4^{2-}. a) Unstained TEM image of ferritin with an iron and molybdate core ($Fe(O)OH{\cdot}(MoO_4)$). b) Uranyl acetate stained iron and molybdate ferritin sample showing protein with the mineral core inside. c) EDX analysis from TEM showing molybdenum and iron content from Figure 4-3a. Additional figures for each anion co-deposited sample can be seen in the supplemental data.

Co-deposition anion	Iron per Ferritin	Anion per Ferritin	Core Size (nm)	Indirect Band Gap (eV)	Change in Indirect (eV)	Direct Band Gap	Change in Direct (eV)
No Salt – Bulk	900 ± 71	n/a	9.05 ± 1.44	2.092 ± 0.011	n/a	2.992 ± 0.012	n/a
Halides							
F^-	2650 ± 430	260	Not measured	2.078 ± 0.012	-0.014	2.991 ± 0.008	-0.001
Cl^-	2090 ± 280	210	9.11 ± 0.92	2.077 ± 0.012	-0.015	2.974 ± 0.010	-0.018
Br^-	2400 ± 250	240	9.25 ± 0.55	2.032 ± 0.012	-0.06	2.942 ± 0.016	-0.05
I^-	2600 ± 300	260	9.33 ± 0.92	2.050 ± 0.012	-0.042	2.934 ± 0.014	-0.058
1 mM Oxo-Anion							
PO_4^{3-}	2000 ± 400	185 ± 20	Not measured	2.139 ± 0.010	0.047	3.009 ± 0.008	0.017
MnO_4^{2-}	2000 ± 300	75 ± 1	Not measured	2.080 ± 0.010	-0.012	2.994 ± 0.008	0.002
MoO_4^{2-}	1175 ± 200	95 ± 2	Not measured	2.116 ± 0.012	0.024	2.990 ± 0.010	-0.002
WO_4^{2-}	1750 ± 100	1000 ± 10	Not measured	2.215 ± 0.012	0.123	3.058 ± 0.008	0.066
5 mM Oxo-Anion							
PO_4^{3-}	430 ± 53	60 ± 5	Not measured	2.380 ± 0.024	0.288	3.231 ± 0.014	0.239
MnO_4^{2-}	127 ± 24	112 ± 1	8.38 ± 0.67	1.988 ± 0.012	-0.104	2.878 ± 0.010	-0.114
MoO_4^{2-}	1075 ± 140	345 ± 3	8.58 ± 0.81	2.113 ± 0.010	0.021	3.001 ± 0.010	0.009
WO_4^{2-}	1060 ± 120	1430 ± 10	8.26 ± 1.01	2.242 ± 0.010	0.15	3.062 ± 0.012	0.07

Table 4 - 1. Reported metals per ferritin, anion co-deposition, and band gap values. It should be noted that the 1 mM and 5 mM titles are for the concentration of oxo-anions used during synthesis, and not the actual concentration of the anions present inside the ferritin protein. The "Change in Indirect" and "Change in Direct" columns indicate the variation in band gap relative to the "No Salt – Bulk" values. Also see Figure 2 – (3, 4, and 5).

Results and Discussion

Sample Characterization

The newly synthesized ferritin cores that contained co-deposited anions were characterized to determine the extent of anion incorporation in the minerals. First, we performed TEM to confirm that the iron and anions were actually deposited inside the ferritin interior. TEM analysis of the samples showed nanoparticles of ~9 nm diameter (Fig. 3A) consistent with the size of the ferritin interior. Negative staining of the samples showed that these nanoparticles were present inside the ferritin protein shell (Fig 3B). EDX analysis also showed the expected composition of iron and the appropriate anion in the mineral analysis (Fig. 3C shows representative data for the iron molybdate ferritin sample). The TEM analysis of the other ferritin samples is presented in the supplemental data section. The silicon and copper peaks are from the silicon detector in the instrument, and the copper grids used to image the ferritin samples, respectively.

Additional elemental analysis of the samples was performed to determine the amount of the anions deposited in ferritin by using ion-selective electrodes (ISEs) and ICP-MS. These results are summarized in Table 4 - 1.

Effect of Core Size

Previously, Colton et al.[25] demonstrated a quantum confinement effect where smaller ferritin cores possessed a larger band gap than larger ferritin cores. As we initiated studies on these new ferritin cores with co-deposited anion and iron cores we recognized the importance of evaluating if these new samples exhibited any quantum confinement effects. Figure 4-3 shows that small cores do have larger band gaps, however, when the core sizes exceeded 900 irons per ferritin, a "bulk-like" state was observed where the band gap no longer varies with size (See

Figure 4-3). By defining the “bulk-like” state as cores >900 Fe/ferritin we were able to define deviations from the ferrihydrite band gap as being due to the co-deposition of the anions and not due to quantum confinement effects. Any changes in band gap mentioned in this manuscript will be in relation to this “bulk-like” state.

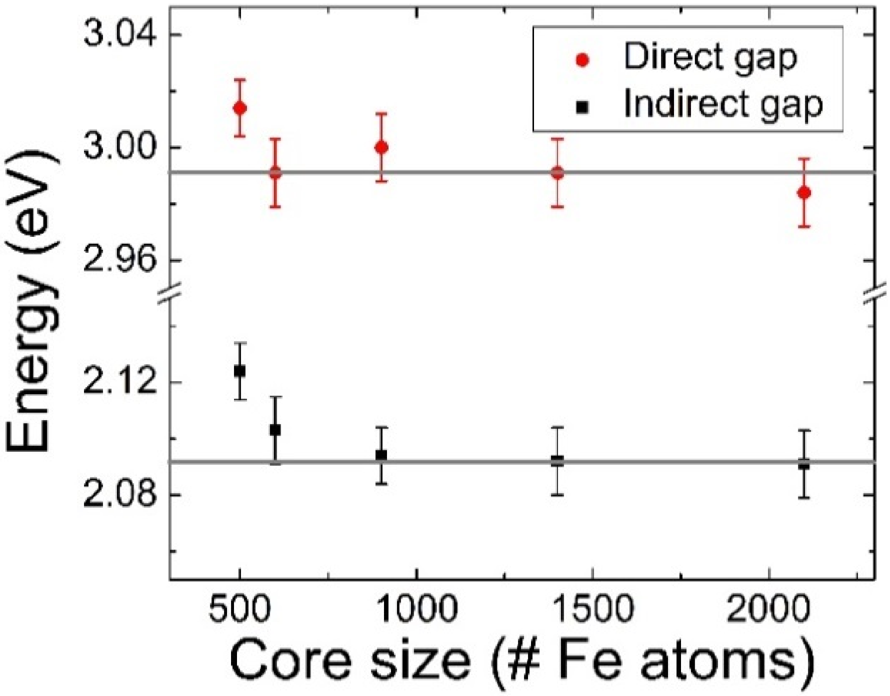

Figure 4 - 3. Reconstituted ferrihydrite cores with no anions present. The gray lines show the band gap of bulk-like Nano crystals.

Effect of Halides

Halides were successfully deposited into the ferrihydrite mineral as shown in Table 4-1. These minerals were synthesized in the presence of 200 mM halide concentrations to allow for a greater probability that an anion would co-deposit with iron during mineralization into ferritin. Colton et al.[25] showed that adsorbing halides to the ferrihydrite surface using salts in solution slightly lowered the indirect band gap, by about 0.010-0.020 eV, but increased the direct band gap (0.010 to 0.050) [See reference 25, Figure 5]. We tested the hypothesis that anion co-deposition inside the mineral would further alter the band gap of these iron/halide minerals. ISE analysis showed that approximately one halide per ten iron ions was found in the new ferritin mineral (Table 4-1). Anion co-deposition with iron was accompanied by a decrease in band gap, particularly for Br^- and I^-. The band gap changes were much more profound for the co-deposited halides than the surface adsorbed halides [See reference 25, Figure 5]. The results show that anions deposited in the mineral core lowered the direct band gap by as much as 0.058 eV in the case of I^-, and the indirect band gap by 0.060 eV in the case of Br^- (Figure 4-4, Table 4-1).

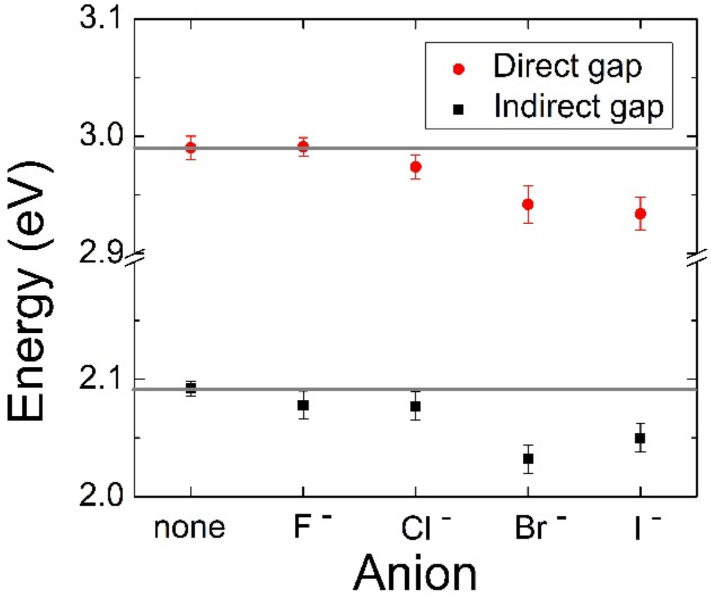

Figure 4 - 4. Band gap measurements of ferritin minerals synthesized by co-depositing iron and halides. The gray lines correspond to the direct and indirect band gaps from the bulk ferrihydrite control. (See Table 4-1 for a detailed listing of core size, anion incorporation, and band gap.)

Effect of Oxo-Anions

Ferritin iron cores were synthesized with oxo-anions following the method of Polanams et al.[14] These samples also showed variations in the band gap compared to the ferritin ferrihydrite control (Fig. 3-4, Table 4-1). Ferritin oxo-anion samples were prepared using two different oxo-anion concentrations during synthesis, namely 1 mM and 5 mM. This allowed us to study alterations to the band gap in preparation of ferritin minerals with different iron to oxo-anion ratios (See total oxo-anions deposited in mineral cores with different synthesis concentration, 1 mM or 5 mM in Table 4-1). We will refer to these distinct samples as the 1 mM and 5 mM samples throughout the rest of the manuscript, however these concentrations do not refer to the actual amount of oxo-anion incorporated, they refer to the synthesis conditions. The actual oxo-anion concentration present in the sample is indicated in Table 4-1. These different synthesis concentrations were chosen because it is known that some oxo-anions form polymers with iron in solution and inhibit the iron loading process into ferritin.[31] By varying these synthesis conditions we were able to prepare ferritins with different iron to oxo-anion ratios. We removed the iron oxo-anion polymeric complex from solution so that only the ferritin samples containing iron and oxo-anions were studied for band gap measurements.

We expected approximately 10-30% oxo-anion substitution based on the results of Johnson et al,[32] and Polanams et al,[14] who showed that phosphate as well as other oxo-anions are able to co-deposit in reconstituted ferritin cores in ratios between 10% and 30% of the total iron content. We used BioRad P-10 slurry to filter out iron oxo-anion polymers not sequestered inside ferritin[25], resulting in our samples having between 15% and 30% loading. As expected, the ferritin samples prepared in the presence of 5 mM oxoanions loaded a greater percentage of oxo-anions but had smaller total iron content due to complex formation outside of ferritin (Table 4-1).

It should be noted that phosphate inhibits iron loading into ferritin, and would account for the low iron loading in the 5 mM sample.[33]

The 1 mM PO_4^{3-} sample prepared in this study had 2000 iron atoms per ferritin with approximately 10% phosphate. We report a direct band gap of 3.009 eV and an indirect band gap of 2.139 eV. The iron/phosphate ratio in this synthetic core is similar to native ferritin isolated from horse spleen. Colton et al.[25] studied a native ferritin sample with an iron core of 1100 iron/ferritin with 10 % phosphate. Colton et al.[25] also reported a direct band gap value of 3.053 eV and an indirect band gap of 2.140 eV. Comparison of these two samples showed good agreement (Figure 4-5, Table 4-1).

As expected, the ferritin sample prepared in the 5 mM phosphate solution produced a much smaller iron core (Table 4-1). The band gap of the sample prepared in the presence of 5 mM phosphate had a 0.288 eV increase in indirect band gap versus the bulk iron state (Figure 4-5, Table 4-1). This change in band gap is a combination of two influencing factors. The first is the quantum confinement effect due to the small size of the 500 Fe/ferritin. If we directly compare the indirect band gap of the sample prepared in 5 mM phosphate that contains 500 Fe/ferritin (Indirect band gap = 2.380 eV) to an the iron core of a 500 Fe/ferritin prepared in the absence of phosphate (Fig 3-3, Indirect band gap = 2.127 eV) we see an increase in the band gap of 0.256 eV. However, the 500 iron/ferritin sample had a quantum confinement increase in band gap of only 0.032 eV compared to the iron ferritin sample with the “bulk state” of 900 Fe/ferritin. Therefore, the contribution to the increased band gap corresponding to the quantum confinement effect in the 500 Fe/ferritin sample containing phosphate is small compared to the influence of phosphate on the iron core.

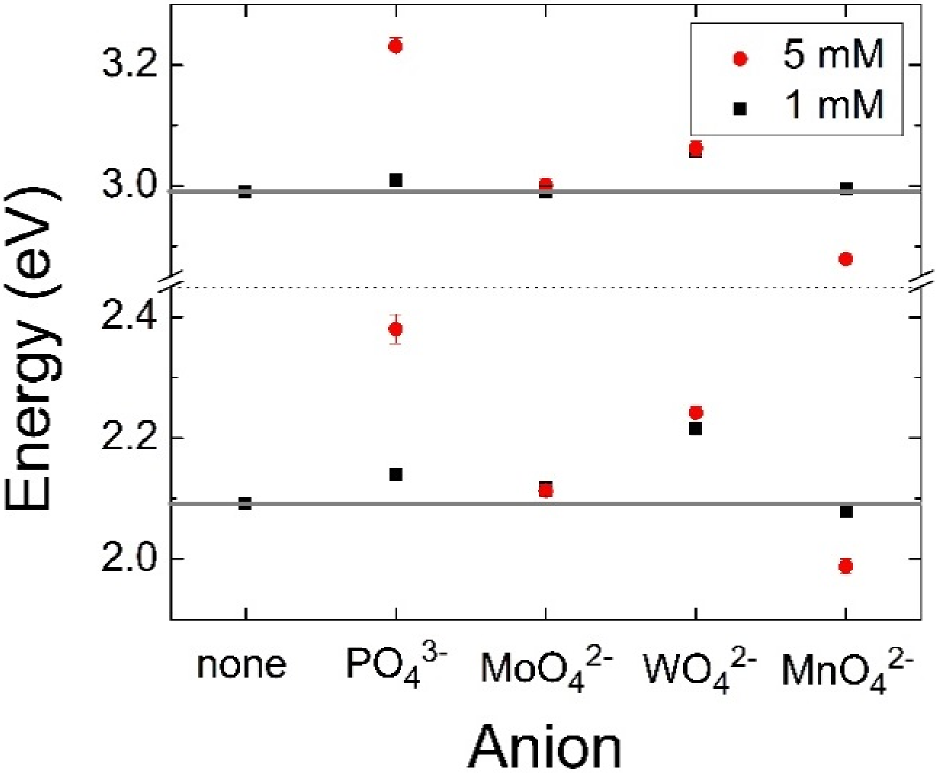

Figure 4 - 5. Ferritin samples synthesized in the presence of 1 mM oxo-anion, and ferritin samples synthesized in the presence of 5 mM oxo-anion. The gray lines correspond to the direct and indirect band gaps from the "bulk-like" ferrihydrite state. The dotted line shows a break in the y-axis separating the higher energy direct gaps from the lower energy indirect gaps. Please note that the x-axis simply denotes the anion used in the synthesis of the iron core and does not attempt to designate any other type of additional trends such as anion size, etc.

The molybdate samples did not show a significant shift in band gap (Figure 4-5, Table 4-1). Both samples were large enough to be in the bulk-like state with 6-30% Mo loading, but neither showed much difference in band gap, suggesting no additional benefit for PV applications by co-depositing molybdate into ferritin.

In contrast, the tungstate sample showed much higher levels of co-deposition, with tungsten to iron ratios greater than one for the 5 mM sample (Table 4-1). This suggests that a tungsten-iron oxide mineral was formed. Both tungstate samples had cores large enough to be in the bulk state, attributing increases in band gap to the co-deposition of the oxo-anions into the iron mineral. Both indirect and direct gaps showed increases in the band gaps, with greater increases in band gap from the greater molybdate co-deposition (Fig. 3-5). Specifically, the 1 mM sample showed increases of 0.123 eV for the indirect band gap and 0.066 eV for the direct band gap, while the 5 mM sample showed increases of 0.15 eV for the indirect band gap and 0.070 eV for the direct band gap (Figure 4-5, Table 4-1).

The use of the oxo-anion permanganate is different than the other oxo-anions used in this study because it is a potent oxidizing agent. We recognized that two possible reactions could occur by adding permanganate with Fe(II) to the ferritin solution. The first is that the permanganate might simply become incorporated into the iron core in a similar fashion to the other oxo-anions. The second is that permanganate might act as an electron acceptor and rapidly oxidize the Fe(II) to Fe(III) during iron loading into ferritin. Additionally the lower valent manganese produced from permanganate oxidation might be co-deposited with iron inside ferritin creating a new mixed mineral phase of iron and manganese.

The 1 mM permanganate sample showed that about 8% of the core was manganese and the rest iron (2000 Fe/ ferritin). The 1 mM permanganate sample showed no significant change in either band gap outside of the error bars shown indicating the sample still possessed a “ferrihydrite-like” core.

In contrast, the 5 mM permanganate sample loaded significantly less iron (~127 Fe/ ferritin) but the resulting core was approximately 1 Fe:1 Mn. This 1:1 ratio suggests that instead of forming a ferrihydrite mineral, a new manganese-iron oxide mineral is formed. This sample decreased both the indirect band gap by 0.104 eV and the direct band gap by 0.114 eV from the ferrihydrite control. The quantum confinement effect observed for cores smaller than 900 irons/ferritin (Fig. 3-3) would suggest that the band gaps should increase when compared to the ferrihydrite ferritin core. In fact, the opposite effect occurred and we observed a decrease in band gap for the co-deposition of iron and manganese into the same mineral. This is clear evidence that a mineral very different from the natural ferrihydrite mineral has been formed in these samples. These results further show the strong effects of the manganese ions in influencing the mineral to produce smaller band gaps. Large minerals of the same 1:1 Fe:Mn may have even lower band gaps when the "bulk like" state is formed and the quantum confinement effect is mitigated. A future study will be conducted to better characterize this new iron-manganese oxide nano-material.

Conclusion

In this report we synthesized a variety of ferritin iron minerals co-deposited with halides or oxo-anions with the goal of perturbing the crystal lattice of the new mineral sufficiently to alter the band gap of the material. Such mineral alterations should allow the new materials different properties for light harvesting from the visible spectrum.

We report the successful synthesis and characterization of ferritin minerals that have iron and halides or iron and oxo-anions co-deposited inside the ferritin protein shell. The direct and indirect band gaps of each of these samples were measured using OAS techniques. We report quantum confinement effects for cores smaller than 900 Fe/ferritin. However, once the core reaches 900 Fe/ferritin a ‘bulk-like” state is achieved and any alterations of the band gap are due to the new mineral phase.

Of the halides, bromide and iodide showed a significant decrease in both the direct and indirect band gap where the other halides did not alter the band gaps. Phosphate and tungstate showed significant increases in both the direct and indirect band gaps where molybdenum did not alter either band gap. The magnitude of band gap shift was further affected by the extent of the anion/oxo-anion incorporated into the ferrihydrite mineral. In the case of permanganate the 5 mM sample, formed a new mineral as shown by 1:1 or greater manganese to iron ratio and a large decrease in band gaps. The band gap range for these new minerals spans from 2.878 eV (430.8 nm) to 3.231 eV (383.7 nm) for the direct gap, and from 1.988 eV (623.7 nm) to 2.380 eV (520.9 nm) for an indirect band gap. The new range of band gaps is represented in Figure 4–1(b).

This work was published by Materials Chemistry A, 2014.[34]

This work was also presented at: Nano and Giga Challenges in Electronics, Photonics, and Renewable Energy 2014; The American Physical Society March 2014 meeting; and COMS and Nano-Utah Joint Conference 2014.

Supplemental Figures

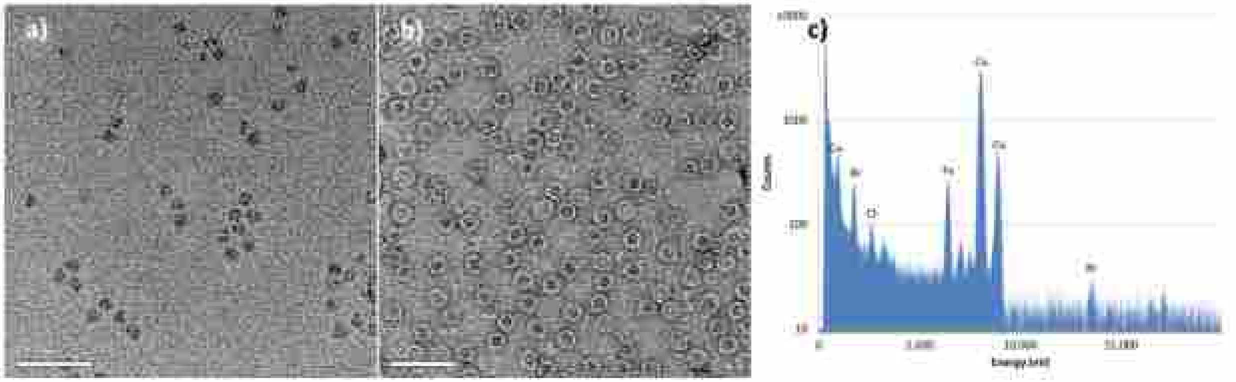

Supplemental Figure 4 - 1. Bromide co-deposited ferritin. a) Unstained TEM image of the ferritin cores. b) Stained ferritin samples with uranyl acetate. c) EDX analysis of bromide deposited cores.

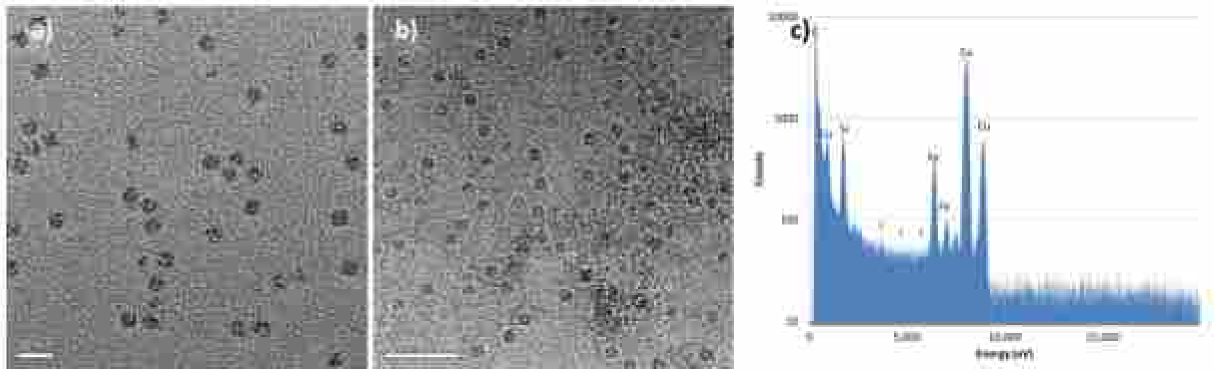

Supplemental Figure 4 - 2. Iodide co-deposited ferritin. a) Unstained TEM image of the ferritin cores. b) Stained ferritin samples with uranyl acetate. c) EDX analysis of iodine deposited cores.

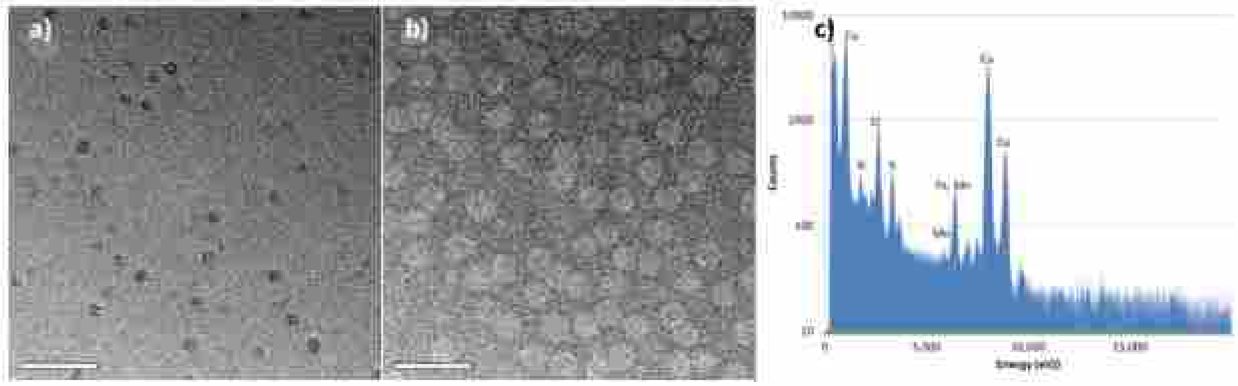

Supplemental Figure 4 - 3. Manganese co-deposited ferritin. a) Unstained TEM image of the ferritin cores. b) Stained ferritin samples with uranyl acetate. c) EDX analysis of manganese deposited cores. Fe and Mn have the same x-ray emission peak at about 6 keV.

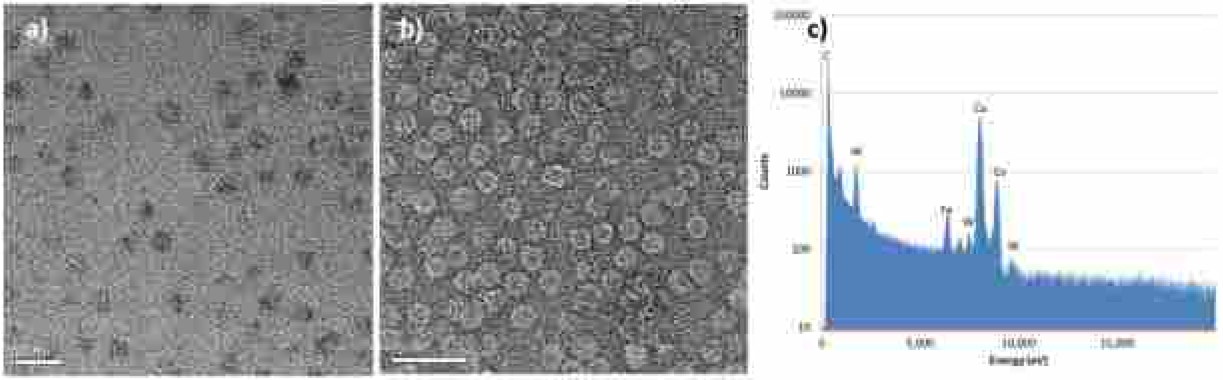

Supplemental Figure 4 - 4. Tungstate co-deposited ferritin. a) Unstained TEM image of the ferritin cores. b) Stained ferritin samples with uranyl acetate. c) EDX analysis of tungsten deposited cores.

Supplemental Table 4 - 1. Iron content and Band Gap measurements. The “bulk-like” state where changes in nanoparticle size no longer significantly affects the band gap measurements occurs at core sizes larger than 900 irons per ferritin.

Reconstituted FTN (Fe/FTN)	**Direct Band Gap (eV)**	**Indirect Band Gap (eV)**
Native Ferritin - 1100	3.05 ± 0.08	2.14 ± 0.02
200	3.02 ± 0.01	2.11 ± 0.01
500	3.01 ± 0.01	2.12 ± 0.01
600	2.99 ± 0.01	2.10 ± 0.01
900	3.00 ± 0.01	2.09 ± 0.01
1400	2.99 ± 0.01	2.09 ± 0.01
2100	2.98 ± 0.01	2.09 ± 0.01

References

---

[1] Nozik, A. J. Exciton Multiplication and Relaxation Dynamics in Quantum Dots: Applications to Ultrahigh-Efficiency Solar Photon Conversion†. *Inorg. Chem.* **44,** 6893–6899 (2005).

[2] Schaller, R. D., Sykora, M., Pietryga, J. M. & Klimov, V. I. Seven Excitons at a Cost of One: Redefining the Limits for Conversion Efficiency of Photons into Charge Carriers. *Nano Lett.* **6,** 424–429 (2006).

[3] S Kim, S. J., Kim, W. J., Sahoo, Y., Cartwright, A. N. & Prasad, P. N. Multiple exciton generation and electrical extraction from a PbSe quantum dot photoconductor. *Applied Physics Letters* **92,** 031107 (2008).

[4] Shockley, W. & Queisser, H. J. Detailed Balance Limit of Efficiency of p-n Junction Solar Cells. *Journal of Applied Physics* **32,** 510–519 (1961).

[5] Green, M. A., Emery, K., Hishikawa, Y., Warta, W. & Dunlop, E. D. Solar cell efficiency tables (version 42). *Progress in Photovoltaics: Research and Applications* **21,** 827–837 (2013).

[6] R. King, D. Law, K. Edmondson, C. Fetzer, G. Kinsey,H. Yoon, R. Sherif, N. Karam. 40% efficient metamorphic GaInP/GaInAs/Ge multijunction solar cells. *Applied physics letters* **90,** 183516–183900 (2007).

---

[7] De Vos, A. Detailed balance limit of the efficiency of tandem solar cells. *Journal of Physics D: Applied Physics* **13,** 839 (1980).

[8] Watt, R. K., Petrucci, O. D. & Smith, T. Ferritin as a model for developing 3rd generation nano architecture organic/inorganic hybrid photo catalysts for energy conversion. *Catal. Sci. Technol.* **3,** 3103–3110 (2013).

[9] Lawson, D. M. *et al.* Solving the structure of human H ferritin by genetically engineering intermolecular crystal contacts. *Nature* **349,** 541–544 (1991).

[10] Hoppler, M., Schönbächler, A., Meile, L., Hurrell, R. F. & Walczyk, T. Ferritin-Iron Is Released during Boiling and In Vitro Gastric Digestion. *The Journal of Nutrition* **138,** 878–884 (2008).

[11] Ford, G. C., P. M. Harrison, D. W. Rice, J. M. A. Smith, A. Treffry, J. L. White, and J. Yariv. Ferritin: Design and Formation of an Iron-Storage Molecule. *Philosophical Transactions of the Royal Society of London. B, Biological Sciences* **304,** 551–565 (1984).

[12] Douglas, T. & Stark, V. T. Nanophase Cobalt Oxyhydroxide Mineral Synthesized within the Protein Cage of Ferritin. *Inorg. Chem.* **39,** 1828–1830 (2000).

[13] Galvez, N., Sanchez, P. & Dominguez-Vera, J. M. Preparation of Cu and CuFe Prussian Blue derivative nanoparticles using the apoferritin cavity as nanoreactor. *Dalton Trans.* 2492–2494 (2005).

[14] Polanams, J., Ray, A. D. & Watt, R. K. Nanophase Iron Phosphate, Iron Arsenate, Iron Vanadate, and Iron Molybdate Minerals Synthesized within the Protein Cage of Ferritin. *Inorg. Chem.* **44,** 3203–3209 (2005).

[15] Watt, R. K., Frankel, R. B. & Watt, G. D. Redox reactions of apo mammalian ferritin. *Biochemistry* **31,** 9673–9679 (1992).

[16] Tominaga, M., Ohira, A., Yamaguchi, Y. & Kunitake, M. Electrochemical, AFM and QCM studies on ferritin immobilized onto a self-assembled monolayer-modified gold electrode. *Journal of Electroanalytical Chemistry* **566,** 323–329 (2004).

[17] Li, M. & Mann, S. DNA-directed assembly of multifunctional nanoparticle networks using metallic and bioinorganic building blocks. *J. Mater. Chem.* **14,** 2260–2263 (2004).

[18] Wong, K. K. ., Cölfen, H., Whilton, N. T., Douglas, T. & Mann, S. Synthesis and characterization of hydrophobic ferritin proteins. *Journal of Inorganic Biochemistry* **76,** 187–195 (1999).

[19] Pyon, M.-S., Cherry, R. J., Bjornsen, A. J. & Zapien, D. C. Uptake and Release of Iron by Ferritin Adsorbed at Tin-Doped Indium Oxide Electrodes. *Langmuir* **15,** 7040–7046 (1999).

---

[20] Keyes, J., Hilton, R., Farrer, J. & Watt, R. Ferritin as a photocatalyst and scaffold for gold nanoparticle synthesis. *J Nanopart Res* **13,** 2563–2575 (2011).

[21] Kim, I., Hosein, H.-A., Strongin, D. R. & Douglas, T. Photochemical Reactivity of Ferritin for Cr(VI) Reduction. *Chem. Mater.* **14,** 4874–4879 (2002).

[22] Ensign, D., Young, M. & Douglas, T. Photocatalytic Synthesis of Copper Colloids from Cu(II) by the Ferrihydrite Core of Ferritin. *Inorg. Chem.* **43,** 3441–3446 (2004).

[23] Nikandrov, V. V., Grätzel, C. K., Moser, J.-E. & Grätzel, M. Light induced redox reactions involving mammalian ferritin as photocatalyst. *Journal of Photochemistry and Photobiology B: Biology* **41,** 83–89 (1997).

[24] Rakshit, T. & Mukhopadhyay, R. Tuning Band Gap of Holoferritin by Metal Core Reconstitution with Cu, Co, and Mn. *Langmuir* **27,** 9681–9686 (2011).

[25] Colton, J., Erickson, S., Smith, T. & Watt, R. Sensitive detection of surface- and size-dependent direct and indirect band gap transitions in ferritin. *Nanotechnology* **25,** 135703 (2014).

[26] Hilton, R. J., Zhang, B., Martineau, L. N., Watt, G. D. & Watt, R. K. Anion deposition into ferritin. *Journal of Inorganic Biochemistry* **108,** 8–14 (2012).

[27] Joo, M.S., Tourillon, G., Sayers, D. E. & Theil, E. C. Rapid reduction of iron in horse spleen ferritin by thioglycolic acid measured by dispersive X-ray absorption spectroscopy. *Biology of metals* **3,** 171–175 (1990).

[28] R. Hilton, *Ph.D. Thesis, Brigham Young University* **2011.**

[29] Moss, M. L. & Mellon, M. G. Colorimetric Determination of Iron with 2,2'-Bipyridyl and with 2,2',2'-Terpyridyl. *Ind. Eng. Chem. Anal. Ed.* **14,** 862–865 (1942).

[30] Lowry, O. H., Rosebrough, N. J., Farr, A. L. & Randall, R. J. Protein measurement with the Folin phenol reagent. *J biol Chem* **193,** 265–275 (1951).

[31] Hilton, R., David Andros, N. & Watt, R. The ferroxidase center is essential for ferritin iron loading in the presence of phosphate and minimizes side reactions that form Fe(III)-phosphate colloids. *Biometals* **25,** 259–273 (2012).

[32] Johnson, J. L., Cannon, M., Watt, R. K., Frankel, R. B. & Watt, G. D. Forming the Phosphate Layer in Reconstituted Horse Spleen Ferritin and the Role of Phosphate in Promoting Core Surface Redox Reactions†. *Biochemistry* **38,** 6706–6713 (1999).

---

[34] Smith, Trevor J., Stephen D. Erickson, Catalina Matias Orozco, Andrew Fluckiger, Lance M. Moses, John S. Colton, and Richard K. Watt. Tuning the band gap of ferritin nanoparticles by co-depositing iron with halides or oxo-anions. *J. Mater. Chem. A* **2,** 20782–20788 (2014).

Chapter 5 – Non-native Co-, Mn-, and Ti-Oxyhydroxide Nanocrystals in Ferritin for High Efficiency Solar Energy Conversion

This chapter is a summary of the paper that was published in Nanotechnology, issue 26, pp. 15703, 2015, and is titled "Non-native Co-, Mn-, and Ti-oxyhydroxide Nanocrystals in Ferritin for High Efficiency Solar Energy Conversion."

In this chapter I performed the majority of the experiments, including non-native metal oxide and reconstituted ferrihydrite mineral synthesis and characterization. Stephen Erickson is the first author of the paper and wrote the initial draft of the paper. Stephen Erickson also performed the band gap measurements and preformed the calculations for a maximally efficient solar cell. I assisted in writing and editing sections of the paper. Dr. John Colton and Dr. Richard Watt also assisted in the editing of this publication.

Overview

Photovoltaic solar cells are striving to reach their maximal photon to electron conversion efficiencies. Interplay between minimizing the energy lost from photons of excess energy while maximizing the number of photons that can be absorbed led Shockley and Queisser to calculate the maximum efficiency for a single material to be 33.7% for a semiconductor with a band gap of 1.34 eV.[1] The 33.7% conversion efficiency limit can be exceed by using multi-junction solar cells, which hace a maximal efficiency of 86% for an infinite number of different materials, and 49% for a more realistic three layers of different materials.[2] Concentrating sunlight can also increase the efficiency of a material up to 40% for a single material and 63% for three different materials.[1] While these efficiencies have maximized for selective light harvesting, producing multi-junction solar cells is complicated at best.

Currently, InGaP multi-junction solar cells consist of three layers: InGaP, InGaAs, and Ge. Within each of the layers there are sub-layers of windows, anti-reflective coatings, tunnel junctions, and other materials for the purposes of efficiently generating and syphoning electron-hole pairs. All three of these materials must have the same crystal lattice, similar working potentials and similar working currents in order to perform properly in tandem. Additions of a 4th layer to increase efficiency with the same crystal lattice, voltage matching, and current matching would be difficult.[3] If the need for crystal lattice matching could be removed, multi-junction solar cells would be far easier to synthesize and develop.

Ferritin provides a unique model for multi-junction photovoltaic devices. It is a sphere-like bio-inorganic molecule that measures 12 nm in diameter with an 8 nm hollow interior. It is capable of storing Ti, Cr, Mn, Fe, Co, and Ni oxo-hydroxide nanoparticles within the protein interior. The protein shell is stable between pH 4-10 and can withstand temperatures up to 85 °C.

The protein shell is also able to maintain the solubility of the metal-oxide nanoparticles in solution and can regenerate the metal-oxide nanoparticles in the event of photocorrosion. The ferritin protein shell is also electrically conductive.[4] The ferritin molecules, with various metal-oxide nanoparticles, can be layered onto one another without the need crystal lattice matching.[5] These properties are ideal for modeling a multi-junction photovoltaic device.

Rakshit et al. measured the band gaps of apoferritin, Mn, Fe, Co, and Cu ferritins using scanning tunneling spectroscopy (STS), reporting band gaps of 1.47 eV, 1.17 eV, 1.00 eV, 0.90 eV, and 0.00 eV.[6] However, in a recent paper from our group by Colton et al.[7] we show that the STS technique is improper for measuring band gaps, and note the discrepancy between the STS experimental results for the ferrihydrite mineral in ferritin (1.00 eV) and both optical filter colorimetric assays (2.5-3.5 eV[8] and 3.0-3.5 eV[9]) and optical absorption spectroscopy (OAS) band gap measurements (3.01 eV for a direct transition and 2.14 eV for an indirect band gap[7]) for the same mineral. Additionally, no known band gap measurements for titanium oxide cores in ferritin have previously been reported.

The purpose of the publication was to measure the band gaps of Ti, Mn, and Co ferritins using OAS and use these results to model maximal efficiency for a ferritin based multi-junction photovoltaic system. My contribution to this paper was the synthesis and characterization of the various non-native metal ferritin samples, where Stephen Erickson performed the band gap measurements and efficiency calculations for the photovoltaic solar cell.

Experimental

Apoferritin, titanium-, manganese-, iron-, and cobalt-ferritin were all synthesized for the purpose of measuring their band gaps to both investigate current literature values and calculate a maximally efficient multi-junction photovoltaic solar cell.

Apoferritin was synthesized using established dialysis methods. Native ferritin was dialyzed against mercaptoacetic acid using a Millipore 10 kDa dialysis cassette to remove iron from ferritin. The resulting apoferritin was then dialyzed against a 0.10% salt free bicarbonate buffer. The resulting protein concentration was measured using a modified Lowry assay.

Titanium oxo-hydroxide (Ti(O)OH) cores were synthesized using modifications to the original method by Klem et al.[10] Three milligrams of apoferritin were added to a buffer solution, containing 300 mM NaCl and 150 mM MES buffer at pH 6.0. A solution of 12.5 mM Ti^{IV}-citrate was then added to the buffered ferritin solution after reaching 60°C using a temperature bath, targeting core sizes of 500, 1000, and 1500 Ti per ferritin. The final volume of the reaction was 2.0 mL inside a UV-Vis cuvette with stirring. The sample was then illuminated with a 150 W Oriel Xe lamp to photocatalyze the titanium loading into apoferritin. A 1 cm water path was used as an infrared filter to remove excess heat from the lamp.

Mn(O)OH cores were synthesized by following established methods.[11,12] A solution of $MnCl_2$ was added to a 50 mM AMPSO buffered solution at pH 8.9 with 5 mg of apoferritin to form the manganese cores. $MnCl_2$ was added to target core sizes of 500, 1000, and 1500 Mn/ferritin at a rate of 100 metal atoms per ferritin per addition every 10 minutes. The pH of the solution was also maintained by addition of 300 mM NaOH.

Reconstituted ferrihydrite minerals were synthesized using established methods. Ferrous ammonium sulfate was added to a 50 mM pH 7.4 imidazole and apoferritin solution at a rate no greater than 100 irons per ferritin per 10 minutes, targeting a core size of 1500 irons per ferritin. pH was maintained at pH 7.4 by additions of 300mM NaOH.

Co(O)OH cores were synthesized by following established methods,[13] where $Co(NO_3)_2$ and H_2O_2 were periodically added to 5 mg of apoferritin solution at pH 5.4, unbuffered. The amount added was adjusted to target a range of core sizes at a rate of 100 metal atoms per ferritin per addition every 10 minutes. The pH of the solution was maintained by addition of 10 mM NaOH.

All samples were then passed over a Sephadex G-75 size exclusion column to remove unbound ions from ferritin.

Protein analysis was performed using a modified Lowry assay.[14] Metal analysis was performed using inductively coupled plasma – mass spectrometry (ICP-MS) with a standard calibration curve. The molar ratio between the metal and protein concentrations gave the resulting metals per ferritin ratios from the metal synthesis.

The successful synthesis of the non-native metals in ferritin was confirmed using tunneling electron microscopy (TEM) with a uranyl acetate negative protein stain. This allowed the ferritin protein shells and metal-oxide cores to be imaged using bright field imaging techniques.

For a detailed explanation for the OAS technique and maximal efficiency calculations please see the original publication from our group by Erickson et al.[15]

Results and Discussion

The synthesis of the non-native metal oxide cores in ferritin was confirmed using TEM as is shown in Figure 5-1. Using bright field imaging techniques, the images shown in Figure 5-1 show a dark contrast from the heavy uranium metals used in the negative stain and the metals in the metal-oxide core. Light elements, such as those that comprise the protein, appear as a lighter contrast in the image. Ferritin proteins with metal cores often resemble egg yolks or doughnuts. Figure 5-1 shown from left to right Co(O)OH, Mn(O)OH, and Ti(O)OH minerals inside the protein shell. In the case of Figure 5-1(c), does not produce significant contrast inside the protein like Co and Mn because titanium is a lighter element.

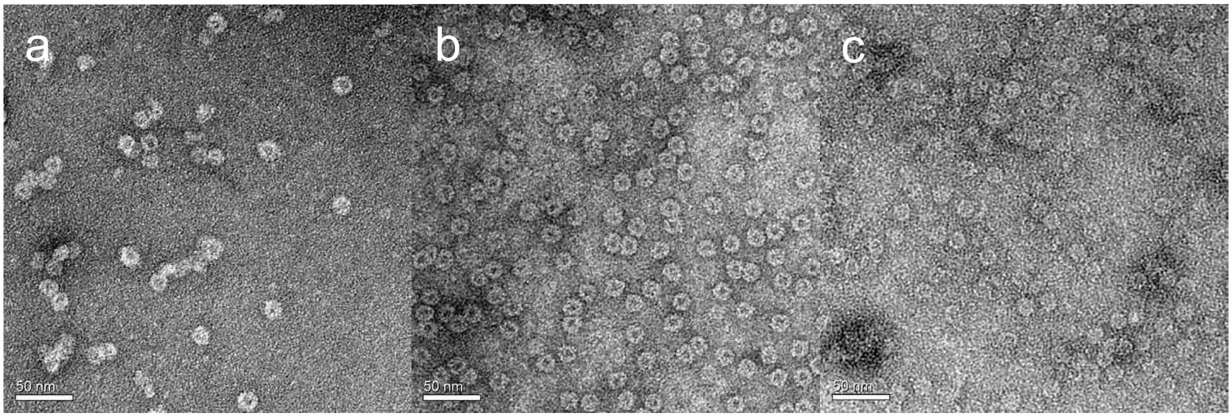

Figure 5 - 1. Representative TEM images of ferritin protein (lighter shell) with synthesized encapsulated nanocrystals (darker core) of (a) Co(O)OH, (b) Mn(O)OH, and (c) Ti(O)OH.

The band gap measurements for Co(O)OH, Mn(O)OH, and Ti(O)OH minerals are shown in Figure 5-2. The three non-native metals as well as the ferrihydrite mineral were determined to be indirect band gap semiconductors that also contain a direct transition. The indirect band gaps for the largest cores were 1.93 eV, 1.60 eV, and 2.19 eV, respectively. The discrepancy between these calculations and those from the STS experiments for Co (0.90 eV) and Mn (1.17 eV) ferritins[6] are evident. Additionally, band gap measurements for the titanium oxide core in ferritin have not yet been reported. The direct transition energies for the largest Co(O)OH, Mn(O)OH, and Ti(O)OH minerals were measured to be 2.6 eV, 2.8 eV, and 3.8 eV, respectively. However, the proximity of the titanium ferritin's direct transition at 3.8 eV and apoferritin's direct transition at 4.0 eV made it difficult to accurately decouple the direct transition in the case of Ti(O)OH ferritin. As such, the direct transition of titanium ferritin is approximated to be 3.8 eV, and specific energies for the various core sizes are not reported.

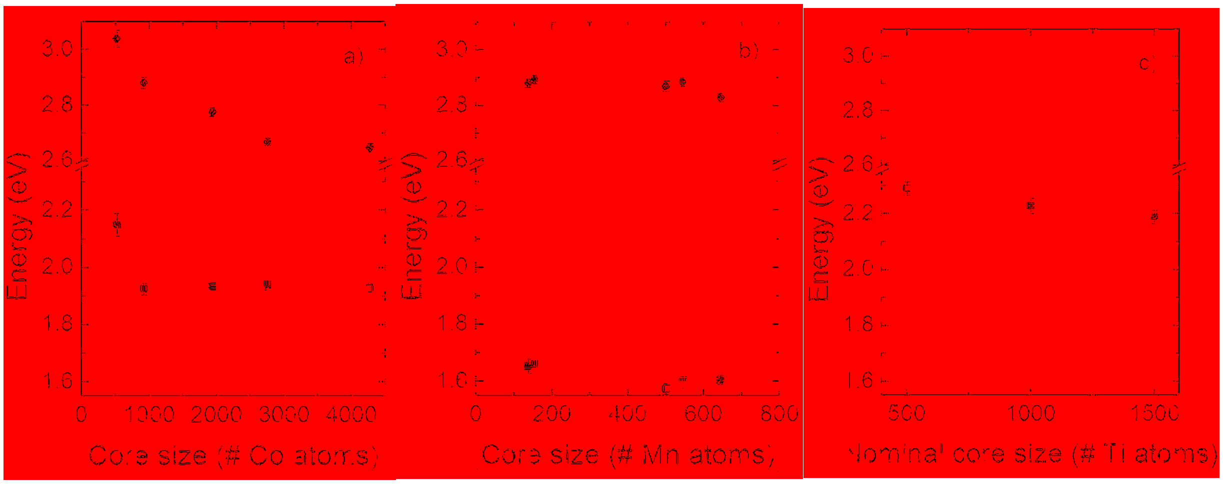

Figure 5 - 2. Band gap measurements of (a) Co(O)OH, (b) Mn(O)OH, and (c) Ti(O)OH nanocrystals plotted against core size. Squares show indirect gaps and circles show direct gaps.

Quantum confinement effects were observed similar to what was observed in the ferrihydrite mineral by our group in a paper by Colton et al.[7] In the case of cobalt ferritin, a "bulk-like" state is observed for cores that were larger than 1000 Co/ferritin, where increasing the number of cobalt atoms in the ferritin protein does not significantly alter the band gap of the mineral. A similar "bulk-like" state was observed in the case of ferrihydrite minerals above 900 irons per ferritin.[16]

The indirect band gap energies from the Co(O)OH, Mn(O)OH, Ti(O)OH, and Fe(O)OH minerals in ferritin were used to calculate the maximal efficiency of a ferritin based solar cell using the AM1.5G solar spectrum. Additional considerations for a silicon base layer were also included in the calculations, which significantly improved the resulting efficiency from 38.0% to 51.3%. These results are illustrated in Figure 5-3. Details as to the equations and resulting calculations are available in the original paper from our group by Erickson et al.[15] Tabulated results are shown in Table 5-1. These calculations include concentrating the light from the AM1.5G spectrum to 1, 100, and maximal light concentration. The calculations both include and exclude the silicon base layer, and calculations for matching the current-voltage performance and efficiency are also available in the paper from our group by Erickson et al.[15]

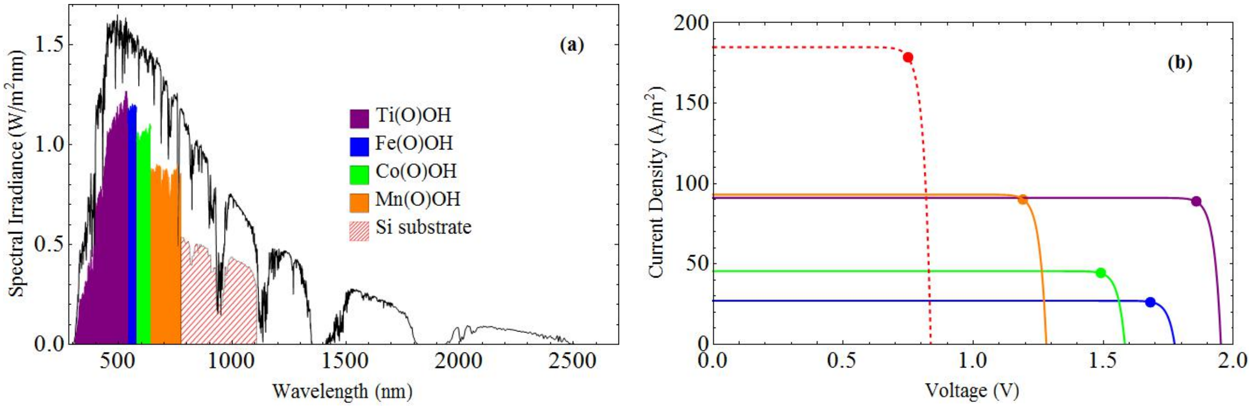

Figure 5 - 3. Visual representation of the theoretical maximum efficiency for a ferritin-based multi-junction solar cell under normal sunlight found by maximizing equation 9. (See reference 15) The black curve shows the AM1.5G spectrum. Different colors (shades) represent different regions of the AM1.5G spectrum absorbed by the different layers of material. Influence of a silicon-like bottom layer (labeled "silicon substrate") on upper layers is small, so the colored (shaded) regions for the upper four layers are accurate for both including and excluding the silicon-like layer. From left to right the materials are Ti(O)OH, Fe(O)OH, Co(O)OH, Mn(O)OH, and silicon. (b) I-V characteristic curves with colors (shades) corresponding to part a. Large dots show the maximum power points,

indicating the operating voltages necessary to obtain maximum efficiency. The curves follow the reverse order from part a.

Table 5 - 1. Summary of the efficiency calculation results. The first three rows involve using only the ferritin-based metal oxyhydroxide nanoparticles whose band gaps we have measured. The next three rows involve using either silicon or nanoparticle with a silicon-like band gap (such as PbS) as an additional bottom layer. The next three rows similarly involve a silicon-like bottom layer, but in a current matching configuration in which the voltages combine.

	f_{Ω}(# suns)	*Operating voltages (V)*	*Theoretical efficiency (%)*
Ti,Fe,Co,Mn	1	1.856,1.680,1.490,1.181	38.0
	100	1.974,1.798,1.607,1.298	41.0
	Max	2.130,1.954,1.764,1.453	44.9
Ti,Fe,Co,Mn,Si	1	1.856,1.680,1.490,1.191,0.748	51.3
	100	1.974,1.798,1.608,1.308,0.864	56.4
	Max	2.130,1.954,1.764,1.464,1.012	63.1
Ti, Co, Mn, Si	1	1.905,1.505,1.251,0.825 (5.49 total)	41.6
(current matched)	100	2.024,1.622,1.370,0.944 (5.96 total)	45.2
	Max	2.182,1.778,1.527,1.103 (6.59 total)	50.0

Conclusion

Syntheses of Ti, Mn, Fe, and Co ferritins were successful and confirmed using size exclusion gel chromatography and TEM analysis. A variety of core sizes for the non-native metal cores were synthesized and characterized. Each metal core was able to give variations to the band gap energies based on quantum confinement effects. The resulting efficiency calculations show that a ferritin based photovoltaic system using cobalt, iron, manganese, and titanium cores can reach a maximal 38% efficiency under normal solar illumination and can be increased to 51.3% efficiency using a silicon base layer.

References

---

[1] Shockley, W. & Queisser, H. J. Detailed Balance Limit of Efficiency of p-n Junction Solar Cells. *Journal of Applied Physics* **32,** 510–519 (1961).

[2] R. King, D. Law, K. Edmondson, C. Fetzer, G. Kinsey,H. Yoon, R. Sherif, N. Karam. 40% efficient metamorphic GaInP/GaInAs/Ge multijunction solar cells. *Applied physics letters* **90,** 183516–183900 (2007).

[3] Yamaguchi, M. III–V compound multi-junction solar cells: present and future. *Solar energy materials and solar cells* **75,** 261–269 (2003).

[4] Xu, D., Watt, G. D., Harb, J. N. & Davis, R. C. Electrical conductivity of ferritin proteins by conductive AFM. *Nano letters* **5,** 571–577 (2005).

[5] Chu, Sang-Hyon, Sang H. Choi, Gerald D. Watt, Jae-Woo Kim, Yeonjoon Park, Robert C. Davis, John N. Harb, Glen C. King, and Peter T. Lillehei. Fabrication of cell structures for bionanobattery. *Smart Struct. Mat.* **5389**, 443–451 (2004).

[6] Rakshit, T. & Mukhopadhyay, R. Tuning Band Gap of Holoferritin by Metal Core Reconstitution with Cu, Co, and Mn. *Langmuir* **27,** 9681–9686 (2011).

[7] Colton, J., Erickson, S., Smith, T. & Watt, R. Sensitive detection of surface- and size-dependent direct and indirect band gap transitions in ferritin. *Nanotechnology* **25,** 135703 (2014).

[8] Kim, Hye-Jin, Hyang-Mi Kim, Ji-Hye Kim, Kyeong-Seon Ryu, Seung-Moon Park, Kwang-Yeup Jahng, Moon-Sik Yang, and Dae-Hyuk Kim. Expression of Heteropolymeric Ferritin Improves Iron Storage in Saccharomyces cerevisiae. *Applied and Environmental Microbiology* **69,** 1999–2005 (2003).

[9] Keyes, J., Hilton, R., Farrer, J. & Watt, R. Ferritin as a photocatalyst and scaffold for gold nanoparticle synthesis. *J Nanopart Res* **13,** 2563–2575 (2011).

[10] Klem, M. T., Mosolf, J., Young, M. & Douglas, T. Photochemical Mineralization of Europium, Titanium, and Iron Oxyhydroxide Nanoparticles in the Ferritin Protein Cage. Inorg. Chem. **47,** 2237–2239 (2008).

[11] Meldrum, F. C., Wade, V. J., Nimmo, D. L., Heywood, B. R. & Mann, S. Synthesis of inorganic nanophase materials in supramolecular protein cages. *Nature* **349,** 684–687 (1991).

[12] Mackle, P., Charnock, J. M., Garner, C. D., Meldrum, F. C. & Mann, S. Characterization of the manganese core of reconstituted ferritin by x-ray absorption spectroscopy. *J. Am. Chem. Soc.* **115,** 8471–8472 (1993).

---

[13] Douglas, T. & Stark, V. T. Nanophase Cobalt Oxyhydroxide Mineral Synthesized within the Protein Cage of Ferritin. *Inorg. Chem.* **39,** 1828–1830 (2000).

[14] Peterson, G. L. A simplification of the protein assay method of Lowry et al. which is more generally applicable. *Analytical Biochemistry* **83,** 346–356 (1977).

[15] Erickson, S. D., Smith, T. J., Moses, L. M., Watt, R. K. & Colton, J. S. Non-native Co-, Mn-, and Ti-oxyhydroxide nanocrystals in ferritin for high efficiency solar energy conversion. *Nanotechnology* **26,** 015703 (2015).

[16] Smith, Trevor J., Stephen D. Erickson, Catalina Matias Orozco, Andrew Fluckiger, Lance M. Moses, John S. Colton, and Richard K. Watt. Tuning the band gap of ferritin nanoparticles by co-depositing iron with halides or oxo-anions. *J. Mater. Chem. A* **2,** 20782–20788 (2014).

Chapter 6 – Practical Demonstration of Titanium Ferritin's Photo-Catalytic Ability

This paper has been prepaired for RCS Advances and will be submitted in the near future. I am the first author of this paper, and performed most of the research and writing with assistance from Jacob Embley and Cameron Olsen. I also received editing assistance from Dr. John Colton and Dr. Richard Watt.

Abstract

Titanium oxo-hydroxide cores in ferritin were used to photocatalytically reduce gold ions into gold nanoparticles. The size of the resulting nanoparticles was dependent on the intensity of UV light used to photocatalyze the reduction. High intensity UV light created 3.9 ± 1.0 nm nanoparticles whereas low intensity light formed a bimodal distribution of nanoparticles of 16 ± 3 nm and 50 nm ± 8 nm nanoparticles.

Introduction

The synthesis and characterization of nanoparticles (NPs) is a rapidly growing area of research. NPs have unique physical and photochemical properties that are different from their bulk material counterparts. Controlling the size, shape, and morphology of the nanoparticles can alter their physical and photochemical properties. Gold nanoparticles (AuNPs) have unique catalytic and optical properties, including surface plasmon resonance signals (SPR) which are size and shape dependent.[1] These AuNPs have applications in medicine[2,3] and as biosensors.[4,5] Consequently the synthesis and stabilization of gold nanoparticles is of great interest. Several studies have used ferritin to create these AuNPs in a size-controlled manner.[6,7] This study focuses on using a new photocatalytic material in ferritin to produce AuNPs.

Ferritin is a sphere-like biomolecule that is found in virtually all organisms and was first discovered by Vilem Laufberger.[8] The primary role of ferritin is to store iron as a ferrihydrite mineral, $(Fe^{III})_2O_3 \cdot 0.5H_2O$ (referred to as Fe(O)OH for convenience). The protein measures 12 nm in diameter with an 8 nm hollow interior and has channels along the 3-fold axis in the 24-mer protein that allows metal ions to traverse the 2 nm thick protein shell. Each subunit is either a heavy (21 kDa) or light (19 kDa) chain commonly referred to as H- and L-ferritin. Each chain has a specific role in the ferritin macromolecule; H-ferritin contains a ferroxidase center where metal ions are oxidized from their 2^+ to 3^+ state.[9] L-ferritin possesses the nucleation site that allows metal ions to bind and form the metal mineral inside ferritin. L-ferritin was also recently shown to contain an important electron transport chain, which facilitates electron import and export for iron loading and demineralization, respectively.[10]

Ferritin has been shown to form various metals[11], metal oxides[12,13,14,15,16], metal sulfides[17], and II-VI[18] semiconductor materials. Our group previously demonstrated that transition metal-oxides are indirect band gap semiconductors that also have a direct transition.[19,20,21] This work included titanium oxo-hydroxide cored ferritin (referred to as Ti-FTN for convenience), which were shown to have an indirect band gap between 2.19 and 2.29 eV with a direct transition at approximately 3.8 eV. In this study, we test Ti-FTN as a photocatalyst to photoreduce gold ions in solution.

Ferrihydrite cores in ferritin (Fe-FTN) have previously been shown to photo-reduce Au(III) to Au(0)[6], Cr(IV) to Cr(III)[22], and Cu(II) to Cu(0)[23]**.** The proposed mechanism with the native mineral suggests that UV light is used to generate an electron-hole pair inside the ferrihydrite mineral.[6,7] This electron-hole pair is sufficiently long lived to allow the excited electron to reduce various species in solution. The remaining hole is filled by citrate oxidation, and the process repeats (Figure 6-1). This study demonstrates a functional photocatalytically driven electron transfer reactions by the titanium cores inside ferritin.

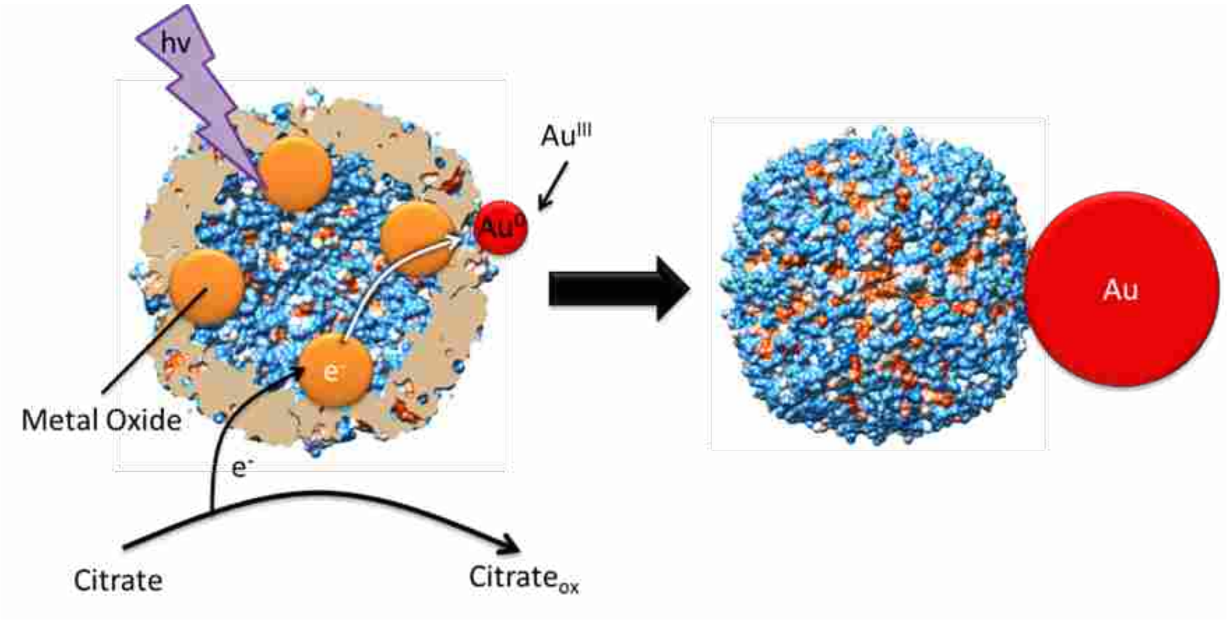

Figure 6 - 1. AuNP synthesis scheme using titanium oxo-hydroxide nanoparticles in ferritin. UV light creates an electron-hole pair, and excited electrons are used to reduce Au(III) ions to Au(0) NPs on the exterior of ferritin. The hole is filled by electrons extracted from citrate, which acts as a sacrificial electron donor.

Materials and Methods

Native horse spleen ferritin was purchased from Sigma Aldrich. Apoferritin was prepared using established methods from M. Joo et al.[24] and J. Polanams et al.[25] using a Milipore 10 kDa molecular weight cut off dialysis cartridge against thioglycolic acid. The finished apoferritin was buffered against a 0.1% bicarbonate buffer. Protein concentration was determined using a modified Lowry[26] by G.L. Peterson[27].

Titanium oxo-hydroxide (Ti(O)OH) cores were made using the method from Erickson et al.[20] which is a modification of the Klem et al.[28] method. Three milligrams of apoferritin were added to a buffer solution, containing 300 mM NaCl and 150 mM MES buffer at pH 6.0. A solution of 12.5 mM Ti^{IV}-citrate was also added to the buffered ferritin solution after reaching 60°C using a temperature bath, targeting a core size of 1500 Ti per ferritin. The final volume of the reaction was 2.0 mL inside a UV-Vis cuvette. The sample was then illuminated with a 150 W Oriel Xe lamp to photocatalyze the titanium loading into apoferritin. A 1 cm water path infrared filter was used to remove excess heat from the lamp. After the Ti-FTN core was synthesized, the sample was passed over a 12.5 cm x 1.0 cm Sephadex G-75 column to separate the ferritin sample from unbound ions. The column was equilibrated with a salt free imidazole buffer, pH 7.4.

Reconstituted ferrihydrite minerals were created following the method from Smith et al.[21] with 300 mM NaCl present during iron loading.

Protein concentrations were determined by the modified Lowry method[27], and metal concentrations were determined by using inductively coupled plasma mass spectrometry (ICP-MS). The ratio of the two concentrations gives the metal/ferritin ratio for the titanium and iron cores.

AuNP formation was measured using established methods from Keyes et al.[6] using an HP 8453 spectrophotometer measuring 530 nm over time. 40 μL of 10 mM Au(III) were placed into a ferritin solution containing 32 mM Citrate, 20 mM TRIS pH 7.4, and 125 mM NaCl, with a final volume of 1.5 mL. Protein concentrations were maintained at 0.15 mg/mL, including both reconstituted Fe-FTN and Ti-FTN. After a 30 second baseline was collected, a Sun Ray 400 UV floodlight (1.26 W/cm^2) was used to illuminate the sample for several minutes until the absorbance at 530 nm plateaued signifying that the Au(III) ions were mostly consumed and converted into AuNPs. The UV lamp on the spectrophotometer (1.5 mW/cm^2) was also used to produce AuNPs using Ti-FTN.

Scanning tunnelling electron microscope (STEM) grids were prepared using the method from Smith et al.[29] STEM images were captured and energy-dispersive X-ray spectroscopy (EDX) analyses performed using a Technai-TF20 tunnelling electron microscope. Uranyl acetate was used as a negative stain to enhance protein contrast.

Results and Discussion

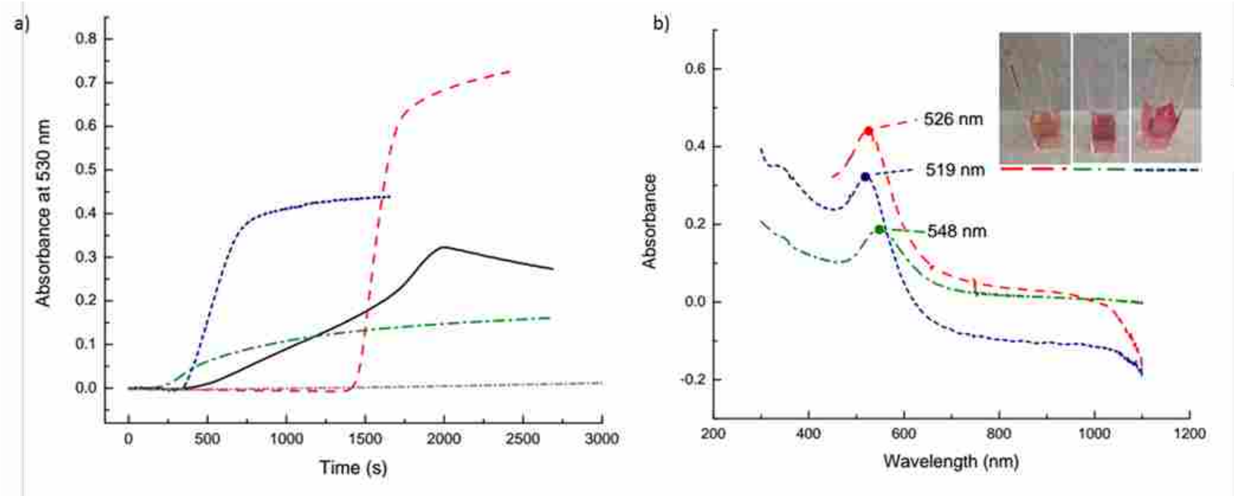

Figure 6 - 2. AuNP formation kinetic trace measured at 530 with final absorbance spectra. (a) Gold nanoparticle formation using Fe-FTN or Ti-FTN cores. The Fe-FTN control is in red (long dash), The gold only control is in black. There are three separate kinetic traces for the Ti-FTN. Illumination with intense light is shown in dark blue (short dash), illumination by low intensity UV light is shown in green (— - —), and the control without UV light is shown in gray (-··-). (b) Shows the SPR peak of the gold nanoparticles after 20 minutes of illumination. The inset photos are of the AuNPs formed from, left to right: Fe-FTN (red, long dash), Ti-FTN low light (green, — - —), and Ti-FTN intense light (dark blue, short dash). The respective lines and colours of the various samples are shown below the photo.

The photocatalytic reduction of Au(III) ions to AuNPs are monitored by measuring the SPR signal at 530 nm. Reactions using the low intensity UV light from the spectrophotometer as well as the intense UV light from the UV flood lamp were able to reduce gold ions using the titanium ferritin. The low intensity UV light sample created a wide range of gold nanoparticle sizes between 10 and 60 nm. The high intensity UV light created gold nanoparticles similar to what has been observed in the reconstituted Fe-FTN control but with slightly smaller NPs with diameters of less than 10 nm.

Kinetic Traces

The reconstituted Fe-FTN (1400 Fe/FTN) was used as a positive control reaction with conditions that were similar to Keyes et al, with the exception of the UV light source which alters the rate of AuNP formation.[6] In this control no change in absorbance was observed for the first 1400 seconds (compared to 750 seconds for the Keyes et al. method) until the AuNPs grow larger than 2 nm in diameter at which point the approximate 530 nm surface SPR peak is observed (Figure 6-2(a)). The plateau in Figure 6-2(b) occurred as the Au(III) ions were depleted, which decreased the rate of gold nanoparticle formation. The Fe-FTN mineral was reconstituted in order to closely match the size of the titanium cores (1250 Ti/FTN), and allow for a better comparison between the different materials with the protein concentrations held constant.

Reactions performed with Ti-FTN (1250 Ti/FTN) under the same intense UV light as Fe-FTN produced absorbance at 530 nm, much sooner than the Fe-FTN control (300 seconds vs. 1400 seconds, respectively). This faster AuNP formation suggests that Ti-FTN is more photoactive than Fe-FTN.

In a control reaction, the titanium cores inside ferritin were thought to chemically reduce the Au(III) ions to AuNPs when citrate was present in solution and the intense UV light remained off. However, upon further investigation the low intensity UV lamp of the spectrophotometer was on and was sufficient to cause charge separations in the titanium cores and form AuNPs (Fig 2a). Similar reactions using the UV lamp from the spectrophotometer with Fe-FTN cores failed to produce AuNPs, which indicates better reactivity from the Ti-ferritin samples than the Fe-ferritin samples.

The Ti-FTN sample with the low intensity UV light formed AuNPs after 200 seconds of illumination, which is 100 seconds faster than the high intensity UV light sample. The lower intensity UV light allows for larger nanoparticles to form sooner because of the slower photocatalytic reaction, whereas the high intensity light forms several smaller AuNPs that take longer to exceed 2 nm. The SPR signal from the low intensity light also has a lower absorbance than the other samples and is discussed later.

Surface Plasmon Resonance Peaks

The Ti-FTN sample prepared under the intense UV lamp had an absorbance of 519 nm. This absorbance peak for the Ti-FTN was blue-shifted from the usual 530 nm SPR produced by the Fe-FTN which forms 5-10 nm AuNPs. This shift suggests that Ti-FTN formed smaller AuNPs (see below) (Figure 6-2(b)). The blue-shift in the SPR signal, as well as the increase in final absorbance, would also suggest that the AuNPs are not only smaller, but are in much greater number compared to the AuNPs formed by the low intensity UV light, which is described in the TEM analysis of the sample.

The low intensity UV light on the titanium sample gave an SPR signal of 548 nm, meaning that the AuNPs were larger than the previously reported 5-10 nm particles observed for Fe-FTN cores.[6] Since the gold and ferritin concentrations were constant across all experiments, this SPR signal would suggest that there are a fewer number of AuNPs with an increased diameter.

A control experiment using only gold and the citrate buffer solution created insoluble AuNPs (Fig 2a). A characteristic of the non-uniform AuNP formation is the low final 530 nm absorbance below 0.4 units, which is followed by a rapid decay of the signal from the AuNP precipitation.

Control experiments were also performed using Fe-FTN with the low intensity light, Ti-FTN without light, and Ti-FTN without light or citrate. These control reactions produce gold nanoparticles consistent with baseline AuNP formation in buffer as described previously.[30,31,32]

TEM Analysis

Figure 6-3 shows the resulting AuNPs formed after UV illumination of Ti-FTN with intense light, which are very small nanoparticles (3.9 ± 1.0 nm). The smaller size is consistent with the 519 nm SPR. EDX analysis confirms the presence of Ti and Au and is shown in the supplemental data section. The high intensity UV illumination of Ti-FTN causes the rapid formation of AuNPs making several small spheres. The coverage density of the AuNPs on the amorphous carbon grid was averaged over a large area and approximated to be 1250 NP/μm^2. The high density of AuNPs caused greater absorption for the high intensity UV light Ti-FTN sample as observed in Figure 6-2(b).

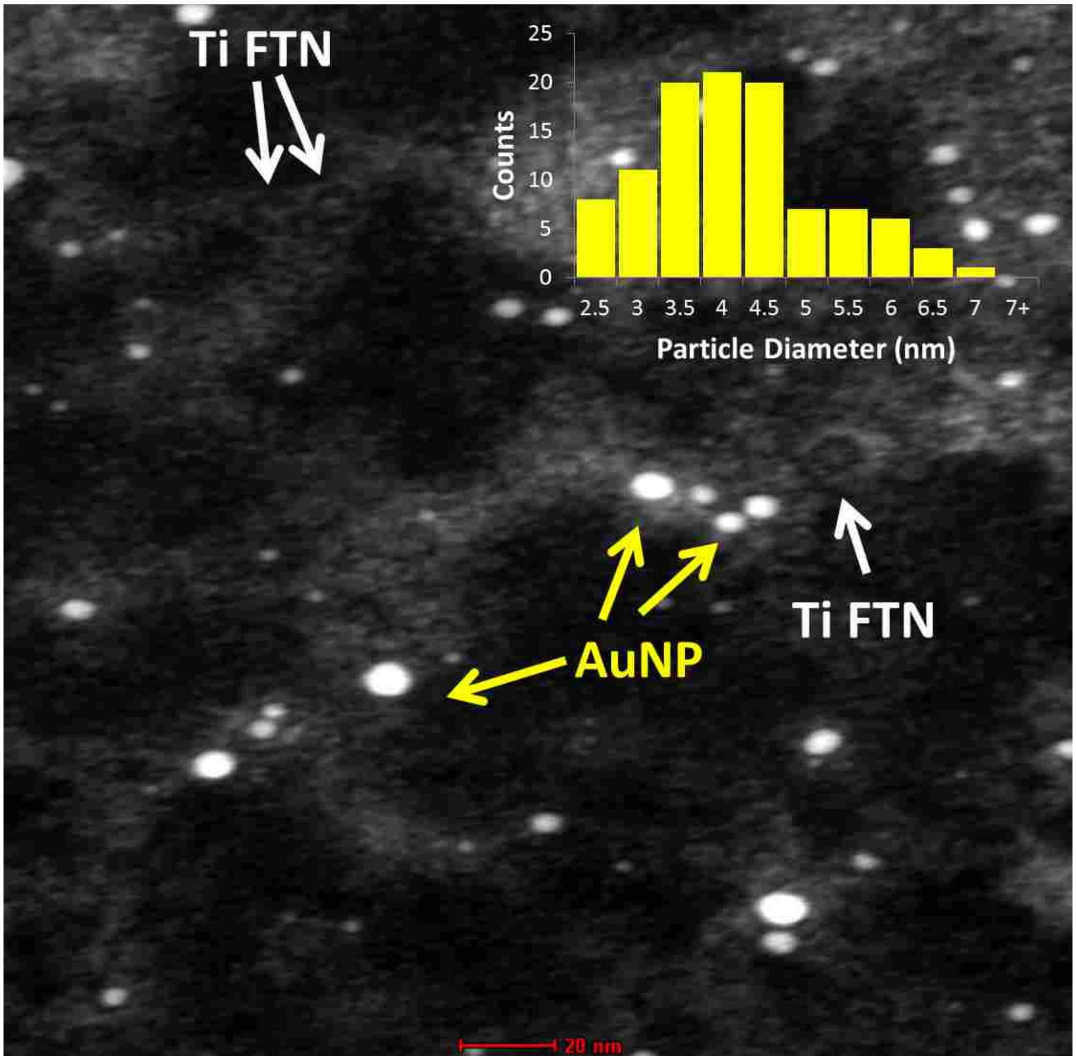

Figure 6 - 3. STEM image of Ti-FTN with Au NPs prepared using the high intensity UV light (20 nm scale bar). An inset histogram shows the size distribution of AuNPs in 0.5 nm increments with a peak average of 3.9 ± 1.0 nm. AuNPs are seen with bright contrast, whereas the ferritins have hollow rings with slight contrast from the Ti.

TEM images from the Ti-FTN with low intensity UV light showed a bimodal distribution of AuNP sizes (Fig. 4), with the AuNPs averaging 16 ± 3 nm and 54 ± 8 nm with an observed density of 5.6 NP/μm^2 on the STEM image (Figure 6-4). This bimodal distribution is most likely caused by the difference in growth rate of each particle; smaller NPs are more commonly observed when using high intensity UV light.[6,7,94]

The larger 56 nm NPs are thought to grow from the slower kinetic rates. Similarly sized AuNPs have been observed under comparable reaction conditions when photoreducing gold ions on a titanium oxide substrate.[33] EDX analysis also confirms the presence of Ti and Au in the sample shown in Figure 6-4 (see supplemental data 6-2). Supplemental Data Figure 6-3 shows a close up of the titanium ferritin samples, which illustrates an absence of AuNPs less than 10 nm.

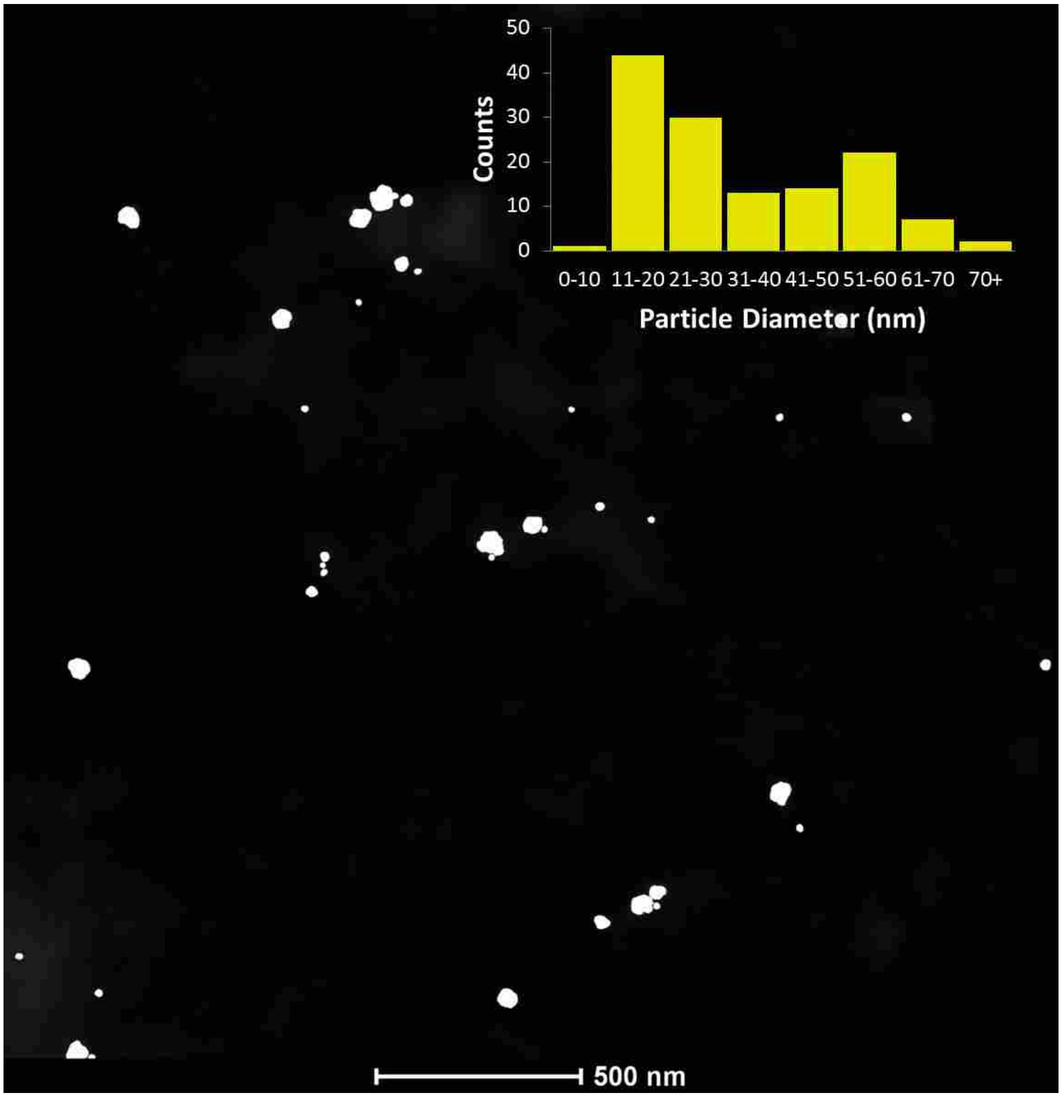

Figure 6 - 4. STEM image of gold nanoparticles formed by illuminating titanium ferritin with low intensity UV light. An inset histogram of the particle size in 10 nm increments shows the bimodal distribution of nanoparticle sizes.

The difference in NP density as well as the difference in the SPR signal peak affects the final absorbance in the 530 nm kinetic trace. When analysing the number of gold atoms and volume of gold nanoparticles deposited on the TEM grids, each sample contained the same number of gold atoms and the same volumetric magnitude of gold nanoparticles (3×10^5

$nm^3Au/\mu m^2$ from high intensity light and $5x10^5$ $nm^3Au/\mu m^2$ from low intensity light, assuming spherical nanoparticles).

Whether or not these AuNPs are in direct contact with ferritin protein shell is difficult to determine. Their observed proximity may be a result of the catalytic nature of the titanium ferritin material, where gold is nucleated on the surface of the protein shell as described previously[6], or the AuNPs may be simply be in close proximity as a result of preparing the TEM grid. Regardless, using high intensity UV light creates small NPs with narrow size distribution, and the low intensity UV light creates a bimodal distribution of larger NPs.

Gold Nanoparticle Analysis

Rapid AuNP formation from the high intensity UV light creates smaller single- or bi-crystalline AuNPs. Slower AuNP formation with lower intensity UV light leads to larger AuNPs with greater polycrystalline character. In all cases the crystal's fine structure shows that the AuNPs are formed from a single NP, rather than several AuNPs coalescing into a single NPs. Additionally, monocrystaline AuNPs are observed with very small AuNPs (<5 nm) and may be the result of insufficient material to allow for polycrystalline AuNPs.

AuNPs are known to have cubic close-packed structure[34], with the {111} planes being the easiest to see on the TEM. Polycrystals are observed when an angle other than 70° is measured between the {111} and {111} planes (shown as colored lines in Figures 6-5, 6-6, and 6-7 when visible under TEM). While other planes may be present in the AuNPs, no other planes were observed within the crystal lattice.

Figure 6-5 shows that the AuNPs from the Ti-FTN reacted with high intensity UV light produced mostly polycrystalline NPs, with the exception of those AuNPs less than 5 nm. The polycrystalline character is most likely caused by the rapid AuNP formation from the high intensity UV light.

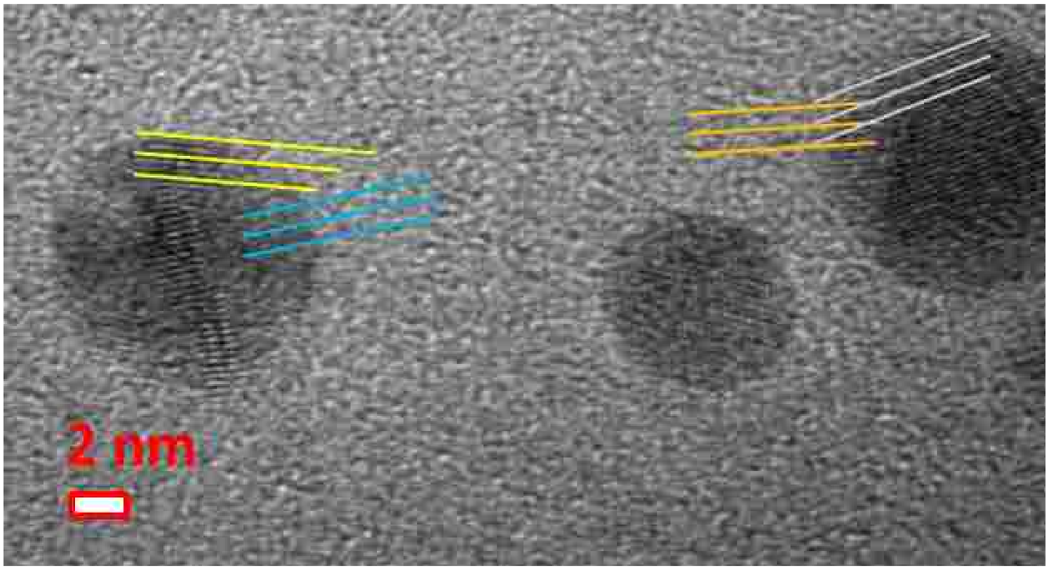

Figure 6 - 5. Polycrystalline AuNPs formed from Ti-FTN with intense UV light. The lattice fringes that are highlighted by yellow and blue lines have a 17° angle and the fringes from the purple and orange lines have a 165° angle. The central AuNP measured a 70° angle between the {111} planes, which suggests a single AuNP.

The low intensity UV light with Ti-FTN created larger polycrystalline AuNPs with significantly more disorder as shown in Figure 6-6. The greater observed disorder in the crystal lattice may be due to slower Au(III) reduction that occurs from the low intensity light, which allows for larger AuNPs and thus a greater chance for defects to form within the crystal.

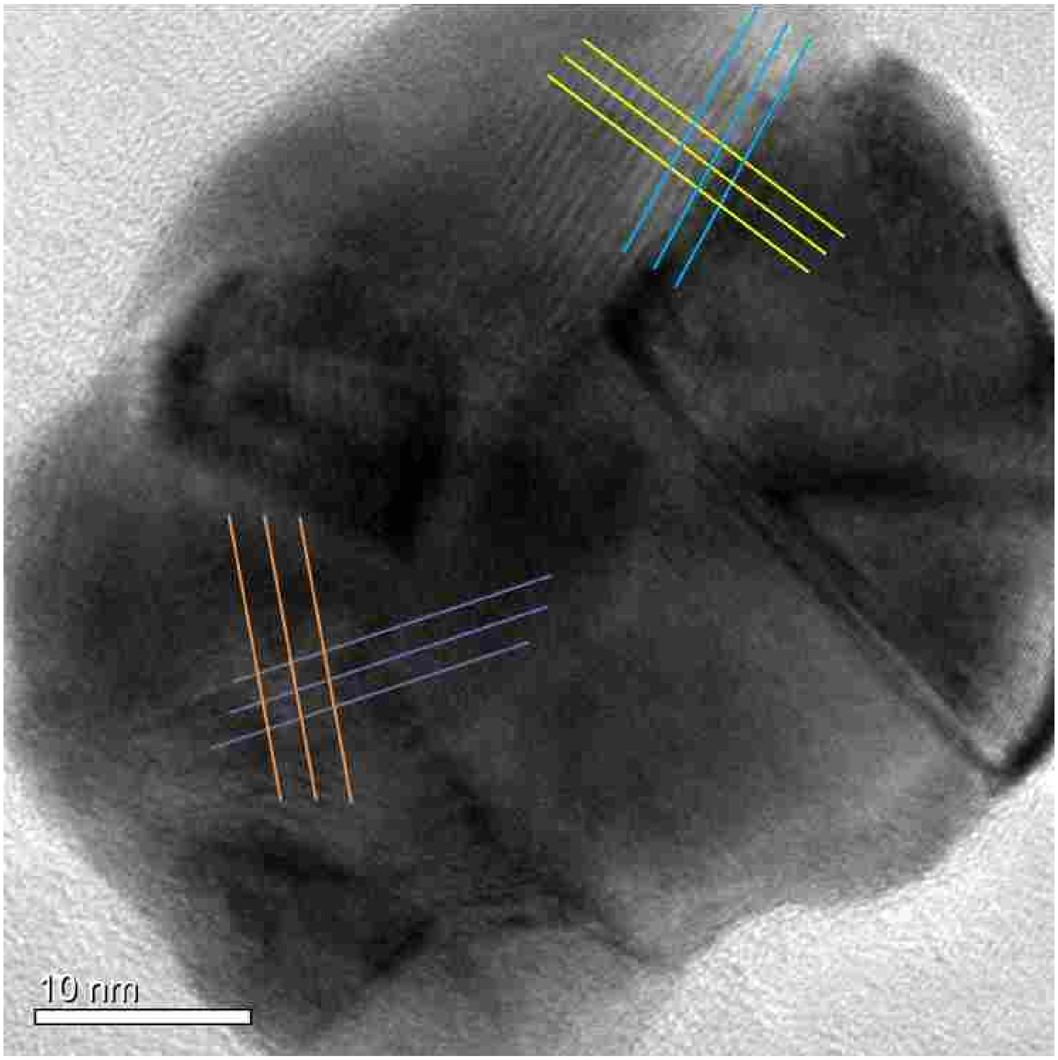

Figure 6 - 6. AuNP formed from Ti-FTN with low intensity UV light. The lattice fringes that are highlighted by the yellow and blue lines create an observed Moire pattern. Fringes from the yellow and blue lines have an 80° angle, and fringes from the purple and orange lines also have an 80° angle.

In contrast, the Fe-FTN's AuNPs formed a mixture of monocrystalline and polycrystalline AuNPs as shown in Figure 6-7 (a) and (b). The greater monocrystallinity may be as a result of both smaller sized AuNPs (7 nm ± 3 nm) and the slower kinetic rate of AuNP formation, which allows for greater organization of the AuNPs.

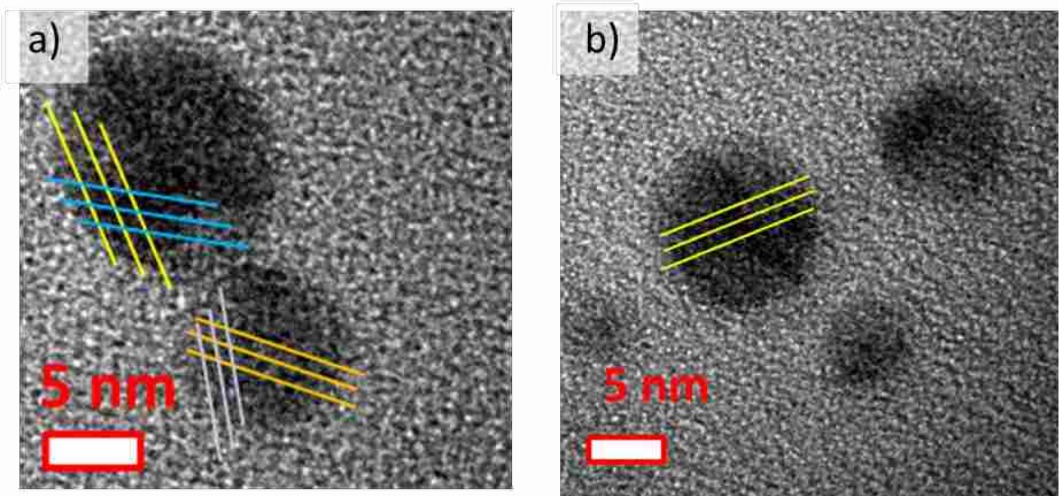

Figure 6 - 7. AuNPs formed by Fe-FTN using intense UV light. a) Polycrystalline AuNPs. The lattice fringes in blue and yellow measure 122° and the orange and purple fringes measure 60°. b) Monocrystalline AuNP with {111} planes.

The high intensity UV light in general created much smaller AuNPs in both the Ti-FTN and Fe-FTN samples. However, the Ti-FTN sample created smaller AuNPs (3.0 ± 1.0 nm) with a greater number of polycrystalline AuNPs and fewer monocrystalline AuNPs than the AuNPs formed by the Fe-FTN counterpart (7 nm ± 3 nm). These results are opposite from what was expected, where larger AuNPs would have a greater degree of defects in the NPs. The difference in crystallinity is attributed to the rate of AuNP formation from the photoactivity of the minerals.

Conclusion

While ferrihydrite cores in ferritin were previously shown to reduce Au(III) to gold nanoparticles[6,7], titanium oxide cores in ferritin have now been demonstrated to photoreduce Au(III) ions into gold nanoparticles. The photochemical reduction process using Ti-FTN is significantly faster, requires less light, and provides a larger range of gold nanoparticle sizes than previously observed for Fe-FTN. The AuNPs from Ti-FTN form either very small nanoparticles (3.9 ± 1.0 nm) in high density (1250 NP/μm^2) using a 1.26 W/cm^2 UV light, or larger particles

(16 ± 3 nm and 54 ± 8 nm) in low density (5.6 NP/μm^2) using a 1.5 mW/cm^2 UV light. Both the Ti-FTN and Fe-FTN cores in ferritin form polycrystalline AuNPs, however the Ti-FTN cores have a greater degree of polycrystallinity than the Fe-FTN sample's AuNPs. These results show that a non-native metal in ferritin has photocatalytic properties and provide plausibility to a ferritin based photovoltaic system.

Supplemental Data

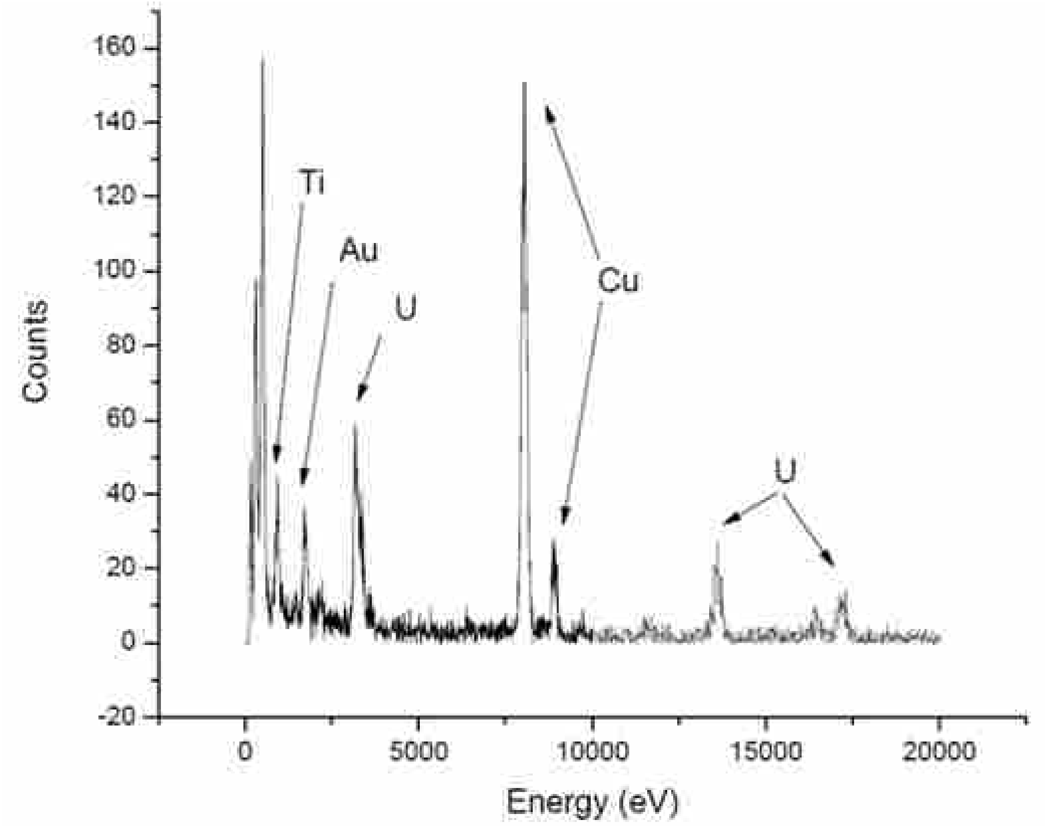

Supplemental Figure 6 - 1. EDX analysis of the AuNPs formed from titanium ferritin using high intensity UV light. Titanium, gold, and uranium are all labelled in the EDX analysis.

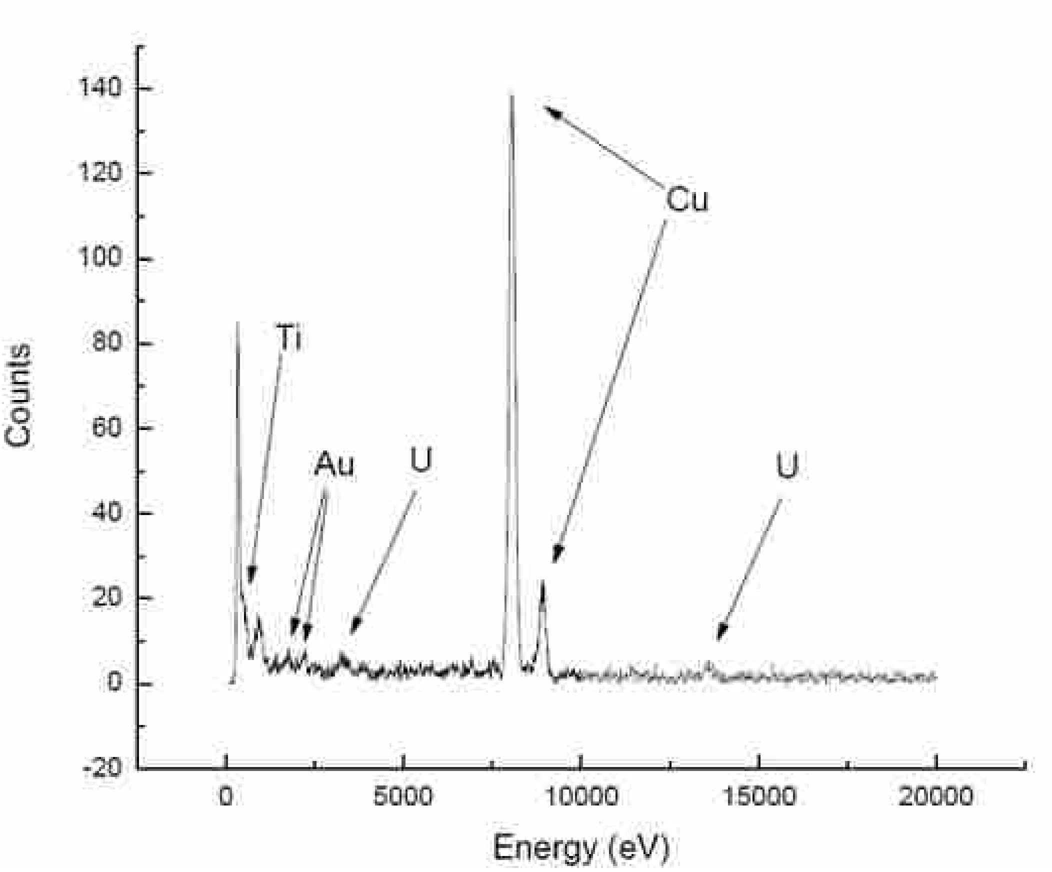

Supplemental Figure 6 - 2. EDX analysis of titanium ferritin and AuNPs formed from low intensity UV light. Titanium, gold, and uranium are all labelled in the EDX analysis.

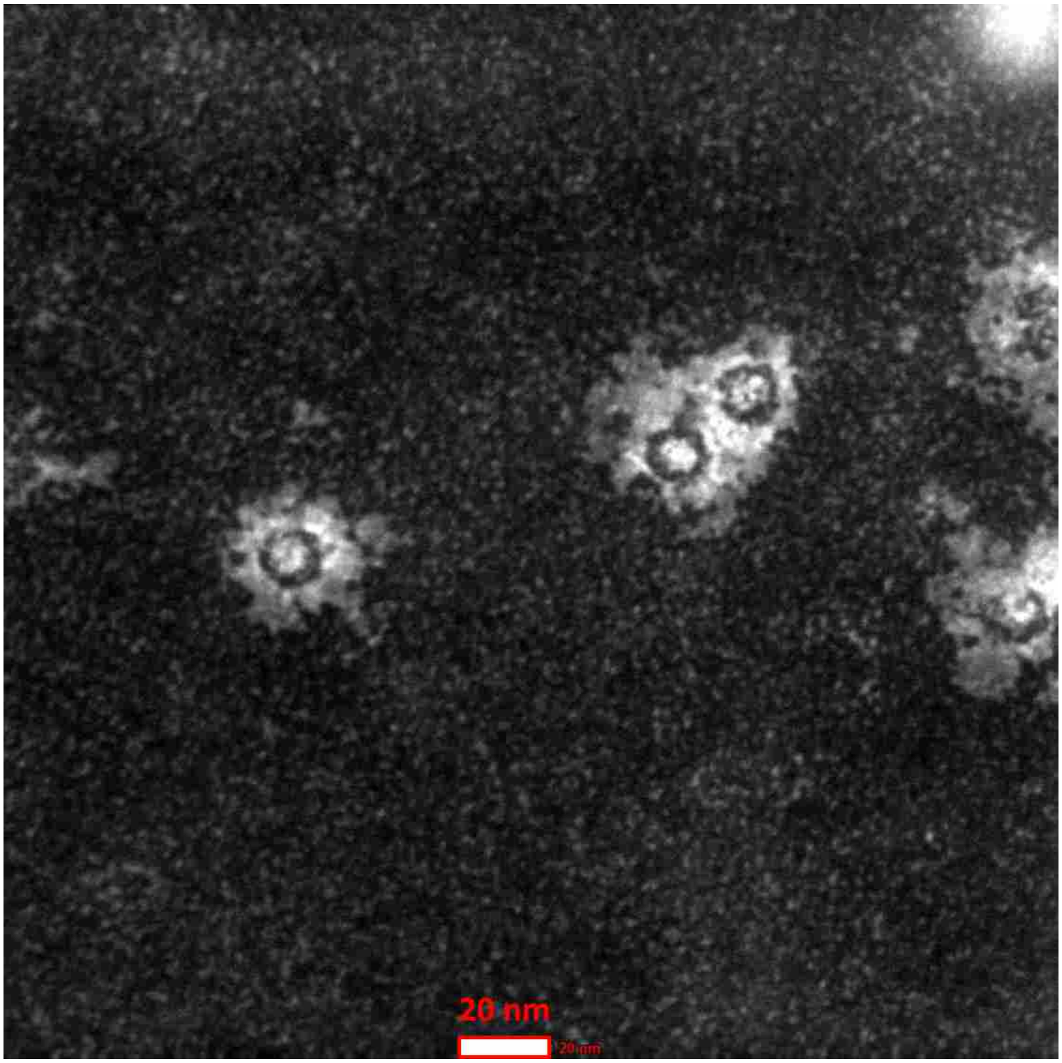

Supplemental Figure 6 - 3. Close of up titanium ferritin where AuNPs were formed using low intensity UV light. This shows an absence of AuNPs measuring less than 10 nm in diameter. Ferritin cores are shown as white circles inside dark halos, where the ferritin protein shells are the dark halos. The uranyl acetate stain is observed on the exterior of the protein shell.

References

---

[1] Eustis, S. & El-Sayed, M. A. Why gold nanoparticles are more precious than pretty gold: Noble metal surface plasmon resonance and its enhancement of the radiative and nonradiative properties of nanocrystals of different shapes. *Chem. Soc. Rev.* **35,** 209–217 (2006).

---

[2] Cheng, Y. *et al.* Highly Efficient Drug Delivery with Gold Nanoparticle Vectors for in Vivo Photodynamic Therapy of Cancer. *J. Am. Chem. Soc.* **130,** 10643–10647 (2008).

[3] L. Kennedy, L. Bickford, N. Lewinski, A. Coughlin, Y. Hu, E. Day, J. West and R. Drezek. A New Era for Cancer Treatment: Gold-Nanoparticle-Mediated Thermal Therapies. *Small* **7,** 169–183 (2011).

[4] Hirsch, L. R., Jackson, J. B., Lee, A., Halas, N. J. & West, J. L. A Whole Blood Immunoassay Using Gold Nanoshells. *Anal. Chem.* **75,** 2377–2381 (2003).

[5] C. Medley, J. Smith, Z. Tang, Y. Wu, S. Bamrungsap and W. Tan. Gold Nanoparticle-Based Colorimetric Assay for the Direct Detection of Cancerous Cells. *Anal. Chem.* **80,** 1067–1072 (2008).

[6] Keyes, J., Hilton, R., Farrer, J. & Watt, R. Ferritin as a photocatalyst and scaffold for gold nanoparticle synthesis. *J Nanopart Res* **13,** 2563–2575 (2011).

[7] Petrucci, O. D., Buck, D. C., Farrer, J. K. & Watt, R. K. A ferritin mediated photochemical method to synthesize biocompatible catalytically active gold nanoparticles: size control synthesis for small ([similar]2 nm), medium ([similar]7 nm) or large ([similar]17 nm) nanoparticles. *RSC Adv.* **4,** 3472–3481 (2014).

[8] Laufberger, V. Sur la cristallisation de la ferritine. *Bull. Soc. chim. biol* **19,** 1575–1582 (1937).

[9] Hentze, M. W. *et al.* Cloning, characterization, expression, and chromosomal localization of a human ferritin heavy-chain gene. *Proceedings of the National Academy of Sciences* **83,** 7226–7230 (1986).

[10] Carmona, U., Li, L., Zhang, L. & Knez, M. Ferritin light-chain subunits: key elements for the electron transfer across the protein cage. *Chem. Commun.* **50,** 15358–15361 (2014).

[11] Ensign, D., Young, M. & Douglas, T. Photocatalytic Synthesis of Copper Colloids from Cu(II) by the Ferrihydrite Core of Ferritin. *Inorg. Chem.* **43,** 3441–3446 (2004).

[12] Watt, R. K., Petrucci, O. D. & Smith, T. Ferritin as a model for developing 3rd generation nano architecture organic/inorganic hybrid photo catalysts for energy conversion. *Catal. Sci. Technol.* **3,** 3103–3110 (2013).

[13] Meldrum, F. C., Wade, V. J., Nimmo, D. L., Heywood, B. R. & Mann, S. Synthesis of inorganic nanophase materials in supramolecular protein cages. *Nature* **349,** 684–687 (1991).

[14] Douglas, T. & Stark, V. T. Nanophase Cobalt Oxyhydroxide Mineral Synthesized within the Protein Cage of Ferritin. *Inorg. Chem.* **39,** 1828–1830 (2000).

[15] Klem, M. T., Mosolf, J., Young, M. & Douglas, T. Photochemical Mineralization of Europium, Titanium, and Iron Oxyhydroxide Nanoparticles in the Ferritin Protein Cage. *Inorg. Chem.* **47,** 2237–2239 (2008).

[16] Okuda, M., Iwahori, K., Yamashita, I. & Yoshimura, H. Fabrication of nickel and chromium nanoparticles using the protein cage of apoferritin. *Biotechnology and Bioengineering* **84,** 187–194 (2003).

[17] Douglas, T. *et al.* Synthesis and Structure of an Iron (III) Sulfide-Ferritin Bioinorganic Nanocomposite. *Science* **269,** 54–57 (1995).

[18] Yamashita, I., Hayashi, J. & Hara, M. Bio-template Synthesis of Uniform CdSe Nanoparticles Using Cage-shaped Protein, Apoferritin. *Chemistry Letters* **33,** 1158–1159 (2004).

[19] Colton, J., Erickson, S., Smith, T. & Watt, R. Sensitive detection of surface- and size-dependent direct and indirect band gap transitions in ferritin. *Nanotechnology* **25,** 135703 (2014).

[20] Erickson, S. D., Smith, T. J., Moses, L. M., Watt, R. K. & Colton, J. S. Non-native Co-, Mn-, and Ti-oxyhydroxide nanocrystals in ferritin for high efficiency solar energy conversion. *Nanotechnology* **26,** 015703 (2015).

[21] T. Smith, S. Erickson, C. Orozco, A. Fluckiger, L. Moses, J. Colton and R. Watt. Tuning the band gap of ferritin nanoparticles by co-depositing iron with halides or oxo-anions. *J. Mater. Chem. A* **2,** 20782–20788 (2014).

[22] Kim, I., Hosein, H.-A., Strongin, D. R. & Douglas, T. Photochemical Reactivity of Ferritin for Cr(VI) Reduction. *Chem. Mater.* **14,** 4874–4879 (2002).

[23] Ensign, D., Young, M. & Douglas, T. Photocatalytic Synthesis of Copper Colloids from Cu(II) by the Ferrihydrite Core of Ferritin. *Inorg. Chem.* **43,** 3441–3446 (2004).

[24] Joo, M.-S., Tourillon, G., Sayers, D. E. & Theil, E. C. Rapid reduction of iron in horse spleen ferritin by thioglycolic acid measured by dispersive X-ray absorption spectroscopy. *Biology of metals* **3,** 171–175 (1990).

[25] Polanams, J., Ray, A. D. & Watt, R. K. Nanophase Iron Phosphate, Iron Arsenate, Iron Vanadate, and Iron Molybdate Minerals Synthesized within the Protein Cage of Ferritin. *Inorg. Chem.* **44,** 3203–3209 (2005).

[26] Lowry, O. H., Rosebrough, N. J., Farr, A. L. & Randall, R. J. Protein measurement with the Folin phenol reagent. *J Biol Chem* **193,** 265–275 (1951).

[27] Peterson, G. L. A simplification of the protein assay method of Lowry et al. which is more generally applicable. *Analytical Biochemistry* **83,** 346–356 (1977).

---

[28] Klem, M. T., Mosolf, J., Young, M. & Douglas, T. Photochemical Mineralization of Europium, Titanium, and Iron Oxyhydroxide Nanoparticles in the Ferritin Protein Cage. *Inorg. Chem.* **47,** 2237–2239 (2008).

[29] T. Smith, C. Olsen, J. Embley, S. Erickson, D. Buck, A. Neilson, J. Colton, R. Watt. Tuning the band gap of ferritin nanoparticles by co-depositing iron with halides or oxo-anions. *J. Mater. Chem. A* **2,** 20782–20788 (2014).

[30] Habib, A., Tabata, M. & Wu, Y. G. Formation of Gold Nanoparticles by Good's Buffers. *Bulletin of the Chemical Society of Japan* **78,** 262–269 (2005).

[31] Xie, J., Lee, J. Y. & Wang, D. I. C. Seedless, Surfactantless, High-Yield Synthesis of Branched Gold Nanocrystals in HEPES Buffer Solution. *Chem. Mater.* **19,** 2823–2830 (2007).

[32] Tong, S. W. *et al.* Improvement in the hole collection of polymer solar cells by utilizing gold nanoparticle buffer layer. *Chemical Physics Letters* **453,** 73–76 (2008).

[33] Tian, Y. & Tatsuma, T. Mechanisms and Applications of Plasmon-Induced Charge Separation at TiO2 Films Loaded with Gold Nanoparticles. *J. Am. Chem. Soc.* **127,** 7632–7637 (2005).

[34] Maeland, A. & Flanagan, T. B. Lattice spacings of gold-palladium alloys. *Canadian journal of physics* **42,** 2364–2366 (1964).

Chapter 7 – Synthesis of Manganese (II/III), (III), and (IV) Ferritin Using Comproportionation

This paper was submitted to Journal of Inorganic Chemistry on May 20, 2015, and is titled "The Synthesis of Manganese (II/III), (III), and (IV) Ferritin Minerals". I am the First Author of this paper, and preformed all of the sample synthesis, = characterization, and writing. I received assistance from Stephen Erickson, Jacob Embley, and Cameron Olsen. I also received editing assistance from Dr. John Colton and Dr. Richard Watt, as well as the above mentioned undergraduate students.

Abstract

This paper investigates comproportionation reactions of Mn(II) with permanganate as a route for manganese oxide nanoparticle synthesis in ferritin. We report reaction schemes that used manganese comproportionation reactions in the presence of apoferritin and control reactions with only permanganate and apoferritin to create Mn3O4, Mn2O3, and MnO2 mineral cores in ferritin. The reaction schemes that produced these different manganese minerals rely on altering the Mn(II):MnO4- ratios and running the reactions in acidic, neutral or basic buffers. The mineralization of manganese inside ferritin was verified through the co-elution of ferritin and manganese through gel filtration columns and through tunneling electron microscopy. The oxidation states of the manganese minerals were characterized using coulometry and the mineral core types were deduced from the Pourbaix diagram. The band gaps of the resulting minerals were determined by optical absorption spectroscopy.

Introduction

The synthesis and characterization of nanoparticles is important due to their biomedical, optical, and electronic applications. Nanoscale materials possess unique properties that are different than atomic or bulk properties. For example, nanoscale metal oxides have been used as bactericides,[1] nano-sensors[2], and mammalian cell toxins[3]. Controlling the size, shape, and composition of these nanomaterials greatly affects their optical and chemical properties, thus increasing their utility.

The biomolecule ferritin has been used as a scaffold for the encapsulation of metal-oxide nanoparticles.[4,5,6,7] The protein complex is a 450 kDa biomolecule composed of 24 subunits. The ferritin subunits assemble into a sphere measuring 12 nm in diameter with an 8 nm hollow interior. In nature, ferritin's primary role is to sequester iron as a ferrihydrite [Fe(O)OH] mineral.

Ferritin metal-oxide cores are traditionally synthesized *in vitro* by reacting a low oxidation state transition metal (typically the 2^+ state) with the ferroxidase center in ferritin. Oxygen, or other external oxidants such as peroxide, oxidize the metal to form a M(O)OH mineral (where M is a metal typically in the 3^+ oxidation state).[5,6] Using this procedure or slight variations of this procedure, material chemists have synthesized a variety of metal nanoparticles in ferritin.[4,5,6,7] Additionally, metal oxo-anion minerals have been synthesized by adding oxo-anions to the reaction buffer during iron loading.[7,8] The mechanism allowing these oxo-anions to enter ferritin is unknown but potentially these oxo-anions can diffuse into the ferritin interior.[9,10]

The synthesis of nanoparticles inside ferritin allows for a variety of advantages, including obtaining a uniform size distribution and maintaining nanoparticle solubility. The protein shell is advantageous because it can be organized into ordered architectures for various applications.[11,12] The ability to organize the ferritin protein shell into architectures automatically organizes the encapsulated metal nanoparticles into the same pattern. The unique properties of the ferritin organic/inorganic architectures show potential in bio-battery[13,14,15] and light harvesting applications.[,16,17,18,19]

Recent work has focused on the photocatalytic properties of ferritin.[20,21] Erickson et al.[17] used optical absorption spectroscopy to investigate band gaps of non-native metal-oxides synthesized inside ferritin and reported the following indirect band gaps and direct transitions: Mn(III)-ferritin (1.60 eV, 2.83 eV), Co(III)-ferritin (1.93 eV, 2.65 eV), and Ti(IV)-ferritin (2.19 eV, 3.8 eV). In a similar study, Smith et al. measured the indirect band gap and direct transition of iron oxo-anion minerals synthesized in ferritin by the co-deposition of iron with oxo-anions such as phosphate (2.38 eV, 3.23 eV), molybdate (2.11 eV, 3.00 eV), tungstate (2.24 eV, 3.06 eV), and permanganate (1.99 eV, 2.88 eV).[7]

The Mn(III)-ferritin samples prepared in Ref. 17 and elsewhere[22,23] have followed the synthesis method described above, and will be referred throughout this work as the "Meldrum method[6]". However, the observation by Smith et al. that ferritin iron loading in the presence of permanganate produced a ferritin mineral core with both iron and manganese[7] indicated a potential new route for manganese loading into ferritin. The interaction of permanganate with ferritin is unique with the potential to: 1) use permanganate to replace oxygen as the oxidant at the ferritin ferroxidase center for metal loading by oxidizing lower valent metals such as Mn(II), or 2) permanganate might enter ferritin like other oxo-anions by diffusing into the ferritin interior and oxidize divalent metals from the interior. Based on these potential reactions, we also recognized the possibility of forming higher valent manganese species in ferritin. Higher valent species might have different photochemical properties than known manganese(III) ferritin samples[6] and would certainly have applications in nanobattery technology.[14]

The overall goal of this study was to evaluate new synthetic routes for preparing manganese ferritin by incubating apoferritin with Mn(II) and permanganate. In the process we desired to obtain some mechanistic understanding of the reactions to apply towards future synthetic reactions. We identified comproportionation reactions and used these reactions to predict probable manganese ferritin products.

One goal was to prepare Mn(IV) in ferritin. To do this we proposed to perform a Mn(II)/Mn(VII) comproportionation reaction to prepare a ferritin Mn(IV)O_2 mineral core, see Eq. 1. We hypothesized this reaction could occur because it is known that both oxo-anions[7,8,24,25,26] and divalent metals[24,25,27,28,29,30,31] can diffuse into the ferritin cavity. If both Mn(II) and permanganate diffuse into the ferritin interior, the comproportionation reaction shown in Eq. 1 could occur in the ferritin interior to produce a Mn(IV) mineral inside ferritin.

Apoferritin + $3Mn(II) + 2\ Mn(VII)O_4^- \rightarrow 5Mn(IV)O_2$-ferritin (Eq. 1)

However, we recognized another comproportionation reaction with a different $Mn(II):MnO_4^-$ ratio could result in a Mn(III) core, see Eq. 2.

Apoferritin + $4Mn(II) + Mn(VII)O_4^- \rightarrow 5Mn(III)_2O_3$-ferritin (Eq. 2)

Therefore, altering the stoichiometry could in theory allow one to select between an Mn(III) and an Mn(IV) mineral in ferritin (Fig. 1). We will refer to the samples prepared with the 3:2 and the 4:1 Mn(II) to $Mn(VII)O_4^-$ ratios, shown in Eq. 1 and Eq. 2 as samples A and B, respectively.

Another important factor to consider in these reactions is the effect of pH. Manganese redox reactions are pH dependent, so it is important to test the reactions in acidic, neutral and basic conditions (pH 5.4, 7.4 or 9.4) to determine the pH that maximizes the loading of manganese into ferritin or controls the oxidation state of the resulting mineral. A reaction scheme for the comproportionation reactions and proposed products for samples A and B is shown in Figure 7-1(a).

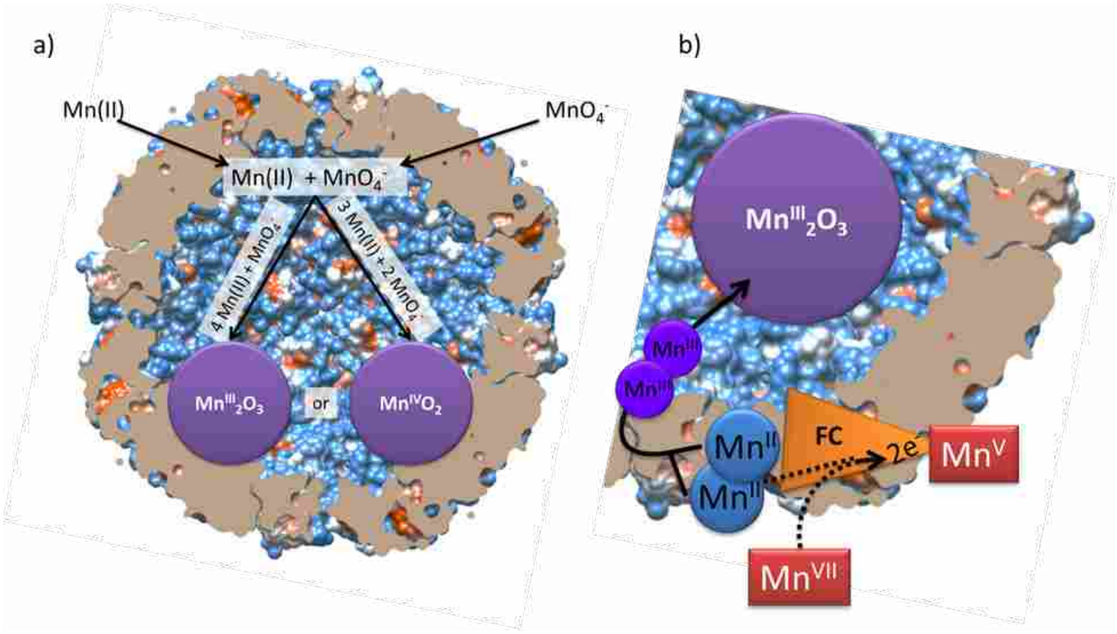

Figure 7 - 1. Scheme of hypothesized reactions for manganese loading into ferritin. (a) Scheme for samples A and B, using the reactions given in Eqs. 1 and 2. Manganese and permanganate first enter ferritin and then undergo a comproportionation reaction to form either a Mn(IV) or Mn(III) mineral. Eqs. 1 and 2 represent the right-hand and left-hand pathways in the figure, respectively. (b) Scheme for sample C, using the reaction given in Eq. 3. Mn(II) binds at the ferroxidase center (FC) and is oxidized to Mn(III) by permanganate. After oxidation the Mn(III) ions migrate to the ferritin interior and become mineralized as an Mn(III) compound such as Mn_2O_3 or MnO(O)H. Model generated using UCSF Chimera software package PDB code 1FHA.

Additionally we recognized that the ferroxidase center of ferritin might control the redox state of the final mineral formed in ferritin. If two Mn(II) ions bind at the ferroxidase center and permanganate acts as the oxidant, the two Mn(II) ions can each donate an electron to permanganate to form two Mn(III) ions that would migrate into the ferritin interior and mineralize inside ferritin. Mn(V) would be the product of permanganate reduction. This is described in Eq. 3. The Mn(III) mineral could be Mn(O)OH as in the Meldrum method, Mn_2O_3, or another Mn(III) compound. We will refer to the sample prepared with the 2:1 Mn(II) to

$Mn(VII)O_4^-$ ratio as sample C. The reaction scheme for Eq. 3 and the hypothesized product for sample C is shown in Figure 7-1(b).

$$\text{Apoferritin-FC} + 2\text{Mn(II)} + \text{Mn(VII)O}_4^- \rightarrow 2\text{Mn(III)-ferritin} + \text{Mn(V)} \qquad \text{(Eq. 3)}$$

If the ferroxidase center reaction dominates the oxidation of Mn(II) as in Eq. 3, as opposed to the diffusion process and comproportionation reaction occurring inside of ferritin as in Eq. 1, then it is possible that a Mn(III) mineral would be produced even if the stoichiometry favors the formation of a Mn(IV) mineral (e.g. the 3:2 ratio of sample A).

It is also possible that the resulting Mn(V) from Eq. 3 could undergo a second 2-electron reduction at the ferroxidase center with Mn(II) ions and enter ferritin as Mn(III).[32] That would lead to Eq. 4. Note that Eq. 4 has the same stoichiometry as Eq. 2 (as used in sample B); the difference is that Eq. 2 relies on the comproportionation reaction occurring inside ferritin whereas Eq. 4 relies on the ferroxidase center of ferritin and requires any Mn(V) formed to also react at the ferroxidase center and be reduced to Mn(III). Since Eqs. 2 and 4 are chemically indistinguishable, one cannot determine from the 4:1 ratio of sample B which process is occurring.

$$\text{Apoferritin-FC} + 4\text{Mn(II)} + \text{Mn(VII)O}_4^- \rightarrow 5\ \text{Mn(III)-ferritin} \qquad \text{(Eq. 4)}$$

In this paper we report the successful synthesis of manganese oxide nanoparticles inside ferritin. The resulting minerals are Mn_3O_4 and Mn_2O_3 depending on the synthesis scheme used, and possess lower oxidation states than predicted in the hypothesized reaction schemes. The unexpected lower oxidation states are a result of oxidation of the ferritin protein itself by the permanganate. Characterization of these new ferritin manganese minerals shows that they are different than the manganese minerals formed using the traditional Meldrum method.

Additionally, a new Mn(IV) mineral, MnO_2, was formed under high pH conditions using only apoferritin and permanganate, i.e. with no Mn(II) present in solution.

Materials and Methods

Synthesis

Apoferritin samples were prepared from horse spleen ferritin following established methods using thio-glycolic acid dialysis with horse spleen ferritin. Manganese loading into ferritin was performed at three different pH values: 5.4, 7.4, and 9.4 for the majority of the reactions outlined in the Introduction. Apoferritin was prepared at these pH values by adding 5.0 mg of apoferritin to 1.0 mL of one of the following three buffered solutions containing either: 1 M pH 5.4 2-(N-morpholino)ethanesulfonic acid (MES) buffer, 1 M pH 7.4 imidazole buffer, or 1 M pH 9.4 N-(1,1-Dimethyl-2-hydroxyethyl)-3-amino-2-hydroxypropanesulfonic acid (AMPSO) buffer. Manganese was then added to the apoferritin solution by one of the following methods to synthesize the manganese ferritin cores. Mn(II) ions were supplied by adding $MnCl_2$ in precise amounts to the solution.

Comproportionation reactions with apoferritin using a 3:2 ratio of Mn(II) to MnO_4^- (sample A) were performed by co-additions of first 80 MnO_4^-/ferritin (10 µL of 88 mM $KMnO_4$) followed quickly by an addition of 120 Mn(II)/ferritin (10 µL of 143 mM $MnCl_2$) to 5 mg of apoferritin. This stoichiometric ratio of 3 Mn(II) per 2 MnO_4^- targets a Mn(IV) product (Eq. 1). These additions were repeated 8 times, with at least 10 minutes between each addition to target a core size of 1600 Mn/ferritin. The reactions were performed in each of the buffers indicated above, at pH 5.4, 7.4 and 9.4. Only the pH 9.4 reactions using this stoichiometric ratio resulted in manganese loading into ferritin.

Based on the fact that the 3 Mn(II) per 2 MnO_4^- ratio only produced a manganese core at pH 9.4, the other stoichiometric ratios for comproportionation reactions were only tested at pH 9.4. These included reactions using Mn(II) to MnO_4^- ratios of 4:1 (sample B) and 2:1 (sample C). For these reactions, the ferritin concentration was 3.0 mg of apoferritin because the other comproportionation reactions produced significant protein loss during the reaction. Additionally a balanced stoichiometric ratio was also performed anaerobically to see if oxygen was competing with permanganate as the oxidant. The results of the aerobic and anaerobic reactions were within experimental error indicating that permanganate was the predominant electron acceptor and any results relating to final oxidation states were not skewed by the presence of oxygen as an oxidant.

A control reaction where apoferritin was incubated with permanganate in the absence of Mn(II) was performed by adding 200 µL of 88 mM $KMnO_4$ to 5 mg of apoferritin solution using a syringe pump. The solution was added at a rate of 10 µL per hour, or 80 Mn/ferritin per hour, targeting 1600 Mn/ferritin. This synthesis was performed at pH 5.4, 7.4, and 9.4 and will be referred to as sample D1, D2, and D3, respectively.

After the synthesis reactions were complete, all samples were centrifuged and the supernatant containing ferritin decanted. The ferritin samples were loaded onto a 12.5 cm x 1 cm Sephadex G-75 size exclusion column, which was buffered with 25 mM pH 7.4 imidazole, no salt. The eluting ferritin peak was collected and characterized for manganese content by the methods described below.

Characterization

Protein and metal analyses were completed using standard methods;[7,17] protein analysis was performed using the Bradford Method[33], and metal analysis was performed using inductively coupled plasma mass spectrometry (ICP-MS). The ratio between the two molar concentrations gives the relative manganese per ferritin ratio, which is indicative of nanoparticle size.

Tunneling electron microscope (TEM) images were prepared using an amorphous carbon TEM slide with a 300 mesh copper grid. The grids were placed under a vacuum and charged with a static electricity generator. 3.5 μL of the manganese ferritin samples were then added to the TEM grid for 60 seconds. Afterwards, the excess solution was wicked away with a Kimwipe followed by a water wash with a water droplet. This ferritin TEM sample was then treated with a negative stain to visualize the ferritin protein shell by adding 3.5 μL of 2.5% uranyl acetate for 60 seconds, and the excess solution was wicked away with a Kimwipe. The TEM grid was then rinsed with a water droplet. Bright field images and diffraction patterns were captured using a Tecnai-F20 TEM.

Energy-dispersive X-ray spectroscopy (EDX) was used to analyze the mineral content inside of ferritin while the Tecnai-F20 was in Scanning Tunneling Electron Microscopy (STEM) mode. The STEM beam was focused to approximately 3 nm and then scanned across an individual ferritin molecule while Mn-K_α X-rays were measured by EDX.

X-ray powder diffraction studies were performed using a Brunker-Nonius FR591 single crystal diffractometer with a rotating Cu anode. Data was collected in transmission mode X-ray diffraction (XRD) with a polyimide capillary that contained the manganese ferritin solutions.

Coulometry experiments were performed to calculate the total number of electrons used to reduce the manganese mineral. This was done using a slight modification of the Watt et al.[34] procedure, where the tris(hydroxymethyl)aminomethane (TRIS) pH was adjusted to pH 7.0 to better suit the manganese reduction. The solution also contained 500 mM NaCl and 100 μM methyl viologen as the electron mediator. A potential of –800 mV vs. saturated $Ag^+/AgCl$ reference electrode was used to reduce the manganese core to Mn(II). Current was measured as a function of time with 10-30 μL additions of anaerobic manganese ferritin to the reduced solution. These additions caused a change in current. With current plotted as a function of time, the curve was integrated (area calculated) to yield the total charge and hence total number of electrons used to reduce the manganese oxide core to Mn(II).

Band gaps were measured using optical absorption spectroscopy as described by Colton et al.[16]

Results and Discussion

Sample Preparation and Ferritin Characterization after Synthesis

Samples A, B, and C were prepared using Mn(II) to MnO_4^- ratios of 3:2, 4:1, and 2:1 with hypothesized synthesis reactions of Eqs. 1, 2, and 3, respectively, as discussed in the Introduction. Once the synthesis reactions were complete, the samples were centrifuged to remove metal particulates and denatured protein, followed by the supernatant being passed over a Sephadex G-75 column (1 cm x 12.5 cm) to separate the manganese-containing ferritin from the unsequestered manganese ions in solution. For all ferritin samples, manganese co-migrated with the ferritin as is shown in Figure 7-2, which is representative of the elution profiles for all samples. The 1.0 mL fractions were then analyzed for manganese content using ICP-MS. Ferritin eluted in fractions 4, 5, and 6 and showed high manganese content. Unbound manganese was observed in fractions 9 to 15. After separating the ferritin from unbound manganese, the samples were placed on TEM grids for TEM analysis and the absorption spectrum of each sample was recorded and the samples were photographed.

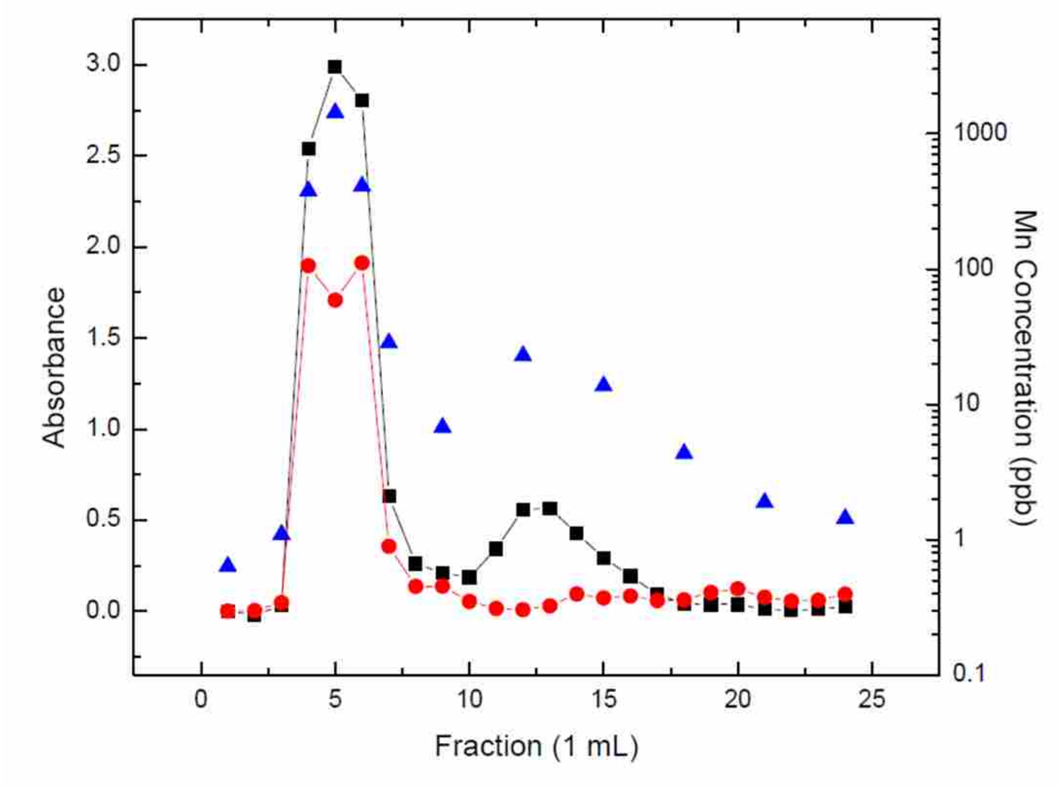

Figure 7 - 2. Ferritin elution profile on a 12.5 cm x 1.0 cm G-75 size exclusion column. After the synthesis reactions, ferritin was purified using a Sephadex G-75 size exclusion column (1.0 cm x 12.5 cm). The figure shows the resulting elution profile showing the separation of a manganese-ferritin from unbound manganese. Fractions (1.0 mL) were collected and analyzed. The absorption of the manganese mineral in ferritin is measured at 420 nm (red circles). Both the ferritin and MES buffer elution are measured at 255 nm (black squares). The manganese concentration in each fraction was measured by ICP-MS (blue triangles) and is displayed on the secondary y-axis on a log scale. This figure is representative of the elution profiles of all manganese-ferritin samples; the specific sample shown here is sample D1 (permanganate reacted with apo ferritin at pH 5.4).

TEM images show the presence of nanocrystals inside ferritin, and bright field images for samples A, B, and C are shown in Figures 7-3(a), 7-4(a), and 7-5(a), respectively. The metal cores are observed in the interior of ferritin as dark spots. The ferritin spheres are approximately 12 nm in diameter with interiors measuring 8 nm across, consistent with metal-loaded ferritin. STEM mode was employed to perform EDX analysis of the samples. As the STEM beam was scanned across the surface of the mineral, backscattered X-rays from the elements in the sample were detected by the EDX. Specific STEM traces and EDX results are shown in parts (b) and (c) of Figures 7-3, 7-4, and 7-5, respectively. The EDX analysis verified the presence of Mn on the interior of the ferritin proteins.

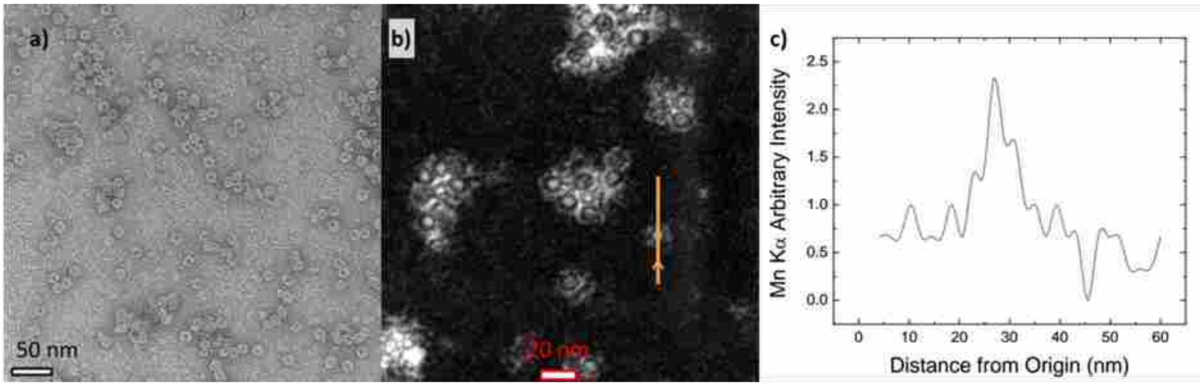

Figure 7 - 3. TEM analysis of sample A, manganese-loaded ferritin prepared using a 3:2 ratio of Mn(II) to MnO_4^-. (a) Bright field TEM image. (b) STEM image, with line scan for the EDX measurement indicated in orange. (c) The intensity of the Mn-Kα signal as a function of distance from the origin. Manganese is observed between 22 and 32 nm which corresponds to the interior of the ferritin molecule.

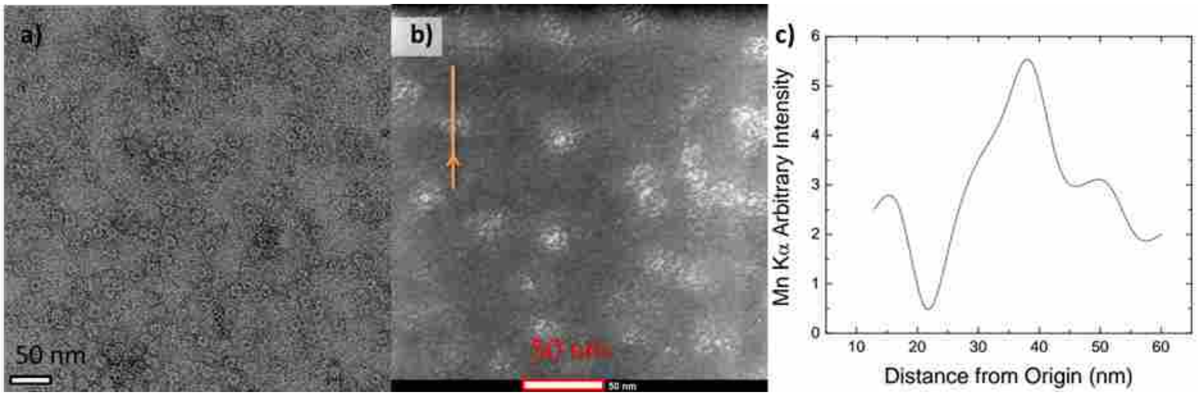

Figure 7 - 4. TEM analysis of sample B, manganese-loaded ferritin prepared using a 4:1 ratio of Mn(II) to MnO_4^-. (a) Bright field TEM image. (b) STEM image, with line scan for the EDX measurement indicated in orange. (c) The intensity of the Mn-Kα signal as a function of distance from the origin.

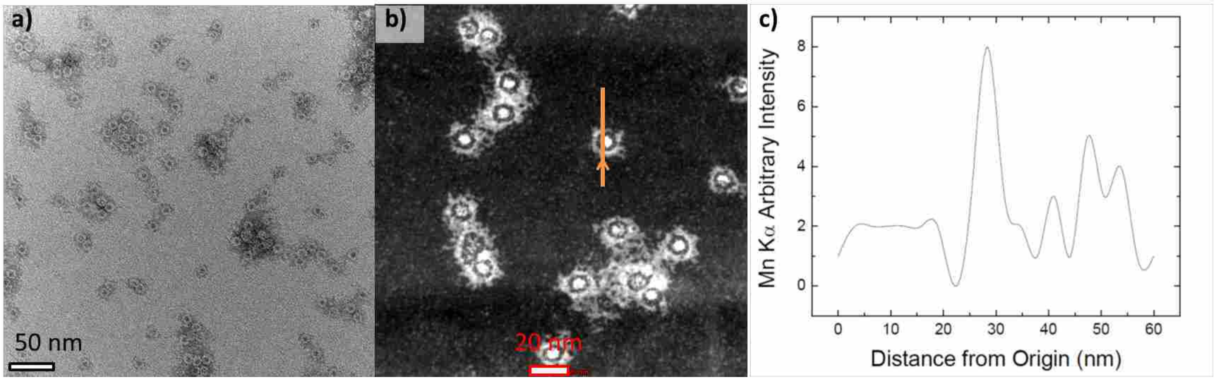

Figure 7 - 5. TEM analysis of sample C, manganese-loaded ferritin prepared using a 2:1 ratio of Mn(II) to MnO4-. Bright field TEM image. (b) STEM image, with line scan for the EDX measurement indicated in orange. (c) The intensity of the Mn-Kα signal as a function of distance from the origin.

Electron diffraction studies were also performed with the TEM; however, the samples were amorphous and did not produce clear diffraction data. (See Supplemental Figure 7-1) XRD analysis similarly suggested an amorphous manganese core inside ferritin (data not shown).

The metal content of these ferritin samples was calculated from the protein and metal analyses and were 1350 ± 75 Mn/ferritin for sample A, 4200 ± 100 Mn/ferritin for sample B, and 1000 ± 150 Mn/ferritin for sample C. The metal/ferritin content along with various other measured and targeted parameters for the three samples are summarized in Table 7-1 and are compared to a fourth sample synthesized using the Meldrum synthesis method (please add the meldrum reference here). The Meldrum sample's nanoparticle size was 650 ± 50 Mn/ferritin.

The absorption spectra of samples A, B, C, and Meldrum are presented in Figure 7-6. The absorption peak at 280 nm comes from the ferritin protein; the absorbance tailing into the visible wavelengths arises from the metal cores. The inset photographs give a visual comparison of samples A, B, and C. The more intense absorption near 400 nm observed in the new samples suggests that the new synthesis reactions produce a different manganese oxide mineral in ferritin than the traditional Meldrum method. Both the spectra and photos are of the samples with a ferritin concentration of 0.1 mg/mL.

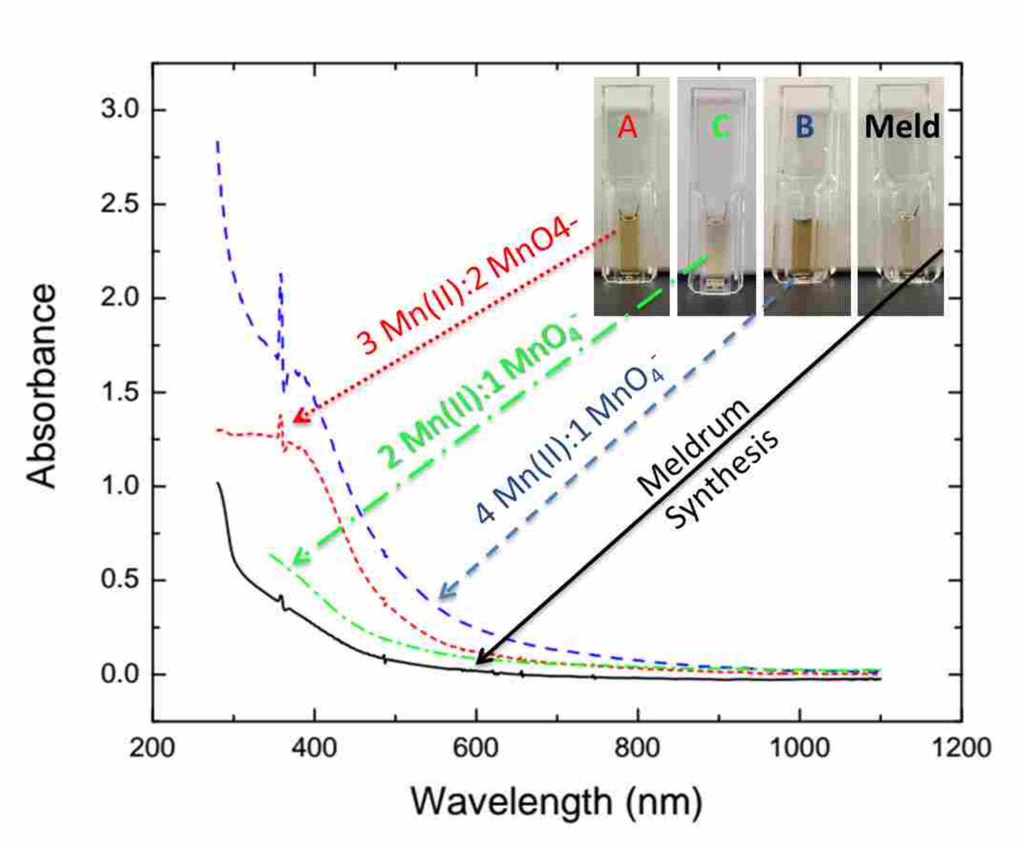

Figure 7 - 6. Absorption spectra of manganese-loaded ferritin samples A (red curve; 3:2 ratio of Mn(II) to MnO_4^-), sample B (blue curve, 4:1 ratio), sample C (green curve, 2:1 ratio), and Meldrum sample (black curve). The increased absorption near 400 nm in the new samples suggests a different mineral than in the Meldrum sample. The inset shows photographs of the four samples, from left to right: A, C, B, Meldrum.

Coulometry experiments were performed to count the number of electrons required to reduce each manganese oxide mineral to the Mn(II) oxidation state. The coulometry experiments were conducted at pH 7.0 in order to reduce all of the different mineral oxides in accordance with the associated Pourbaix diagram.[35] From this, the oxidation states of the manganese minerals were determined and the chemical formula of the associated manganese oxide minerals was deduced. For sample A (3:2 ratio of Mn(II) to MnO_4^-) the coulometry results showed that it could accept 1.0 electron/Mn, indicating an oxidation state of Mn(III), a likely mineral from the Pourbaix diagram of Mn_2O_3. This differs from the targeted mineral given in Eq. 1 which would have an oxidation state of Mn(IV). Samples B (4:1 ratio) and C (2:1 ratio) both accepted 0.7 electrons/Mn, have oxidation states which are a mixture of Mn(II) and Mn(III), and have suggested minerals from the Pourbaix diagram of Mn_3O_4. These again disagree with their targeted oxidation states of Mn(III) from Eqns 2 and 3. This information is also summarized in Table 7-1.

Table 7 - 1. A summary of important parameters for samples A, C, and B, formed via manganese comproportionation synthesis. The samples are listed in increasing stoichiometric ratio. The last column is the sample from the traditional Meldrum method with its known parameters.

	Sample A	**Sample C**	**Sample B**	**Meldrum**
Stoichiometric Ratio, Mn(II):MnO_4^-	3:2	2:1	4:1	n/a
Hypothesized reaction	Eq. 1	Eq. 3	Eq. 2	n/a
Targeted Oxidation State	Mn(IV)	Mn(III)	Mn(III)	n/a
Final Protein Content (mg)*	4.0	2	0.8	n/a
Percent Protein Loss	20 %	30%	75%	n/a
Size (Mn/ferritin)	1350 ± 75	1000 ± 150	4200 ± 100	650 ± 50
Electrons/Mn to reduce to Mn(II)	1.0	0.7	0.7	1
Deduced Oxidation State	Mn(III)	Mn(II)/ Mn(III) mixture	Mn(II)/ Mn(III) mixture	Mn(III)
Suggested Mineral from Pourbaix diagram	Mn_2O_3	Mn_3O_4	Mn_3O_4	Mn(O)OH

*The 4:1 and 2:1 ratios were performed using only 3 mg of apoferritin. The 3:2 ratio used 5 mg of apoferritin.

An inspection of Table 7-1 yields several interesting observations. The first is that the observed oxidation state of the manganese product in ferritin is consistently lower than anticipated. The second observation is that the Mn/ferritin ratio in samples B and C was much higher than the maximum theoretical loading of 1600 Mn/ferritin (the theoretical maximum being set by the amount of Mn introduced during synthesis). The third observation is that significant protein loss occurred during the synthesis reactions. During several of the reactions, we observed that the solution became cloudy, suggesting protein denaturation. We interpret these results by assuming that permanganate is oxidizing the protein and causing the extensive protein damage. The oxidation of the protein consumed sufficient permanganate to alter the reaction stoichiometries and lower the oxidation state of each product from what was predicted.

One of our original goals was to evaluate the products of each of the proposed synthesis reactions (Eqs. 1, 2 and 3) in order to determine the mechanism of manganese loading into ferritin, i.e. whether the manganese utilized the ferroxidase center or not. Unfortunately, the significant protein loss and corresponding unexpected oxidation states do not allow us to interpret the equations as expected for these three samples. However, we did succeed in preparing new manganese ferritin minerals using this new method, two of which (samples A and C) resulted in cores with marginal protein losses of 20% and 30 % respectively.

Permanganate Loading into Apoferritin

To test the possibility that permanganate might diffuse into apoferritin and remain encapsulated, we reacted permanganate with apoferritin in the absence of Mn(II). This was done under three different pH conditions. We will refer to the samples prepared under pH 5.4, pH 7.4, and pH 9.4 as samples D1, D2, and D3, respectively. The targeted manganese loading for these experiments was 1600 Mn/ferritin. Manganese was observed to load into ferritin under these conditions, even in the absence of Mn(II). Approximately 60-70% of the ferritin was denatured, suggesting that the protein acted as a sacrificial electron donor and reduced the permanganate to a lower valent manganese species that was encapsulated inside ferritin. A summary of the data from these samples is shown in Table 7-2.

Table 7 - 2. A summary of important parameters for samples D1, D2, and D3, formed via permanganate loading into apoferritin in the absence of Mn(II).

	Sample D1	**Sample D2**	**Sample D3**
pH	pH 5.4	pH 7.4	pH 9.4
Final Protein Content (mg)*	2	2	1.5
Percent Protein Loss	60 %	60 %	70 %
Size (Mn/ferritin)	1850 ± 75	450 ± 30	160 ± 5
Electrons/Mn to reduce to Mn(II)	0.7	0.7	2.0
Deduced Oxidation State	Mn(II)/ Mn(III) mixture	Mn(II)/ Mn(III) mixture	Mn(IV)
Suggested Mineral from Pourbaix diagram	Mn_3O_4	Mn_3O_4	MnO_2

*Original protein content was 5 mg of apoferritin.

The pH loading efficiency was opposite of that which was observed for the comproportionation reactions. Permanganate reduction is known to be favored under acidic conditions, whereas manganese (II) oxidation, hydrolysis and mineralization into ferritin is favored under basic conditions. With these samples, the reaction performed at pH 5.4 (sample D1) produced the largest manganese cores (1850 Mn/ferritin). Samples D1 and D2 both accepted 0.7 electrons/Mn in the coulometry experiment and have oxidation states which are a mixture of Mn(II) and Mn(III), and have suggested minerals of Mn_3O_4 from the Pourbaix diagram. This indicates these samples are similar to samples B and C discussed above. By contrast, sample D (pH 9.4) accepted 2 electrons/Mn, which indicates an oxidation state of Mn(IV) and gives a suggested mineral of MnO_2. This is very different than all the samples produced through the comproportionation reactions (A, B, and C) as well as the sample created with the traditional synthesis method (Meldrum), and achieves our goal of creating an Mn(IV) mineral albeit one with small cores of only 160 Mn/ferritin. The absorption spectra of the permanganate–loaded ferritin are displayed in Figure 7-7.

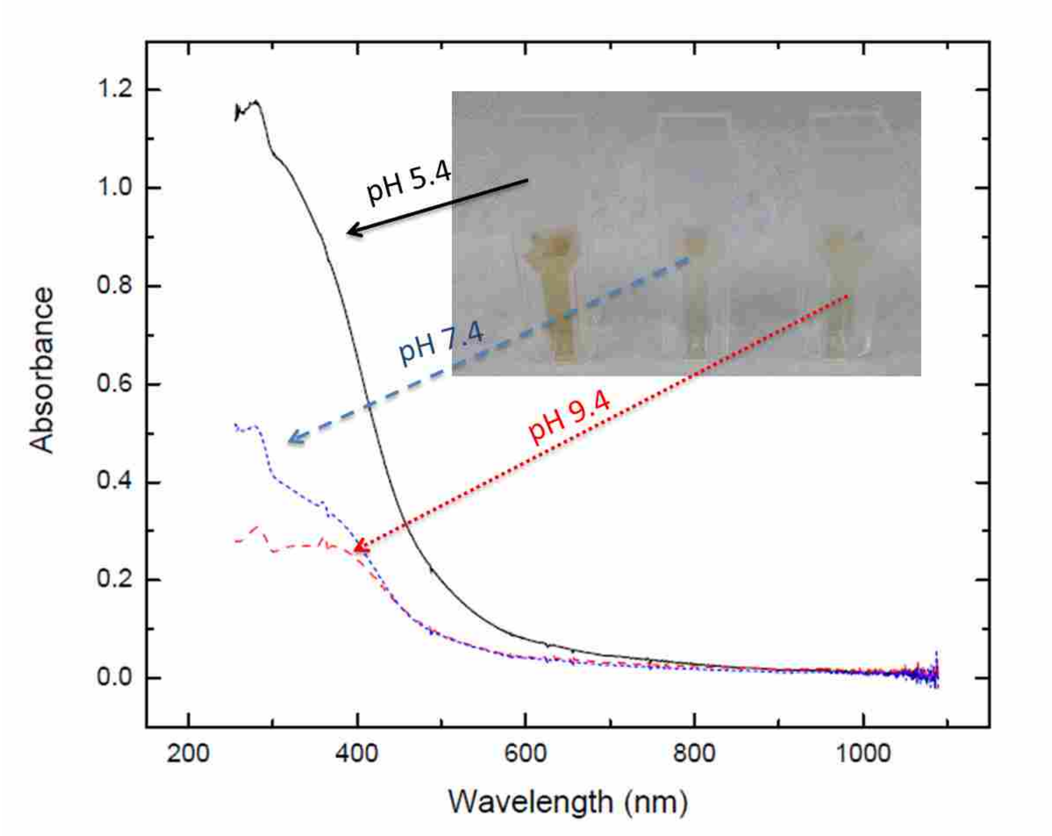

Figure 7 - 7. Absorption spectra of permanganate-loaded ferritin samples D1 (black, pH 5.4), D2 (blue, pH 7.4), and D3 (red, pH 9.4). Each sample was prepared at 0.10 mg/mL ferritin. The inset shows photographs of the three samples, from left to right: D1, D2, D3.

TEM images from sample D3, the only sample to feature a Mn(IV) mineral core, are shown in Figure 7-8. TEM images from samples D1 and D2 are shown in Supplemental Figure 7-2 and Supplemental Figure 7-3, respectively. The data for sample D1 includes EDX analysis showing the presence of Mn inside the core; the nanoparticles in samples D2 and D3 were too small to allow for EDX analysis. As with the comproportionation samples (A, B, and C), the TEM analyses of samples D1, D2, and D3 showed the manganese cores to be amorphous.

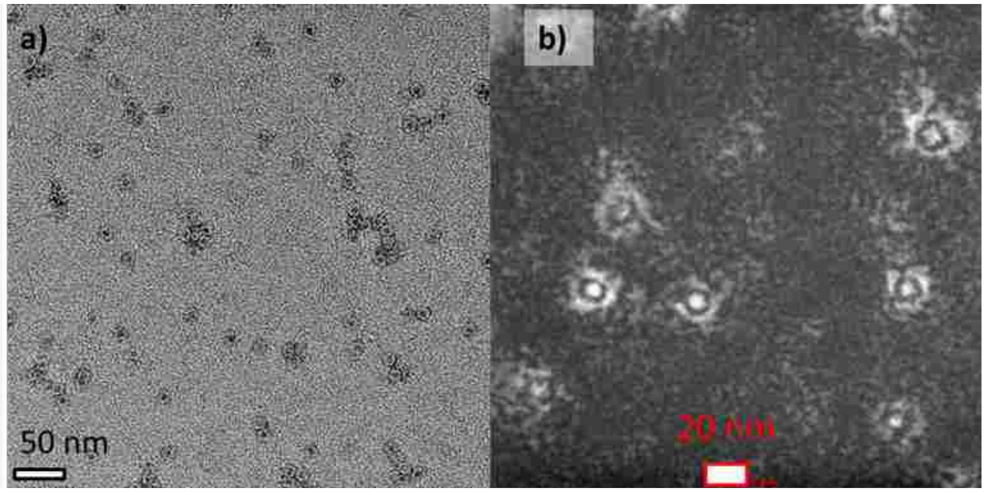

Figure 7 - 8. TEM analysis of sample D3, manganese-loaded ferritin prepared by the permanganate loading into apoferritin reaction at pH 9.4, which formed a Mn(IV) mineral. (a) Bright field TEM image. (b) STEM image. The manganese cores for this sample (160 Mn/ferritin) were insufficient to perform EDX analysis.

Band Gap Measurements of the Manganese Ferritin Minerals

Band gap measurements were performed on all of the samples to further illustrate the differences between the Meldrum manganese synthesis[6] and the comproportionation reactions performed in this study. The manganese minerals were found to be indirect band gap semiconductors that also contain a direct transition. Specific band gaps are given in Table 7-3. Manganese oxide minerals using the Meldrum synthesis method have previously been shown to be indirect band gap semiconductors with an indirect band gap of 1.65 eV and a direct transition of 2.85 eV.[17] In contrast, the comproportionation samples had indirect gaps (direct transitions) of 1.90 eV (2.56 eV), 1.85 eV (2.70 eV), and 1.98 eV (2.70 eV) for samples A, B, and C, respectively. The permanganate control reactions resulted in indirect gaps (direct transitions) of 1.94 eV (2.66 eV), 1.94 eV (2.66 eV), and 1.94 eV (2.59 eV) for samples D1, D2, and D3, respectively. These new materials are significantly different than the Meldrum sample reported by Erickson et al.,[17] being up to 0.3 eV higher for the indirect band gap and 0.3 eV lower for the direct transition. The change in band gap is attributed to the changes in oxidation state as a result of the synthesis method, which presumably also affects the mineral phase of the manganese oxide.

Table 7 - 3. Band gap results of the different manganese minerals in ferritin.

	Sample A	**Sample C**	**Sample B**	**Meldrum**	**Sample D1**	**Sample D2**	**Sample D3**
Stoichiometric Ratio or pH level	3:2	2:1	4:1	n/a	pH 5.4	pH 7.4	pH 9.4
Indirect Band Gap (eV)	1.90 ± 0.02	1.98 ± 0.02	1.85 ± 0.04	1.65 ± 0.02	1.94 ± 0.02	1.94 ± 0.02	1.94 ± 0.04
Direct Transition (eV)	2.56 ± 0.02	2.70 ± 0.01	2.70 ± 0.03	2.85 ± 0.02	2.66 ± 0.02	2.66 ± 0.02	2.59 ± 0.02
Size (Mn/ferritin)	1350 ± 75	1000 ± 150	4200 ± 100	650 ± 50	1850 ± 75	450 ± 30	160 ± 5
Suggested Mineral from Pourbaix diagram	Mn_2O_3	Mn_3O_4	Mn_3O_4	Mn(O)OH	Mn_3O_4	Mn_3O_4	MnO_2

Conclusion

A new synthesis method for preparing manganese ferritin minerals using comproportionation reactions combining permanganate and Mn(II) created new manganese oxide cores inside ferritin. The resulting cores possessed mixed oxidation states of Mn(II)/Mn(III) for the mineral Mn_3O_4, Mn(III) for the mineral Mn_2O_3 and Mn(IV) for the mineral MnO_2. Additionally, we report that our attempts to entrap permanganate inside ferritin caused oxidation of apoferritin but produced mixed oxidation states of Mn(II)/Mn(III) in the form of Mn_3O_4 at pH 5.4 and pH 7.4 but produced a Mn(IV) mineral MnO_2 at pH 9.4.

The new manganese ferritin mineral phases are different than those prepared by the synthesis method of Meldrum et al.[6] based on differences in UV/Vis spectra and the various oxidation states of manganese. The new mineral phases and oxidation states altered the band gaps from the Meldrum synthesis.[17] The mineral phases and oxidation states of these new manganese minerals in ferritin expands the possible applications of manganese ferritin in photovoltaics and nanobattery technologies.

Supplemental Figures

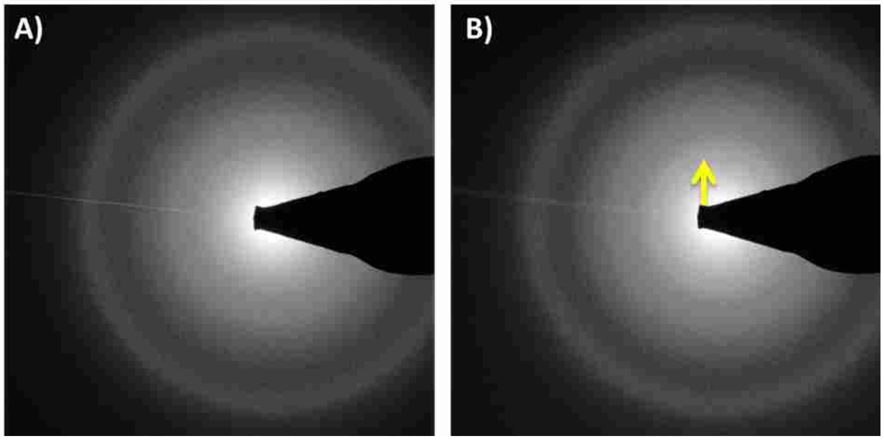

Supplemental Figure 7 - 1. Representative TEM diffraction patterns of a) amorphous carbon and b) Mn-Ferritin. Only one additional diffuse diffraction ring is visible in B and is highlighted by an arrow.

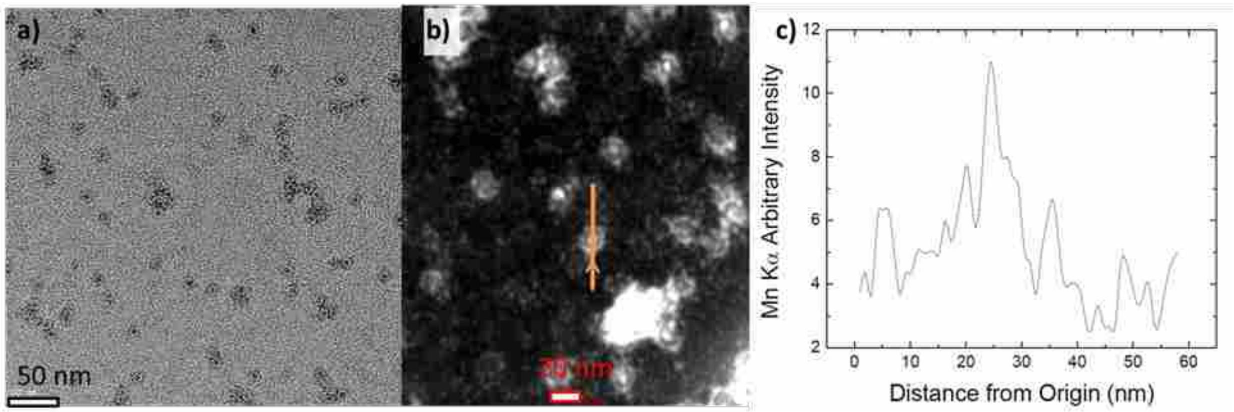

Supplemental Figure 7 - 2. TEM analysis of sample D1, manganese-loaded ferritin prepared by the permanganate loading into apoferritin reaction at pH 5.4. (a) Bright field TEM image. (b) STEM image, with line scan for the EDX measurement indicated in orange. (c) The intensity of the Mn-Kα signal as a function of distance from the origin indicating the presence of Mn in the interior of the ferritin molecule.

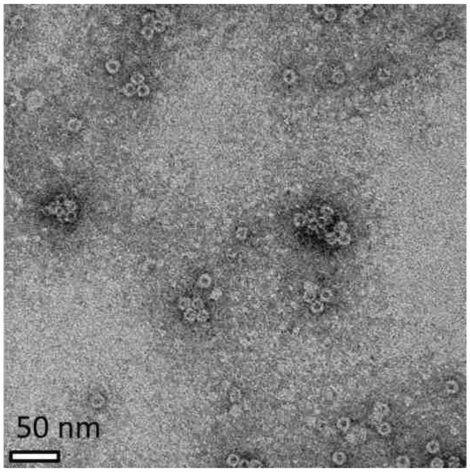

Supplemental Figure 7 - 3. Bright field TEM image of sample D2, manganese-loaded ferritin prepared by the permanganate loading into apoferritin reaction at pH 7.4. The manganese cores for this sample (450 Mn/ferritin) were insufficient to perform EDX analysis.

Notes

Reducing agents were also tested to see if permanganate by itself could load into ferritin without consuming the protein in the process. The reducing agents were sodium citrate and sodium dithionite in stoichiometric amounts for a targeted Mn(IV) core. These were tested as being either in solution prior to the permanganate addition, or as co-injections. However, all of these conditions failed to produce a manganese oxide core inside of ferritin at any pH previously tested, suggesting that permanganate binding to the protein is important.

References

---

[1] Stoimenov, P. K., Klinger, R. L., Marchin, G. L. & Klabunde, K. J. Metal Oxide Nanoparticles as Bactericidal Agents. *Langmuir* **18,** 6679–6686 (2002).

[2] Franke, M. E., Koplin, T. J. & Simon, U. Metal and Metal Oxide Nanoparticles in Chemiresistors: Does the Nanoscale Matter? *Small* **2,** 36–50 (2006).

[3] Jeng, H. A. & Swanson, J. Toxicity of Metal Oxide Nanoparticles in Mammalian Cells. *Journal of Environmental Science and Health, Part A* **41,** 2699–2711 (2006).

[4] Klem, M. T., Mosolf, J., Young, M. & Douglas, T. Photochemical Mineralization of Europium, Titanium, and Iron Oxyhydroxide Nanoparticles in the Ferritin Protein Cage. *Inorg. Chem.* **47,** 2237–2239 (2008).

[5] Douglas, T. & Stark, V. T. Nanophase Cobalt Oxyhydroxide Mineral Synthesized within the Protein Cage of Ferritin. *Inorg. Chem.* **39,** 1828–1830 (2000).

[6] Meldrum, F. C., Wade, V. J., Nimmo, D. L., Heywood, B. R. & Mann, S. Synthesis of inorganic nanophase materials in supramolecular protein cages. *Nature* **349,** 684–687 (1991).

[7] Smith, T. J., Erickson, S. D., Orozco, C. M., Fluckiger, A., Moses, L.M., Colton, J.S., Watt, R.K., Tuning the band gap of ferritin nanoparticles by co-depositing iron with halides or oxo-anions. *J. Mater. Chem. A* **2,** 20782–20788 (2014).

[8] Polanams, J., Ray, A. D. & Watt, R. K. Nanophase Iron Phosphate, Iron Arsenate, Iron Vanadate, and Iron Molybdate Minerals Synthesized within the Protein Cage of Ferritin. *Inorg. Chem.* **44,** 3203–3209 (2005).

[9] Watt, R. K., Petrucci, O. D. & Smith, T. Ferritin as a model for developing 3rd generation nano architecture organic/inorganic hybrid photo catalysts for energy conversion. *Catal. Sci. Technol.* **3,** 3103–3110 (2013).

[10] Hilton, R. J., Zhang, B., Martineau, L. N., Watt, G. D. & Watt, R. K. Anion deposition into ferritin. *Journal of Inorganic Biochemistry* **108,** 8–14 (2012).

[11] Uto, K., Yamamoto, K., Kishimoto, N., Muraoka, M., Aoyagi, T., Yamashita, I., Electrostatic adsorption of ferritin, proteins and nanoparticle conjugate onto the surface of polyelectrolyte multilayers. *J. Mater. Chem.* **18,** 3876–3884 (2008).

---

[12] Ko, Y., Kim, Y., Baek, H. & Cho, J. Electrically Bistable Properties of Layer-by-Layer Assembled Multilayers Based on Protein Nanoparticles. *ACS Nano* **5,** 9918–9926 (2011).

[13] Chu, Sang-Hyon, Sang H. Choi, Gerald D. Watt, Jae-Woo Kim, Yeonjoon Park, Robert C. Davis, John N. Harb, Glen C. King, and Peter T. Lillehei. Fabrication of cell structures for bionanobattery. *Smart Struct. Mat.* **5389**, 443–451 (2004).

[14] Watt, G. D., Kim, J. W., Zhang, B., Miller, T., Harb, J. N., Davis, R. C., & Choi, S. H. A Protein-Based Ferritin Bio-Nanobattery. *Journal of Nanotechnology* **2012,** 9 (2012).

[15] King, G. C., Choi, S. H., Chu, S. H., Kim, J. W., Watt, G. D., Lillehei, P. T., Elliott, J. R.. *3rd International Energy Conversion Engineering Conference*. **2005.**

[16] Colton, JS, SD Erickson, TJ Smith, and RK Watt. “Sensitive Detection of Surface- and Size-Dependent Direct and Indirect Band Gap Transitions in Ferritin.” *Nanotechnology* 25, no. 13 (2014)

[17] Erickson, Stephen D, Trevor J Smith, Lance M. Moses, Richard K Watt, and John S. Colton. “Non-Native Co-, Mn-, and Ti-Oxyhydroxide Nanocrystals in Ferritin for High Efficiency Solar Energy Conversion.” *Nanotechnology* 26, no. 1 (2015).

[18] Kim, Ivan, Hazel-Ann Hosein, Daniel R. Strongin, and Trevor Douglas. “Photochemical Reactivity of Ferritin for Cr(VI) Reduction.” *Chemistry of Materials* 14, no. 11 (November 1, 2002).

[19] Keyes, J., Hilton, R., Farrer, J. & Watt, R. Ferritin as a photocatalyst and scaffold for gold nanoparticle synthesis. *J Nanopart Res* **13,** 2563–2575 (2011).

[20] Ensign, D., Young, M. & Douglas, T. Photocatalytic Synthesis of Copper Colloids from Cu(II) by the Ferrihydrite Core of Ferritin. *Inorg. Chem.* **43,** 3441–3446 (2004).

[21] Nikandrov, V. V., Grätzel, C. K., Moser, J.-E. & Grätzel, M. Light induced redox reactions involving mammalian ferritin as photocatalyst. *Journal of Photochemistry and Photobiology B: Biology* **41,** 83–89 (1997).

[22] Meldrum, F. C., Wade, V. J., Nimmo, D. L., Heywood, B. R. & Mann, S. Synthesis of inorganic nanophase materials in supramolecular protein cages. *Nature* **349,** 684–687 (1991).

[23] Rakshit, T. & Mukhopadhyay, R. Tuning Band Gap of Holoferritin by Metal Core Reconstitution with Cu, Co, and Mn. *Langmuir* **27,** 9681–9686 (2011).

[24] Johnson, J. L., Cannon, M., Watt, R. K., Frankel, R. B. & Watt, G. D. Forming the Phosphate Layer in Reconstituted Horse Spleen Ferritin and the Role of Phosphate in Promoting Core Surface Redox Reactions†. *Biochemistry* **38,** 6706–6713 (1999).

[25] Huang, H., Watt, R. K., Frankel, R. B. & Watt, G. D. Role of phosphate in iron(2+) binding to horse spleen holoferritin. *Biochemistry* **32,** 1681–1687 (1993).

---

[26] Trefry, A. & Harrison, P. M. Incorporation and release of inorganic phosphate in horse spleen ferritin. *Biochem. J.* **171,** 313–320 (1978).

[27] Zhang, B., Watt, R. K., Gálvez, N., Domínguez-Vera, J. M. & Watt, G. D. Rate of iron transfer through the horse spleen ferritin shell determined by the rate of formation of Prussian Blue and Fe-desferrioxamine within the ferritin cavity. *Biophysical Chemistry* **120,** 96–105 (2006).

[28] Theil, E. C. Ferritin: At the Crossroads of Iron and Oxygen Metabolism. *The Journal of Nutrition* **133,** 1549S–1553S (2003).

[29] Price, D. J. & Joshi, J. G. Ferritin: Protection of enzymatic activity against the inhibition by divalent metal ions in vitro. *Toxicology* **31,** 151–163 (1984).

[30] Price, D. & Joshi, J. G. Ferritin: a zinc detoxicant and a zinc ion donor. *Proceedings of the National Academy of Sciences* **79,** 3116–3119 (1982).

[31] Jacobs, D., Watt, G. D., Frankel, R. B. & Papaefthymiou, G. C. Iron(+2) binding to apo and holo mammalian ferritin. *Biochemistry* **28,** 9216–9221 (1989).

[32] Zhang, B., Watt, R. K., Gálvez, N., Domínguez-Vera, J. M. & Watt, G. D. Rate of iron transfer through the horse spleen ferritin shell determined by the rate of formation of Prussian Blue and Fe-desferrioxamine within the ferritin cavity. *Biophysical Chemistry* **120,** 96–105 (2006).

[33] Bradford, M. M. A rapid and sensitive method for the quantitation of microgram quantities of protein utilizing the principle of protein-dye binding. *Analytical Biochemistry* **72,** 248–254 (1976).

[34] Watt, G. D., Frankel, R. B. & Papaefthymiou, G. C. Reduction of mammalian ferritin. *Proceedings of the National Academy of Sciences* **82,** 3640–3643 (1985).

[35] B. Floyd Brown *et al. Corrosion and Metal Artifacts - A Dialogue Between Conservators and Archaeologists and Corrosion Scientists*. **1977,** Pg 9.

Chapter 8 – NASA - Bio-nano Propellants

This chapter contains the results of my research in conjunction with NASA to use Ferritin as a Bio-Nano-Propellant. The Figures, Photos, and Data were provided by our collaborators at NASA. I was responsible for synthesizing, characterizing, and drying ferritin for use as an oxidant in aluminum based powdered fuels.

Abstract

Ferritin was synthesized to contain almost 4000 peroxides by lyophilizing iron-free apoferritin with 30% peroxide. This produced a peroxide oxidant that increased the burn rate of an aluminum nanoparticle propellant by over four-fold.

Introduction

Aerospace engineering is a complex branch of science, creating fuels, motors, and vehicles that place objects in the atmosphere and into outer space. Rocket motors are a crucial piece of equipment that propels an object through earth's atmosphere and even sending objects into space. These motors house a volatile mixture of fuels that must burn at specific temperatures and pressure. However, the less tolerant a fuel is, the more ridged and expensive a rocket motor design becomes. These factors cause rocket motors to have specific applications, requiring a unique motor for a specific purpose. A more versatile and flexible fuel is preferred when constructing a multi-purpose rocket motor, both in terms of cost and efficiency.

A widely used class of rocket motors uses solid fuels. These fuels use dry mixtures of fuel and oxidizer to create a solid mass that is inserted into a rocket motor housing. These fuels are more energy dense than current liquid fuel technologies, but are more difficult to manufacture. A simplified and recently developed rocket motor uses aluminum nanoparticles and solid water to create propulsion.

An aluminum ice propellant (ALICE) consists of aluminum nanoparticles and water. After mixing, the material is frozen to keep it stable. This fuel uses the high heat of formation of aluminum oxide (−1669.8 kJ/mol) to power the rocket, and uses a three electron redox reaction with oxygen from Al(0) to Al(III). This fuel uses earth abundant materials, creates a benign product, and is relatively safe to handle compared to other rocket fuels.[1,2,3] Dr. Son who created the ALICE fuel noted that "the ALICE can be improved by using better oxidizers.[4]" Peroxide (-120.42 kJ/mol) is a better oxidant than water (-237.14 kJ/mole). Peroxide would increase the energy output of ALICE rockets by at least 10%, if not for its instability and degradation over time. By using the protein ferritin as a nanoscale capsule, the peroxide can be sequestered and protected from the aluminum, and may provide stabilization for peroxide.

The apoferritin cavity can be filled with oxygen containing molecules, whether it be peroxide or other molecules such as oxo-anions. The oxygen is released during combustion, to oxidize the protein as fuel to continue the reaction.

Materials and Methods

Ferritin was dialyzed against mercaptoacetic acid using established methods from M. Joo et al.[5] and J. Polanams et al.[6] The resulting apoferritin was then dialyzed against sodium dithionite and bipyridine to remove any remaining iron. The dialysis was finished by dialyzing against Mili-Q water. The resulting 'Apo-Apoferritin' contained less than 1 iron per 10 ferritins. The apo-apoferritin was then placed into a 30% peroxide solution and lyophilized to dryness. The peroxide ferritin powder was then used as a powder additive for further experimentation.

Peroxide content within the ferritin after lyophilization was measured by rehydrating a small fraction of peroxide ferritin and using peroxide concentration test strips to find the concentration of peroxide in the resulting solution.

Aluminum-peroxide ferritin testing

Various fuel-to-oxidizer mass ratios were tested using peroxide ferritin as the oxidizer and 73 nm aluminum nano-particles (AlNP) as the fuel. The AlNP were purchased from

Novacentrix, with an active area of 72% due to the formation of an Al_2O_3 layer on the exterior of the nanoparticle. Samples were mixed in different rations of AlNP/Peroxide-Ferritin to find the optimum fuel to oxidizer ratio, including 4:1, 1:1, 1:3, and 1:9 as well as neat AlNP and neat peroxide-ferritin. Samples were thoroughly mixed, and added to an 8 cm porcelain trough. An electric igniter was used to initiate the reaction and a video camera was used to record the burn rates of the various mixtures. The apparatus used is shown in Figure 8-1.

Figure 8 - 1. Test set-up for mass composition ratio optimization burn tests. Shown from the top to bottom are the platinum filament for ignition, a sample of nano propellant, the ceramic sample holder, and the molybdenum base plate. A razor blade was included to illustrate the scale used for this experiment.

Once the optimum ratio was determined, a stainless steel chamber was fabricated to test the pressure and atmospheric gas composition on the samples. The chamber (see Figure 8-2) was cylindrical in shape, had a 3.75” opening on one side, was 3.375” long, and had an internal volume of 37.28 in^3. An acrylic window was machined and placed over the front, and sealed with a Viton O-ring. The ceramic sample holder was placed inside the chamber to hold the nanopropellant samples.

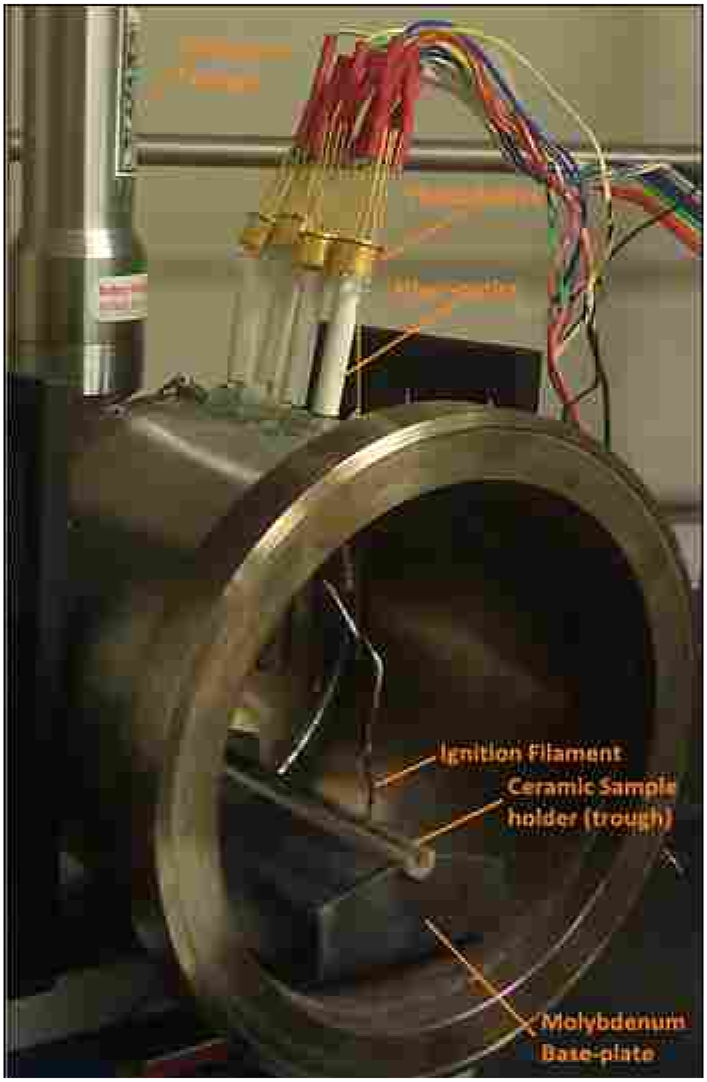

Figure 8 - 2. The Pressurized burn chamber with optical fiber/photodiode pairs for burn rate measurements and pressure gauge for gas generation measurements.

Four photodiodes (25° acceptance angle) placed 10 mm apart were used to measure the emission wavelengths as well as the burn velocity along the trough. The rear portion of the metal cylinder was used to adjust the atmospheric content as well as the pressure of the system.

Results and Discussion

Peroxide Content in Ferritin

Ferritin was found to contain 1350 peroxides per ferritin. We were unable to determine the location of the peroxide with respect to the ferritin protein. The peroxide is packed internally as either peroxide molecules associated with the protein matrix, or as a peroxo-amino acid.

Mass Composition Ratio Optimization

Burn rates were measured using the above mentioned apparatus as shown in Figures 8-1 and 7-2 to find the most optimum fuel to oxidizer ratio. The AlNP control gave a burn rate of 4-6 mm/s in the forward direction at standard temperature and pressure. It should be noted that in the AlNP only control sporadic burning would occur after the initial leading edge passed the detector, indicating that not all of the fuel was consumed on the initial pass of the propagating flame.

Next, varying ratios of AlNP:Peroxide-Ferritin were tested. The approximate 4:1 ratio (78% AlNP and 22% peroxide ferritin) at STP measured between 5-9 mm/s, a near two-fold increase over the AlNP control. It should also be noted that the AlNP burned much more energetically, and in only the forward direction. No sporadic burning was observed.

The 1:1 AlNP to peroxide ferritin sample gave the greatest burn rate increase, with a burn velocity of 15-16 mm/s (Figure 8-3). This sample burned over three times faster than the AlNP control, and created a significantly more energetic flame as well as burning in only the forward direction.

Figure 8 - 3. Comparison of flame size from three different propellant mixtures. A) 100% Aluminum nanoparticle powder (AlNP) (Video 7-1), B) 78% AlNP, 22% apoferritin/H_2O_2 (Video 7-2), C) 50% AlNP, 50% apoferritin/H_2O_2 (Video 8-3). In addition to having a larger flame, the burn rate also increased as more apoferritin/$H_2O_2$was added to the mixture, up to a 50% mixture. A video of this is available with the CD included in this dissertation.

Samples where the oxidizer was in greater proportion than the fuels were unsuccessful. The samples were unable to propagate the flame, and even higher ratios the sample would not ignite, including the peroxide ferritin only control.

Flame Emission spectra

The UV/VIS spectrophotometer used in the experiment recorded the emission spectra for each sample. With the addition of more peroxide into the ferritin, a greater blue shift was observed which suggests that the reaction became more energetic. There is a distinct peak at 590 nm present in each of the aluminum containing samples, which is associated with an intense emission peak from the aluminum combustion.[7] The increase in intensity indicates that the burn becomes faster and more energetic as a function of peroxide ferritin content.

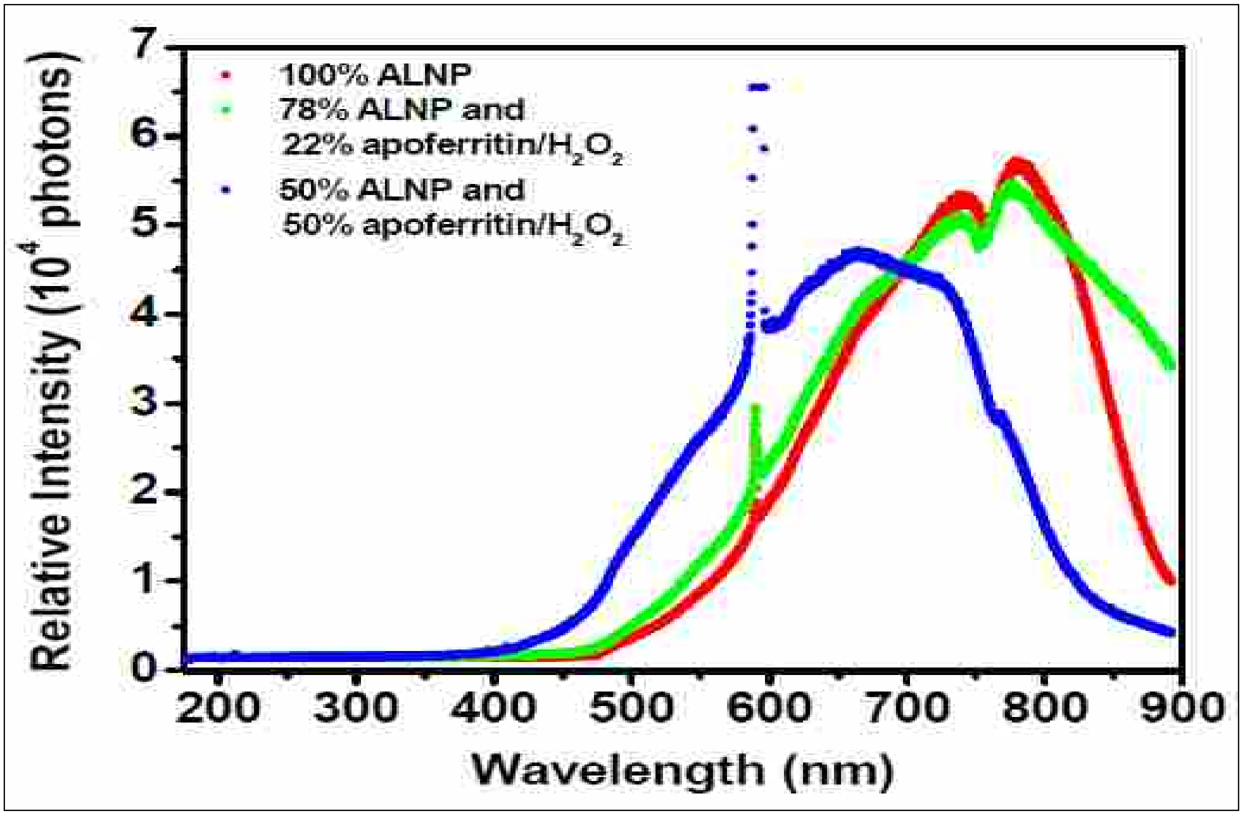

Figure 8 - 4. Flame emission spectroscopy of the three different mass ratio samples. As apoferritin/H2O2 is added, the emission spectrum shifts to higher energy (shorter wavelength). Each spectrum has a signature peak at ~590 nm, which increases as the weight percentage of apoferritin/H2O2 increases to 50%, indicating an increase in burn rate.

*P*ressure Results

The amount of gas generated during the combustion was measured as a variance in pressure and temperature. Only the 1:1 AlNP/Peroxide-Ferritin ratio was tested as it gave the best results in the previous tests. The sample was ignited inside the chamber at STP, and the pressure rose over the course of the 4 second burn time by 6 PSI. Accounting for the volume of the chamber (37.28 in^3) and using the ideal gas law (PV= NkT, where P is pressure, V is fixed volume, N is the number of gaseous particles, k is Boltzmann's constant, and T is absolute temperature), an estimated 5.94×10^{16} gaseous particles were generated.

Inside the pressure chamber the sample burned for a longer period of time when under atmospheric conditions. However, in the absence of oxygen the sample was unable to ignite, and is thought to be due to lack of gaseous oxygen needed to initiate the reaction.

Conclusion

The burn rate of the equal mass ratio fuel increased by two and a half fold in comparison to the pure AlNP control. While the AlNP only control was not able to produce a measurable flame height, the increased peroxide ferritin ratios gave a significant flame height up to 40 mm with the 1:1 ratio. Additionally, the 1:1 ratio burned in only the forward direction, meaning that the fuel to oxidizer ratio was near optimal for the combustion reaction. Less ideal ratios either gave bidirectional flame propagation when insufficient oxidant was present, or were unable to propagate at all when insufficient fuel was present.

The addition of peroxide ferritin enhances the combustive properties of the AlNP. Further testing is required to fully determine the optimum AlNP to peroxide ferritin ratio, as well as investigate the products of reaction as well as other alternatives to using ferritin as the encapsulating molecule.

References

---

[1] Kishore, K., Pai Verneker, V. R. & Prasad, G. Storage stability of solid rocket fuel. 1. Effect of temperature. *Fuel* **56,** 292–294 (1977).

[2] Kalyon, D. M., Yaras, P., Aral, B. & Yilmazer, U. Rheological behavior of a concentrated suspension: A solid rocket fuel simulant. *Journal of Rheology (1978-present)* **37,** 35–53 (1993).

---

[3] Wohlwend, K., L. Q. Maurice, T. Edwards, R. C. Striebich, M. Vangsness, and A. S. Hill. Thermal Stability of Energetic Hydrocarbon Fuels for Use in Combined Cycle Engines. *Journal of Propulsion and Power* **17,** 1258–1262 (2001).

[4] Accessed Janurary 30, 2015. Available at http://www.wpafb.af.mil/news/story.asp?id=123164277

[5] Joo, M.-S., Tourillon, G., Sayers, D. E. & Theil, E. C. Rapid reduction of iron in horse spleen ferritin by thioglycolic acid measured by dispersive X-ray absorption spectroscopy. *Biology of metals* **3,** 171–175 (1990).

[6] Polanams, J., Ray, A. D. & Watt, R. K. Nanophase Iron Phosphate, Iron Arsenate, Iron Vanadate, and Iron Molybdate Minerals Synthesized within the Protein Cage of Ferritin. *Inorg. Chem.* **44,** 3203–3209 (2005).

[7] A. Kramida, Yu. Ralchenko, J. Reader & and NIST ASD Team. (2014). Available: http://physics.nist.gov/asd [2015, May 11].

Chapter 9 – Department of Defense – Bio-nano Propellant

This project was performed under the Strategic Environmental Research and Development Program (SERDP) WP-2142 entitled "Novel Lead-Free Ballistic Modifiers for Improved, IM-Compliant Minimum-Signature Propellants." Researchers at the Naval Air Warfare Center-Weapons Division (NAWCWD) China Lake and Brigham Young University were tasked to demonstrate lead free alternatives as combustion catalysts for minimum signature rocket propellants. The data and major results from this project have not yet been released. I was responsible for synthesizing, characterizing, and drying the ferritin based perchlorate fuel for testing with energetic binders.

Abstract

The ability to tailor a propellant's burn rate utilizing formulation ingredients is an important factor in designing a solid rocket motor. Ferritin provides a unique scaffold for nanoparticle based catalysts. Co-deposition of perchlorate resulted in the greatest loading of anions per ferritin, reaching up to 300 perchlorates per 1500 irons.

Introduction

Solid rocket motors are limited by the performance of their solid rocket fuels. The ability to tailor a propellant's burn rate utilizing formulation ingredients is an important factor in designing a solid rocket motor. To address the performance challenges facing solid rocket motors lead based catalysts are used to control the burn rates without changing the overall composition of the solid rocket fuel.[1]

Lead catalysts allow for rocket motors to burn without leaving a smoke or vapor trail that would expose the locations of fighters and surface-to-air missile (SAM) sites to be discovered. However, the use of lead based catalysts produces adverse health and environmental affects that are dangerous. Additionally, other catalysts that are used in conjunction with lead do not maintain the same performance when lead is absent,[1] and some metals have been identified to work as lead substitutes; however they cause significant fuel degradation during storage. Therefore a lead free catalyst that is able to alter the burn rate of various rocket fuels is needed, while also maintaining the required high performance and smoke free properties is needed in rocket fuels. Ferritin has been shown to encapsulate lead-free metals and oxidants, which should also prevent fuel degradation during storage.

Ferritin provides a unique scaffold for nanoparticle catalysts. Ferritin measures 12 nm in diameter with an 8 nm hollow interior. It can sequester up to 4500 iron atoms as an Fe(O)OH mineral, and can also sequester a variety of anions. These anions are deposited through either an iron reduction as described by Hilton et al[2], or through an iron-anion co-deposition process as described in Chapter 3. The iron co-deposition process is the method that was used in these experiments as the reductive process requires an anaerobic environment that is impractical for solid rocket motor applications.

The work herein addresses the efficiency of perchlorate loading using various loading techniques. Many oxo-anions have been previously observed in ferritin *in vivo*, such as phosphate[3], and *in vito*, including molybdate, vanadate, tungstate, and perchlorate.[4,5] Phosphate, perchlorate, as well as other tetrahedral oxo-anions, are known to show high affinity for ferrihydrite's 110 plane. These anions are capable of adsorbing at a density of one oxo-anion per 0.66 nm sq.[6] However, these oxo-anions may also bind to the 100, 012, and 113 faces, and more rarely with the 104 and 001 faces. The ability of oxo-anions to bind to the different faces of the ferrihydrite mineral (whether as a multi-, bi-, or mono-dentate ligand) may play a role in how well perchlorate binds to the ferrihydrite mineral.

Perchlorate is a strong oxidant, and is the principle oxidant in ammonium perchlorate (AP) rocket fuels. AP rocket fuels consist of AP, a binder (usually hydroxyl-terminated polybutadiene (HTPB)), Aluminum, and burn rate metal catalysts (which usually contain lead). Varying the ratios between AP, binder, Al, and catalyst significantly alters the performance properties of the rocket. However, the use of lead is undesirable for health and environmental reasons. Therefore, a new and environmentally friendly additive is desired.

This study was undertaken to test if using ferritin with a perchlorate-iron-oxide core modifies the burn rate of existing solid rocket propellants.

Materials and Methods

Apoferritin was prepared using previously established methods from M. Joo et al[7] and J. Polanams et al.[3]

Iron perchlorate samples were prepared using three separate techniques, including Co-deposition, pH disassembly and reassembly, and simple anion diffusion. An additional set of samples using nitrate and carboxylic acid containing fuels were incorporated into ferritin using high concentrations of urea to loosen the hydrophobic interaction between ferritin subunits as described previously.[8,9] These samples will be called "ferritin-fuels" for convenience.

Co-deposited iron minerals were created using slight modifications to pH from previously established methods by Smith et al.[5] 5 mg of apoferritin was placed into a buffer free solution between pH 7.0 and 8.0 containing 500 mM sodium perchlorate. A 100 mM ferrous ammonium sulfate solution was added 10 µL at a time every 10 minutes, resulting in a rate of 100 irons per ferritin every 10 minutes. The pH was maintained between pH 7.0 and 8.0 by small additions of 300 mM NaOH. Core sizes were targeted at 2000 Fe/FTN. Samples were prepared in 10, 50, and 100 mg protein masses for further combustion testing.

Disassembly and reassembly of ferritin molecules was performed using established methods[10] by first carefully lowering the pH of a buffer apoferritin solution containing 500 mM sodium perchlorate between 3.5 and 4.0 using nitric for 15 minutes. The pH was then carefully raised to 7.0 using sodium hydroxide, which reassembles the ferritin molecule.

Simple diffusion of perchlorate was performed by adding native ferritin to a 500 mM solution of sodium perchlorate overnight.

After synthesis, samples were passed over a 15 cm x 1 cm Sephedex G-25 size exclusion gel filtration column using Mili-Q water as the eluent. Ferritin was observed to elute between fractions 4 and 6.

Protein analyses were conducted using a modified Lowry method.[11,12]

The iron analysis was performed using established methods.[13] 750 μL Mili-Q of water was added to 250 μL saturated bipyridine with at least 10 mg sodium hydrosulfide being added to the solution. The sample was then blanked inside a UV-VIS Spectrophotometer and a small aliquot of the iron-perchlorate sample was added to the solution while measuring the absorbance change at 522 nm is $\epsilon_{522} = 8650\ M^{-1}\ cm^{-1}$. This process was repeated in at least sextuplet for accurate iron determination.

Perchlorate concentrations were measured using previously established methods by either ion selective electrodes[14] or ICP-MS[15]. The irons per ferritin and perchlorates per ferritin ratios were calculated based on the molar fraction between the protein concentration and the iron concentration.

The co-deposition perchlorate-ferritin samples were first lyophilized as described in Chapter 7 and used in 1% dry mixtures with neat energetic binder (undisclosed). Pressed samples were formed into 2 mm pellets for further combustion testing. Powder samples were also used for various performance analyses, including thermal gravimetric analysis (undisclosed), and micro-ignition high speed video analysis (undisclosed).

The ferritin-fuel samples were prepared in high concentrations of urea, and passed over the G-25 column. Ferritin elutes faster with its sequestered urea as it passes over the size exclusion column, and the hydrophobic channels and subunits reassemble in the urea free soltuion, trapping the fuel inside ferritin. These samples were the lyophilized and tested using the aforementioned powder sample analysis.

Results and Discussion

Perchlorate composition

Co-deposition of perchlorate during iron loading resulted in the highest concentration of anion inside ferritin, between 10 and 20% or 150 to 300 perchlorates per 1500 irons. This particular loading method resulted in a stabilization of the perchlorate, which showed uniform and instantaneous combustion at 240 °C (figure not released). This is in stark contrast to neat perchlorate which begins to decompose at 215 °C, and combusts at 240 °C.

Disassembly and reassembly of ferritin using pH adjustments resulted in approximately 400 perchlorates per ferritin. However this method was less efficient as it caused up to 50% of the ferritin to precipitate.

Simple diffusion of perchlorate into ferritin showed less than 200 perchlorates per ferritin associated with or loaded into to protein. It is known that phosphate will associate on the surface of the ferrihydrite mineral at a density of about 10% or 1 phosphate per 10 irons. The 200 perchlorates per ferritin measured from this technique would suggest that the phosphate has been replaced by perchlorate.

Burn Testing – Perchlorate

Ferritin-perchlorate pellets were prepared for pressurized combustion testing as shown in Figure 9-1. It appears that the ferritin was preferentially deposited on the underside (brown side) of the binder material during pellet pressing. This may be an artifact of ferritins small size fitting well between the binder materials. This preferential deposition is observed in the pressurized burn tests.

Figure 9 - 1. Pressed perchlorate-ferritin pellets with binder material.

The burn tests needed to be pressurized in order to simulate the environment in which a rocket propellant is burned. This added pressure also helps to propagate the combustion which could not occur under atmospheric pressure. In the 500 PSI and 1000 PSI videos (see associated CD Video 9-1 and 9-2, respectively) the pellets are observed to

Figure 9 - 2. Image of perchlorate-ferritin pellet burning at 500 PSI. Ferritin is on the front facing portion of the pellet. (Image captured from Video 8-1)

burn from their interior, with some preference for the ferritin bound portions (See also Figure 9-2). The ferritin portion of the pellet does however burn with a liquid-like phase. Liquid phases in solid propellants are seen as the material is superheated and decomposes under high pressures (>10 MPa).[1] The liquid-like character is most likely a result of the ferritin protein decomposition.

Initial results suggest that the perchlorate-ferritin mixture altered the kinetics of the combustion reaction, showing a plateau like feature in the Pressure/Temperature burn rates. This plateau is proof that the perchlorate-ferritin is acting as a catalyst and would allow for more simple designs in rocket motor housings.

Burn Testing – Nitrate and Carboxylic Acid Containing Fuels

Ferritin-fuel samples were prepared using a high urea concentration to loosen the hydrophobic interaction between ferritin subunits. The elution profile for these samples as shown in Figure 9-3 were, by them self, inconclusive concerning whether or not the samples were contained within ferritin. Additional powder testing was later able to confirm the presence of these fuels within ferritin.

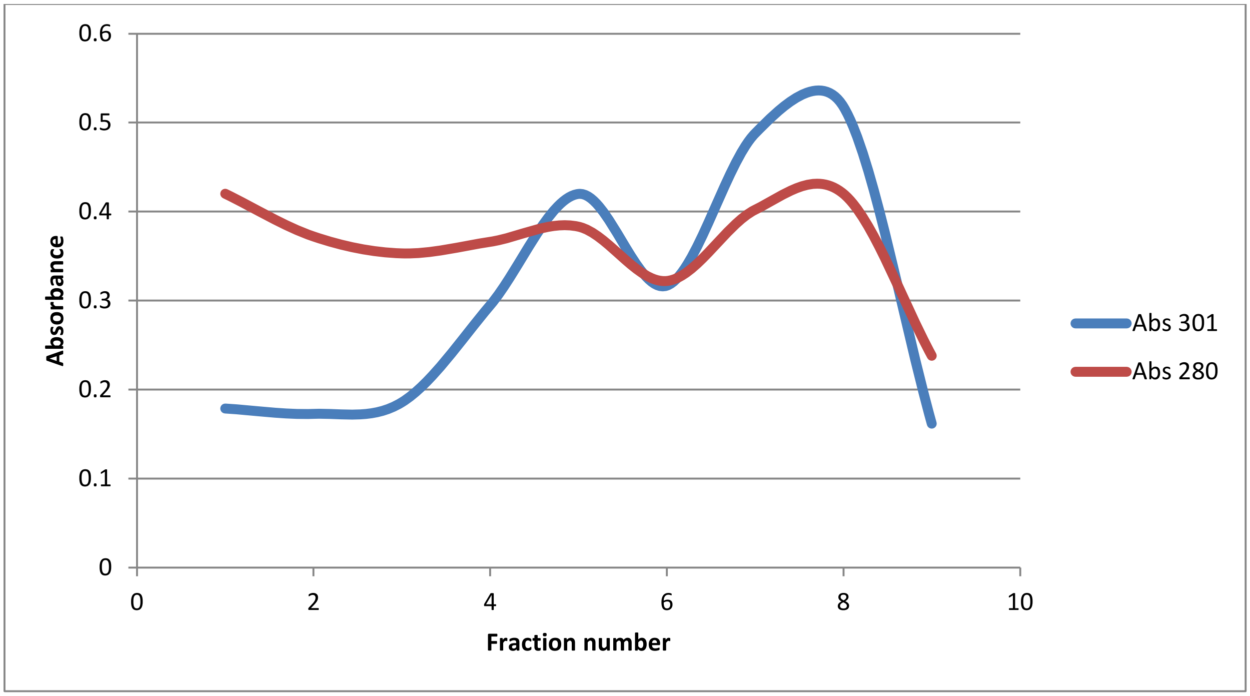

Figure 9 - 3. Representative elution profile of ferritin and fuel. Ferritin has an absorption peak at 280 nm, whereas the fuel has an absorption maximum at 301 nm. The proximity of the two absorption peaks makes it difficult to decouple whether or not the fuel was incorporated within the ferritin molecule.

Powder testing was performed using the ferritin-fuels, and gave evidence that the fuels were contained within ferritin. These ferritin-fuels were ignited using a hot platinum wire, where the ignition point is measured as a function of applied voltage across the platinum wire. The data collected from this experiment show the energy needed to initiate the combustion with the ferritin-fuel sample.

Conclusion

Perchlorate containing ferritins were able to alter the combustion kinetics of solid rocket propellant mixtures by decreasing the Pressure/Temperature dependent combustion kinetics. Using the co-deposition method, ferritin was able to sequester 150-300 perchlorates per ferritin, with an iron oxide core of 1500 irons per ferritin. This material when mixed as a 1% wt mixture with neat binder was able to desensitize the pressure/temperature dependence, which would allow for more simple designs in rocket motor housings.

References

---

[1] Yakovlev, S. I. Lead catalyst action mechanism in propellant burning. *Combust. Explos. Shock Waves* **27,** 28–32 (1991).

[2] Hilton, R. J., Zhang, B., Martineau, L. N., Watt, G. D. & Watt, R. K. Anion deposition into ferritin. *Journal of Inorganic Biochemistry* **108,** 8–14 (2012).

[3] Polanams, J., Ray, A. D. & Watt, R. K. Nanophase Iron Phosphate, Iron Arsenate, Iron Vanadate, and Iron Molybdate Minerals Synthesized within the Protein Cage of Ferritin. *Inorg. Chem.* **44,** 3203–3209 (2005).

[4] Zapien, D. C. & Johnson, M. A. Direct electron transfer of ferritin adsorbed at bare gold electrodes. *Journal of Electroanalytical Chemistry* **494,** 114–120 (2000).

[5] Smith, Trevor J., Stephen D. Erickson, Catalina Matias Orozco, Andrew Fluckiger, Lance M. Moses, John S. Colton, and Richard K. Watt. Tuning the band gap of ferritin nanoparticles by co-depositing iron with halides or oxo-anions. *J. Mater. Chem. A* **2,** 20782–20788 (2014).

[6] Cornell, R. M. & Schwertmann, U. *The Iron Oxides: Structure, Properties, Reactions, Occurences and Uses*. (Wiley-VCH Verlag GmbH & Co. KGaA, 2004).

[7] Joo, M.-S., Tourillon, G., Sayers, D. E. & Theil, E. C. Rapid reduction of iron in horse spleen ferritin by thioglycolic acid measured by dispersive X-ray absorption spectroscopy. *Biology of metals* **3,** 171–175 (1990).

[8] Theil, E. C., Liu, X. S. & Tosha, T. Gated pores in the ferritin protein nanocage. *Inorganica Chimica Acta* **361,** 868–874 (2008).

[9] Gálvez, N., Ruiz, B., Cuesta, R., Colacio, E. & Domínguez-Vera, J. M. Release of Iron from Ferritin by Aceto- and Benzohydroxamic Acids. *Inorg. Chem.* **44,** 2706–2709 (2005).

[10] Webb, B., Frame, J., Zhao, Z., Lee, M. L. & Watt, G. D. Molecular Entrapment of Small Molecules within the Interior of Horse Spleen Ferritin. *Archives of Biochemistry and Biophysics* **309,** 178–183 (1994).

[11] Lowry, O. H., Rosebrough, N. J., Farr, A. L. & Randall, R. J. Protein measurement with the Folin phenol reagent. *J biol Chem* **193,** 265–275 (1951).

---

[12] Peterson, G. L. A simplification of the protein assay method of Lowry et al. which is more generally applicable. *Analytical Biochemistry* **83,** 346–356 (1977).

[13] Moss, M. L. & Mellon, M. G. Colorimetric Determination of Iron with 2,2'-Bipyridyl and with 2,2',2'-Terpyridyl. *Ind. Eng. Chem. Anal. Ed.* **14,** 862–865 (1942).

[14] Hilton, R. J., Zhang, B., Martineau, L. N., Watt, G. D. & Watt, R. K. Anion deposition into ferritin. *Journal of Inorganic Biochemistry* **108,** 8–14 (2012).

[15] Erickson, S. D., Smith, T. J., Moses, L. M., Watt, R. K. & Colton, J. S. Non-native Co-, Mn-, and Ti-oxyhydroxide nanocrystals in ferritin for high efficiency solar energy conversion. *Nanotechnology* **26,** 015703 (2015).

Chapter 10 – Outlook

Permanganate and Redox Reactions with Other Transition Metals

Ferritin provides a unique model for nanoparticle and bio-materials research. It is capable of both mineralizing metal oxide nanoparticles and maintaining the integrity of those nanoparticles in photocatalytic reactions. However, most of the nanoparticles created in ferritin use one of three classes of reactions that were previously discussed in Chapter 7. These three reaction types are: oxidation through using the protein's ferroxidase center, photocatalytic oxidation-reduction, and metal reduction by sulfur oxidation.

In the work by Smith et al. (Chapter 7)[1], manganese and permanganate comproportionation in the presence of apoferritin created a new manganese oxide mineral in ferritin. The reduction of permanganate may replace oxygen as the oxidant and allow for other transition and non-transition metals to load into ferritin that would otherwise be too difficult to oxidize by using ferritin's normal ferroxidase center activity.

Permanganate can oxidize divalent metals to their 3^+ oxidation state in place of oxygen during metal loading into ferritin. It may also be possible to oxidize divalent metals to their 4^+ oxidation state. This reaction is known to work with iron[2] and manganese[1]. Other metals, including: cobalt, chromium, iron, cobalt, nickel, and copper are all viable candidates for permanganate redox reaction.

Cobalt would be the most likely element to work with this reaction. Ferritin requires assistance from peroxide ($H_2O_2 + 2H^+ + 2e^- \rightarrow 2H_2O = 1.78$ V) to load cobalt ($Co^{2+} \rightarrow Co^{3+} + e^- = -1.82$ V) under acidic conditions. The exact location for cobalt loading and oxidation into ferritin is not well demonstrated.[3] However, permanganate's strong oxidizing power in conjunction with cobalt oxidation should allow for cobalt loading into ferritin, and may even create a new mixed Co-Mn mineral. Whether or not a mixed metal core is observed in this reaction would add insight to the mechanism for permanganate deposition into ferritin.

Initial results with the permanganate and cobalt redox reaction suggest that a mixed Co-Mn mineral is formed inside ferritin as measured by ICP-MS. Whether these materials co-exist as a single mixed metal nanoparticle or as two separate mineral phases is yet to be determined. STEM in conjunction with a partial electron energy loss spectroscopy ((P)EELS) system may be able to resolve the location of the various elements. The (P)EELS system at BYU's TEM facility has an energy resolution of 0.4 eV and is able to detect the elemental data of a sample as well as image information from the same sample simultaneously. This produces a two-dimensional elemental or x-ray analysis of a sample which may allow for imaging of specific elements within the ferritin interior.

Chromate and Dichromate Redox Reactions with Transition Metals

Chromate and dichromate are known oxidants[4], and may assist in ferritin metal-oxide deposition.[5] The stronger oxidant is dichromate with a reduction potential of 1.33 V under acidic conditions and has a 6 electron reduction process, 3 electrons per chromium atom. Additional experiments similar to the permanganate redox technique may substitute oxygen and form mixed metal cores, comparable to permanganate. This reaction may create never before seen or analyzed mixed metal-oxide nanoparticles with chromium.

Non-native metals in ferritin for photochemical gold nanoparticle synthesis

Like the titanium gold nanoparticle work (Chapter 6), other non-native metal-oxides in ferritin are thought have photocatalytic properties. According to Nickandrov et. al.[6] and later Keyes et al.[7] UV light photocatalyzes a charge separation which creates an electron-hole pair; were the electron is able to leave ferritin and reduce various species in solution and the hole is filled by a sacrificial electron donor, such as citrate. This mechanism is thought to be independent of what the mineral inside ferritin is, as is demonstrated by the titanium oxo-hydroxide core inside ferritin.

Other nanoparticles, such as cobalt and manganese oxo-hydroxides inside ferritin may also reduce gold (III) ions or other species in solution. In the case of titanium, Ti(IV) is far more stable then Ti(III) and the oxidation from Ti(III) to Ti(IV) may or may not require the ferroxidase center (FC), and can be verified under anaerobic conditions. However, cobalt and manganese might require assistance from the FC to oxidize the metals from M^{2+} to M^{3+}. It should be noted that manganese is able to load into ferritin using the protein's FC, whereas cobalt requires a potent oxidant, such as peroxide, to assist in metal loading. The importance of the FC should be illustrated in comparing the kinetic rates of gold nanoparticle formation between these two minerals, where cobalt may have limited activity. Additional tested could be done using homopolymers of H- or L-chain ferritin, where only the H-chain ferritins would contain the FC, and the absence or abundance of H-chain ferritin would illustrate the FC importance in photocatalysis.

Conclusion

In the introduction I discussed how ferritin is used as a bio-inorganic material. Ferritin provides model for photovoltaic systems as it can sequester metals into metal-oxide nanoparticles, solubilize the nanoparticles, allow import and export of anions across the protein shell, and remain stable under a variety of condition.

In Chapters 1, 3, 4, and 5 I synthesized, characterized, and discussed how previously reported band gaps were either non-specific or incorrect, and was able to accurately determine the indirect band gaps and direct transitions of various metal-oxide cores in ferritin. I also demonstrated that the band gaps of the ferrihydrite mineral in ferritin can be tuned based on the anions present in solution and the anions used during iron deposition.

The anion co-deposition study lead me to investigate the effects of permanganate, a strong oxidizing agent, in manganese (II) and permanganate comproportionation reaction (Chapter 7). Here, I was able to create various manganese oxide cores in ferritin that had not been previously synthesized, including MnO_2, Mn_2O_3, and a Mn_3O_4. This work created a new class of reactions that could allow for unique and undiscovered mixed metal-oxide nanoparticles.

The information I learned from the band gap studies was used to demonstrate that a non-native metal, titanium oxo-hydroxide, in ferritin is able to function as a photocatalyst and reduce gold (III) ions into gold nanoparticles much faster than ferrihydrite nanoparticles.

The work described in this dissertation reconciled and added to the research concerning ferritin as a bio-inorganic material. And shows that ferritin is capable of acting as a photocatalyst, while also having applications in nanobattery technology.

References

---

[1] T. Smith, C. Olsen, J. Embley, S. Erickson, D. Buck, A. Neilson, J. Colton, R. Watt. *Inorg. Chem.* Submitted May 20, 2015.

---

[2] Smith, T. J., Erickson, S. D., Orozco, C. M., Fluckiger, A., Moses, L.M., Colton, J.S., Watt, R.K., Tuning the band gap of ferritin nanoparticles by co-depositing iron with halides or oxo-anions. *J. Mater. Chem. A* **2,** 20782–20788 (2014).

[3] Douglas, T. & Stark, V. T. Nanophase Cobalt Oxyhydroxide Mineral Synthesized within the Protein Cage of Ferritin. *Inorg. Chem.* **39,** 1828–1830 (2000).

[4] Available at http://en.wikipedia.org/wiki/Chromate_and_dichromate. Accessed May 16, 2015

[5] Cerkez, E. B., Bhandari, N., Reeder, R. J. & Strongin, D. R. Coupled Redox Transformation of Chromate and Arsenite on Ferrihydrite. *Environmental science & technology* **49,** 2858–2866 (2015).

[6] Nikandrov, V. V., Grätzel, C. K., Moser, J.-E. & Grätzel, M. Light induced redox reactions involving mammalian ferritin as photocatalyst. *Journal of Photochemistry and Photobiology B: Biology* **41,** 83–89 (1997).

[7] Keyes, J., Hilton, R., Farrer, J. & Watt, R. Ferritin as a photocatalyst and scaffold for gold nanoparticle synthesis. *J Nanopart Res* **13,** 2563–2575 (2011).